

**MULTICOLOR FLUORESCENCE MICROSCOPY FOR
TRACKING MAGNETIC MICRO-AGENTS**

Mert Kaya

MULTICOLOR FLUORESCENCE MICROSCOPY FOR
TRACKING MAGNETIC MICRO-AGENTS

DISSERTATION

to obtain
the degree of doctor at the University of Twente,
on the authority of the rector magnificus,
Prof. Dr. Ir. A. Veldkamp,
on account of the decision of the Doctorate Board,
to be publicly defended
on Thursday the 27th of October 2022 at 16.45 hours

by

Mert Kaya

born on the 28th of April 1989
in Istanbul, Turkey

THIS DISSERTATION HAS BEEN APPROVED BY:
PROF. SARTHAK MISRA

Cover design: Mert Kaya
Printed by: Ipskamp Printing, Enschede
ISBN: 978-90-365-5434-3
DOI: 10.3990/1.9789036554343

©2022 **Mert Kaya, The Netherlands**. All rights reserved. No parts of this thesis may be reproduced, stored in a retrieval system or transmitted in any form or by any means without permission of the author. Alle rechten voorbehouden. Niets uit deze uitgave mag worden vermenigvuldigd, in enige vorm of op enige wijze, zonder voorafgaande schriftelijke toestemming van de auteur.

GRADUATION COMMITTEE:

Chairman/secretary:

Prof. Dr. Ir. H.F.J.M. Koopman

University of Twente

Supervisor:

Prof. Dr. S. Misra

University of Twente,
University of Groningen
and University Medical Center Groningen

Co-supervisor:

Dr. I.S.M. Khalil

University of Twente

Committee Members:

Prof. Q. Zhou

Aalto University

Prof. Dr. I.S. Zuhorn

University of Groningen
and University Medical Center Groningen

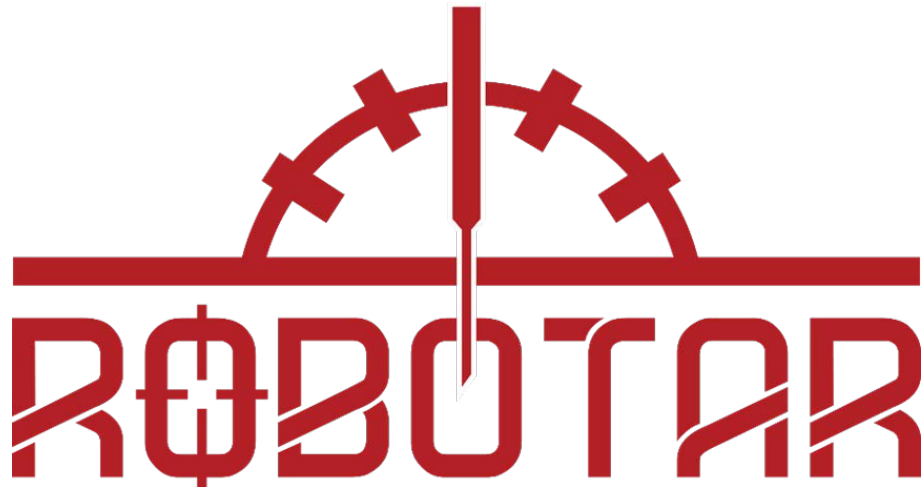
Prof. Dr. Ir. I.M. Vellekoop

University of Twente

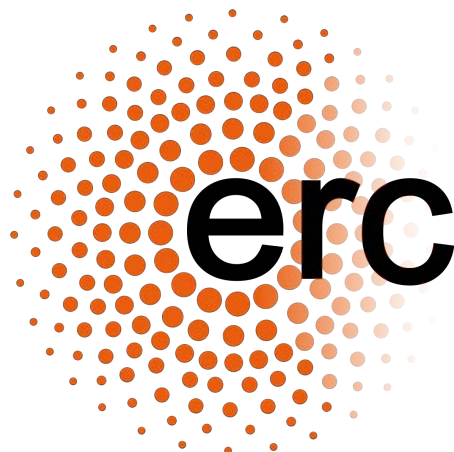
Dr. Ir. J. Rouwkema

University of Twente

THIS WORK IS PART OF THE RESEARCH PROJECT **ROBOTAR**.



The reported research has received funding from the European Research Council (ERC) under the European Union's Horizon 2020 Research and Innovation programme (Grant #638428 — project ROBOTAR: Robot-Assisted Flexible Needle Steering for Targeted Delivery of Magnetic Agents).



To my precious family and the man out of time...
Değerli Aileme ve zamanın ötesindeki bilim adamına...

Summary

The field of microrobotics opens the door to new therapeutic interventions by providing access to hard-to-reach regions of the human body. The envisioned interventions are based on the wireless movement of the micro-agents, part of the microrobotics systems designed to interact with the environments, using external stimuli (e.g., magnetic, sound, light, chemical, temperature). Although a wide variety of micro-agents have been designed, fabricated, and actuated, sensor integration remains a challenge due to size limitations. In order to understand and verify the functionality of the micro-agents, imaging modalities are utilized as external sensors and considered the only feedback source. Since experimental testbeds are fabricated using optically transparent materials, microscopy techniques have been extensively used in preliminary tests and lab-on-a-chip applications.

Single-band fluorescence and bright-field microscopy are commonly used to visualize the micro-agents with spatiotemporal resolution. However, single-band fluorescence microscopy renders visualization of only micro-agents and does not provide information about physical surroundings. Clear visualization of surroundings, as well as the micro-agents, is a requirement to reach the desired location. Bright-field microscopy enables visualization of micro-agents and surroundings, but acquired images do not reveal encoded information about identification and distinction. In this thesis, multicolor fluorescence microscopy is first applied for visualizing magnetically-actuated micro-agents and dynamic surroundings by relatively fast spectrum band change (multiplexing). The main difference of multicolor microscopy is that a sample containing micro-agents is fully resolved in different spectrum bands, and color-coded visualization is acquired. Since color is a visual cue for detection, acquired images enable an increased understanding of the micro-agent functionality and clear distinction of the surrounding media. This thesis aims to fill the gap in the literature on performing real-time multicolor microscopy for micro-agents and surroundings with three parts divided into six chapters.

Chapter 1 provides an overview of micro-agents and multicolor microscopy, as well as research questions tackled in this thesis. Subsequently, **Part I (Chapters 2-4)** describes the imaging, actuation, and tracking tools. A multicolor fluorescence microscope is developed

to excite the fluorophores in a round-robin manner and synchronously acquire images from three distinct spectrum bands. **Chapter 2** includes the microscope design, fluorophore selection, and spectrum analysis. A tumor environment is created by randomly placing cancer spheroids (formed with cervical HeLa cells) and polystyrene beads as drug carriers in a microfluidic channel. The environment is employed to validate that the microscope generates images with unambiguous color coding by spectral crosstalk analysis. Real-time multicolor microscopy is demonstrated by visualizing the attachment of the beads to a cancer spheroid utilizing electrostatic forces as a method for biohybrid drug carrier fabrication. The microscope is coupled with an orthogonal array of four iron-core coils to mobilize micro-agents using magnetic fields. The coils are individually powered using custom-made driver circuits.

Chapter 3 presents the coil driver architecture designed for magnetic manipulation of the micro-agents. A multilayer shielding enclosure is designed to prevent degradation of measurement and control signals by possible penetration of stray magnetic and electromagnetic waves. Finite element analysis shows that the shielding enclosure generates a low-resistance path for both magnetic and electromagnetic waves. Helmholtz, air-core, and iron-core coils are individually employed to experimentally validate that the driver is able to power different coil configurations. The effect of pulse width modulation (PWM) on the magnetic field and ohmic losses is observed at varying carrier frequencies and duty cycles. Experiments and finite element simulations reveal that magnetic field fluctuations minimize when PWM carrier frequencies are selected close to the self-resonant frequencies of the coils. In order to obtain automated quantitative data about actuated micro-agents through the generated magnetic fields, a visual tracker is implemented.

Chapter 4 introduces a visual tracking framework to localize different types of micro-agents without the need for specific detection and thresholding procedure. The working mechanism of the framework is based on computing the motion of a micro-agent between two consecutive frames using optimization techniques. In order to model the motion and compensate for the intensity fluctuations, the photometric affine function is selected. Pyramidal implementation of the framework is employed to render tracking of the micro-agents under the large motion displacements and prevent failures. The framework is combined with multi-rate state estimators for its usage in control applications by upsampling the actual image acquisition rate. The accuracy of the multi-rate state estimation is measured using high-speed bright-field imaging. The scientific tools introduced in **Chapters 2-4** are used in **Chapter 5** to acquire and analyze the multicolor images through experiments where the micro-agents are manipulated using magnetic fields.

Part II (Chapter 5) demonstrates the performance of real-time multicolor microscopy by visualizing micro-agents within 3D tumor-on-a-chip and vascular networks. The electrospinning technique is employed to fabricate magnetic and fluorescent micro-agents with relatively high photobleaching resistance. In order to visualize and measure sequential motion, cancer cell spheroids are actuated with the micro-agents in an open reservoir. A microfluidic chip is designed to create a tumor model, immobilize a single cancer spheroid in a fixed location, and provide a confined space for multicolor image acquisition. Single and cluster micro-agents are attached to the immobilized cancer spheroids as a proof-of-concept targeted drug delivery demonstration. Dynamic multicolor imaging reveals that the microfluidic chip maintains the cancer spheroids for long-term microscopy. *In vitro* perfusable vascular network and *ex ovo* chorioallantoic membrane are used to acquire spectrally resolved visualization of micro-agents in vascularized environments. Imaging experiments show that multicolor microscopy renders color-coded visualization

of polymeric micro-agents, organic bodies (cancer spheroids and vessels), and surrounding media in real-time.

Part III (Chapter 6) concludes this thesis by highlighting the main contributions and future implications. **Chapter 6** first presents the conclusions of research conducted in **Chapters 2-5** and couples them with potential applications in the field of microrobotics. The subsequent section provides an outlook for follow-up research studies. Guidelines are suggested for fabricating therapeutic micro-agents and monitoring their efficacy on live cells using multicolor microscopy. The microscope-in-a-catheter concept is proposed for real-time multicolor image acquisition of micro-agents inside the tissue. This concept holds the potential to accelerate the clinical translation of micro-agents by enabling visualization of drug release under *in vivo* conditions.

Contents

1	Introduction	17
1.1	The Field of Microrobotics	17
1.2	Multicolor Fluorescence Microscopy	25
1.3	Research Objectives	27
1.4	Thesis Outline	28
1.5	Research Framework and Scientific Outputs	29

I

Scientific Tools

2	Multicolor Fluorescence Microscope	35
2.1	Introduction	36
2.2	Materials and Methods	37
2.2.1	Spectrum Analysis	37
2.2.2	Multicolor Fluorescence Microscope Architecture	37
2.2.3	Demultiplexer Interface	39
2.2.4	Cell Culture and Spheroid Formation	39
2.2.5	Agarose Molds	41
2.2.6	Cell Labelling using CMTPIX and Fixation	42
2.2.7	Microfluidic Channel Fabrication	42
2.2.8	Image Acquisition	42
2.3	Results	42
2.3.1	Multicolor Fluorescence Image Acquisition	42
2.3.2	Crosstalk Analysis for the Multicolor Fluorescence Microscopy	44
2.3.3	Exposure Time Analysis	46
2.3.4	Uptake of Indocyanine Green by HeLa Cell Spheroids	48

2.3.5	Photobleaching Resistance	51
2.3.6	Photodamage Analysis	51
2.3.7	Real-time Multicolor Fluorescence Microscopy	53
2.4	Conclusions	54
3	Electromagnetic Coil Driver	57
3.1	Introduction	58
3.2	Coil Driver	58
3.2.1	Driver Architecture	58
3.2.2	Magnetic and Electromagnetic Shielding	60
3.3	Experiments	60
3.3.1	Finite Element Results	60
3.3.2	Experimental Setup	63
3.3.3	Experimental Results	63
4	Template-Based Visual Tracking	67
4.1	Introduction	68
4.2	Visual Tracking of Magnetic Micro-Agents	69
4.2.1	Motion Model	70
4.2.2	SSD-based Visual Tracking	71
4.2.3	NCC-based Visual Tracking	72
4.2.4	Pyramidal Implementation	72
4.2.5	Template Update Strategy	72
4.3	Multi-Rate State Estimation	72
4.3.1	System Description	73
4.3.2	A Multi-Rate Luenberger Observer	76
4.3.3	A Multi-Rate Kalman Filter	76
4.4	Collaborative Tracking using Observers	77
4.5	Experiments	78
4.5.1	Experimental Setup	78
4.5.2	Execution Times	78
4.5.3	Experimental Results	79
4.6	Conclusions	81

II System Integration and Real-Time Multicolor Microscopy

5	Real-Time Multicolor Microscopy	87
5.1	Introduction	88
5.2	Methods	90
5.2.1	Micro-Agent Fabrication using Electrospinning	90
5.2.2	Spectrum Analysis	90
5.2.3	HeLa Cell Spheroids Formation	93
5.2.4	Microfluidic Chip Fabrication	93
5.2.5	3D Co-Culture in a Microfluidic System for <i>In Vitro</i> Vascularization	93
5.2.6	Chicken Vasculature	94
5.2.7	Multicolor Fluorescence Microscopy and Magnetic Movement	94

5.2.8	Ethics Statement	96
5.3	Results	98
5.3.1	Single-Band Fluorescence Microscopy	98
5.3.2	Attachment of micro-agents to HeLa cell spheroids	98
5.3.3	Translation and Rotation of Cell Spheroids by Micro-Agents Attachment ...	100
5.3.4	Micro-Agents Attachment to Immobilized HeLa Cell Spheroids	103
5.3.5	Micro-Agents inside a Perfusable Vascular Network	105
5.3.6	Micro-Agents inside Chorioallantoic Membrane Vasculature	106
5.4	Conclusions	109

III

Concluding Remarks

6	Conclusions	113
6.1	Part I - Scientific Tools	113
6.2	Part II - System Integration	114
6.3	Outlook	115
6.3.1	Fabrication of Polymeric Micro-Agents containing Drugs	115
6.3.2	Visualization of Drug Release and Cellular Viability	116
6.3.3	Multicolor Microscope-in-a-Catheter	117
	Bibliography	119
	Articles	119
	Books	131
	Acknowledgments	133
	About the Author	135

1. Introduction

The focus of this thesis is real-time imaging system development for magnetic micro-agents. This chapter first introduces the relevant literature review and existing imaging challenges. In the following sections, the research questions and proposed solutions are detailed. The chapter concludes by giving the outline and publication outcomes of the research conducted in this doctoral study.

1.1 The Field of Microrobotics

Developing stimuli-responsive actuators by technologies for creating small-scale structures (not greater than 1 mm) has emerged a new field of study called microrobotics [1]. Over the last two decades, advances in microrobotics have introduced innovative techniques to reach areas inaccessible with conventional tools [2–4]. This feature finds use in healthcare [5], environmental cleaning [6], micro-assembly [7], and sensing fields [8]. Among the application domain of microrobotics, minimally invasive surgery and targeted drug delivery are two prominent examples directly related to human health [9]. Preclinical experiments have shown that microrobotics pave the way for reshaping surgical interventions and reducing the side effects of drugs. Although there are challenges to be resolved for clinical translation, microrobotics offer a remedy for the cure of many diseases. The future potential of microrobotics for treatments is detailed using cancer, one of the global health problems.

Various drugs have been developed and implicated in clinical use to treat cancer and prevent its recurrence. Despite the considerable efforts and technological breakthroughs, the success rate of the drugs is still low since only 0.7% of the given dosage level can be delivered to cancer cells [10, 11]. For this reason, drug treatments are not feasible for most patients. In this case, complicated surgery is necessary to extract the cancerous tissue. Conventional surgical interventions utilize techniques that make use of tools such as scalpels, tweezers, and micro-scissors. Such interventions are invasive and cause large wounds to the patients. Severe side effects like hemorrhage and metastasis might occur during a relatively long recovery period. The cancerous tissue can also be in a region

difficult to reach with the tools, so performing surgery may not be possible. Microrobotics overcome restrictions in cancer treatment by providing non-invasive access to tissues. Micro-agents, the end-effector of microrobotic systems, are able to be coated with nanoparticle drugs and manipulated toward the cancer tissue [12]. Upon therapeutic micro-agents reach the desired location, triggering the release renders (1) concentrating drug particle delivery to the cancer cells for the successful treatment and (2) minimizing the side-effects of the drugs, patient recovery time, and pain. Manipulability of micro-agents for concentrating drug particles in a specific tissue opens an avenue to shift medical practices (not limited only to cancer treatment) towards interventions using microrobotic systems (Fig. 1.1-(a)) [13–15]. One of the most conspicuous interventions are ophthalmic therapies [16], fertilization [17], blood clot breakdown [18], and biopsy [19] (Fig.1.1-(b)-(e)).

To date, systems have been developed for diverse microrobotics applications, including therapeutic interventions, to manipulate micro-agents in a controlled manner [22–24]. The structure of systems often consists of a macroscopic actuation setup, micro-agents having polymeric or biological entity bodies, and an imaging unit for localization. The actuation setups generate forces to manipulate micro-agents. The dynamic motion of micro-agents is achieved by propulsion and steering forces [25, 26]. The propulsion force is generated by (1) external power provided using the actuation setups [27], (2) conversion of chemical energy into kinetic energy [28], and (3) a micro-organism containing cilia or flagella [29]. Regardless of the propulsion force generation, micro-agents are steered using fields or gradients produced by external stimuli such as magnetic, ultrasound, light, and electrostatic [2]. Among these, the magnetic field is preferable due to the ease of control and fast response time. The key feature of the magnetic field is that it does not attenuate inside the human body and allows manipulation of micro-agents towards hard-to-access regions. Therefore, magnetic actuation techniques have progressed substantially in recent years. Sophisticated actuation setups, consisting of electromagnetic coils or permanent magnets that enclose the workspace, have been designed to manipulate agents inside the tissue or vessels by generating the required field intensity (Fig. 1.2) [30]. Additionally, much effort has been directed to fabricating therapeutic agents that respond to the magnetic field.

Photolithography-based manufacturing techniques have been extensively used to fabricate micro-agents [36–38]. The standard lithography techniques, in which the negative photoresist is exposed to the light using patterns, allow the fabrication of micro-agents with planar 2D and 2.5D geometries down to 10 nm resolution (Fig. 1.3-(a)) [39]. Direct laser writing (DLW), defined as lithography-based additive manufacturing technology, overcomes limitations in the standard techniques by enabling 3D printing of micro-agents with intricate geometries (Fig. 1.3-(b)) [40, 41]. In order to fabricate biocompatible and biodegradable micro-agents containing drug particles, DLW provides a printing resolution down to 100 nm [42]. For manipulation, magnetic particles are sputtered on the surface of the micro-agent in the post-fabrication stage or directly mixed with the printing resin [43, 44]. An alternative to lithography-based techniques is biotemplating, also known as biohybrid micro-agent fabrication. Biotemplating allows utilizing cells and organisms as micro-agents by attaching magnetic nanoparticles to their surfaces via electrostatic interactions (Fig. 1.3-(c)) [2, 3]. The superiority of biotemplating is that the fabricated micro-agents do not cause cytotoxic effects on the cells since they consist of biocompatible elements. As in the lithography studies, it has been experimentally validated that micro-agents fabricated using biotemplating can transport drugs to cells [45]. Although therapeutic micro-agents with high architectural complexity are able to be fabricated with plenty of methods like lithography and biotemplating, sensor integration is not feasible

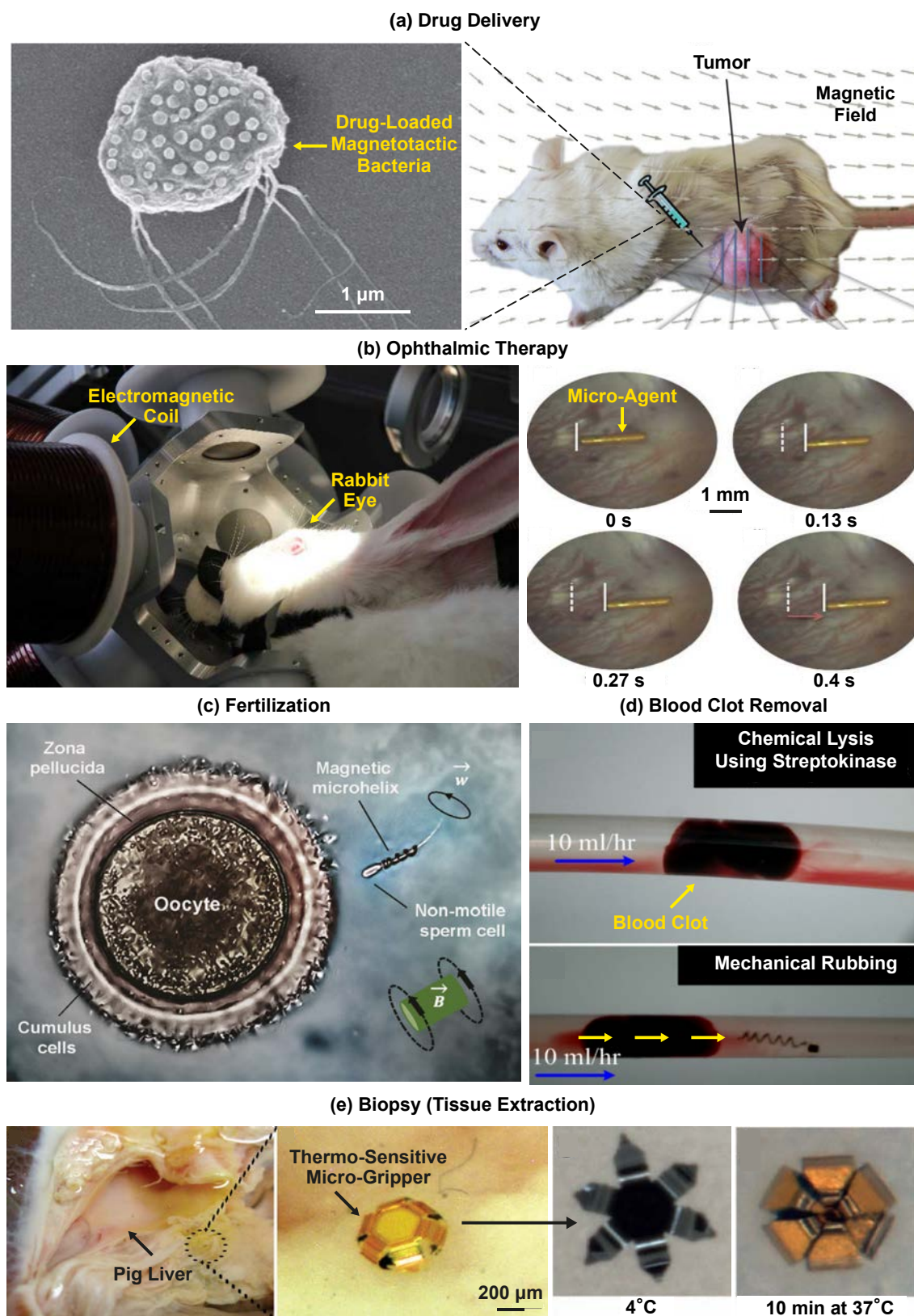


Figure 1.1: Example applications of microrobotics in healthcare. (a) Targeted drug delivery in a tumor-bearing mouse using biohybrid micro-agents [13]. (b) Minimally invasive ocular surgery using a micro-agent [20]. (c) Sperm delivery to an egg cell with a magnetic helix carrier [17]. (d) Blood clot breakdown using a helical micro-agent [18]. (e) Tissue extraction using magnetic and thermo-responsive micro-gripper [21].

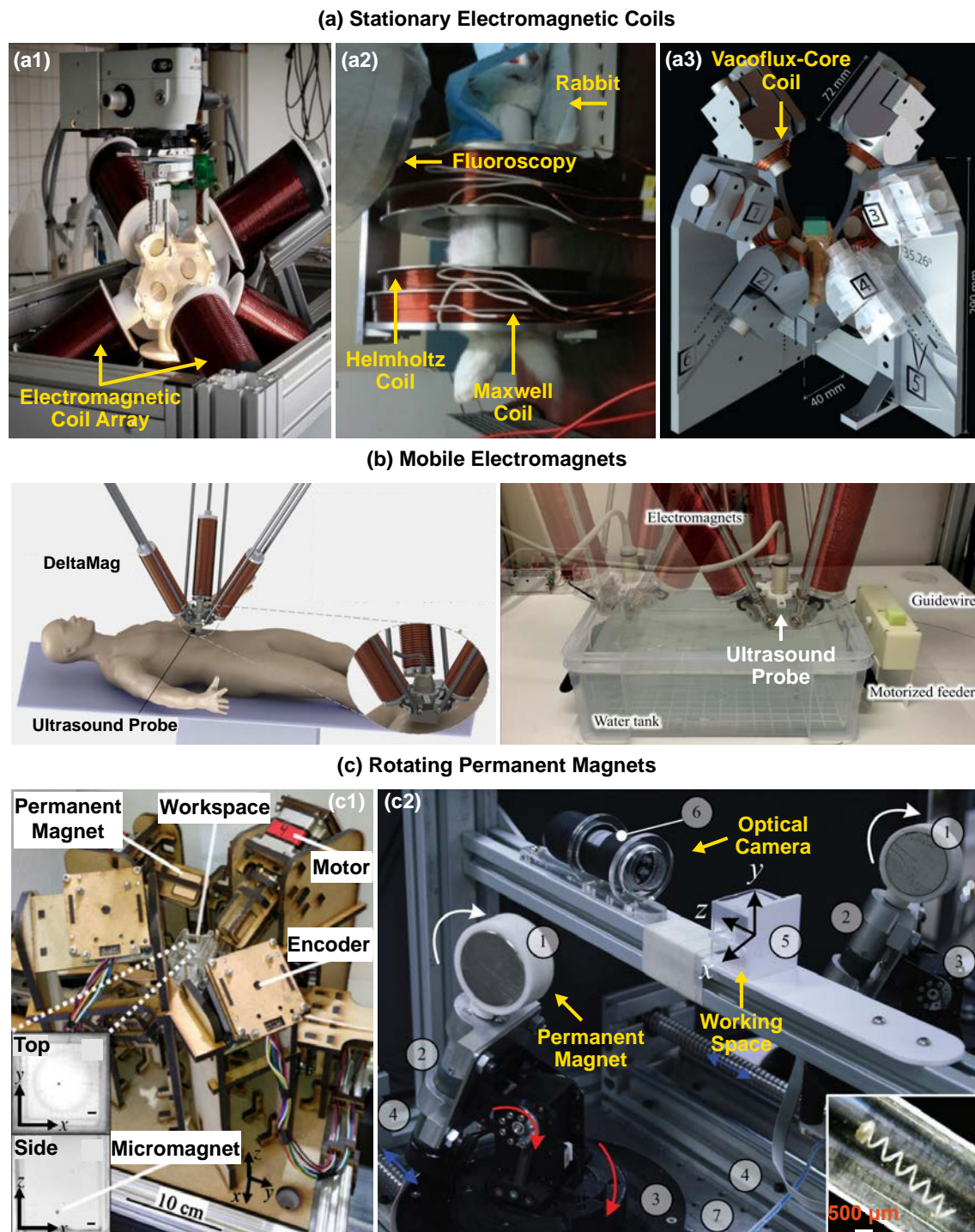


Figure 1.2: Various developed systems for the manipulation of micro-agents using magnetic fields. (a1)-(a3) The systems generate controlled field intensity and gradients with stationary coil configurations [20, 31, 32], respectively. (b) An coil array placed in a delta arm for clinical scenarios [33]. (c1) and (c2) Articulated mechanisms that manipulate the micro-agents by rotating the permanent magnets [34, 35], respectively.

due to size limitations [27, 46, 47]. Therefore, imaging modalities are used as external sensors to obtain three necessary components for successful manipulation: localization of micro-agents, path planning via visualizing surrounding tissue, and target identification.

Micro-agents and physical surroundings are able to be visualized under *in vivo* and *in vitro* conditions using magnetic resonance imaging (MRI), single-photon emission computed tomography (SPECT), fluoroscopy, ultrasound, photoacoustic, and optical imaging. Among the modalities, MRI has a unique feature that enables simultaneous manipulation and visualization of the micro-agents [53–55]. Gradient coils inside the MRI machine generate field intensity for both propulsion and steering of the micro-agents. Acquired MRI images also contain visualization of both micro-agents and anatomical structures with a relatively high contrast-to-noise ratio (Fig. 1.4-(a)). However, MRI is not a suitable modality for microrobotics applications that require real-time image acquisition since it suffers from relatively low temporal resolution. Similar to MRI, SPECT provides a relatively high temporal resolution and a low acquisition rate that hinders its use for the real-time manipulation of micro-agents (Fig. 1.4-(b)) [56]. Besides, the relatively narrow and enclosed working space of SPECT restricts the integration of the actuation setups. Compared to SPECT, fluoroscopy [23, 31, 57, 58] and ultrasound [59–62] ensure (1) real-time image acquisition and (2) a relatively larger working space that allows the integration of stationary and articulated actuation setups. The shortcoming of the ultrasound is that the acquired images are inherently noisy and contain relatively high-intensity artifacts, which hamper the visualization of micro-agents (Fig. 1.4-(c) and (d)). The photoacoustic technique, defined as light-induced ultrasound imaging, makes it possible to increase the acoustic intensity of micro-agents containing metals. The light absorption of the metals emits ultrasound waves, which render resolving micro-agents from artifacts and surrounding tissue by contrast enhancement (Fig. 1.4-(e)) [63–65].

Optical imaging techniques provide shallow imaging depth compared to the previously mentioned imaging methods. Optical coherence tomography (OCT), endoscopy, fluorescence imaging, and microscopy are the techniques used in the microrobotics field. Among these, OCT has the maximum imaging depth and allows visualization of the micro-agents in the tissue up to 1-2 mm (Fig. 1.5-(a)) [67]. Fiber-optic endoscopes are employed to deliver micro-agents in the gastrointestinal tract and visualize them on the surface area owing to their flexible structures (Fig. 1.5-(b)) [68]. *In vivo* fluorescent imaging is used to visualize micro-agents within the mice by collecting emitted light using a camera (Fig. 1.5-(c)). In order to localize the micro-agents within the whole body, mice are visualized using bright-field imaging and then overlaid on the acquired fluorescent images [14, 69, 70]. Optical microscopes are the essential tools for initial studies and organ-/lab-on-a-chip applications of microrobotics (Fig. 1.5-(d)) [27, 71]. Bright-field microscopy is the most widely used technique due to its ease of use, allowing label-free image acquisition, and relatively high-temporal resolution [61, 72–75]. However, acquired bright-field images do not provide encoded information for tracking and identification (Fig. 1.5-(e)). Besides, the height differences between micro-agents and surroundings cause blurring since bright-field microscopes do not acquire focussed images from multiple planes. Single-band fluorescence microscopy ensures visualization of micro-agents with a higher contrast-to-noise ratio compared to bright-field [19, 23, 60, 76]. The bottleneck of the acquired images is that they do not provide information about surroundings, which is the required component for manipulation. This thesis introduces multicolor microscopy to render an entire sample containing micro-agents visible by fluorescence imaging. The main contribution of this thesis is that direct identifications of micro-agents, targets, and surroundings are obtained

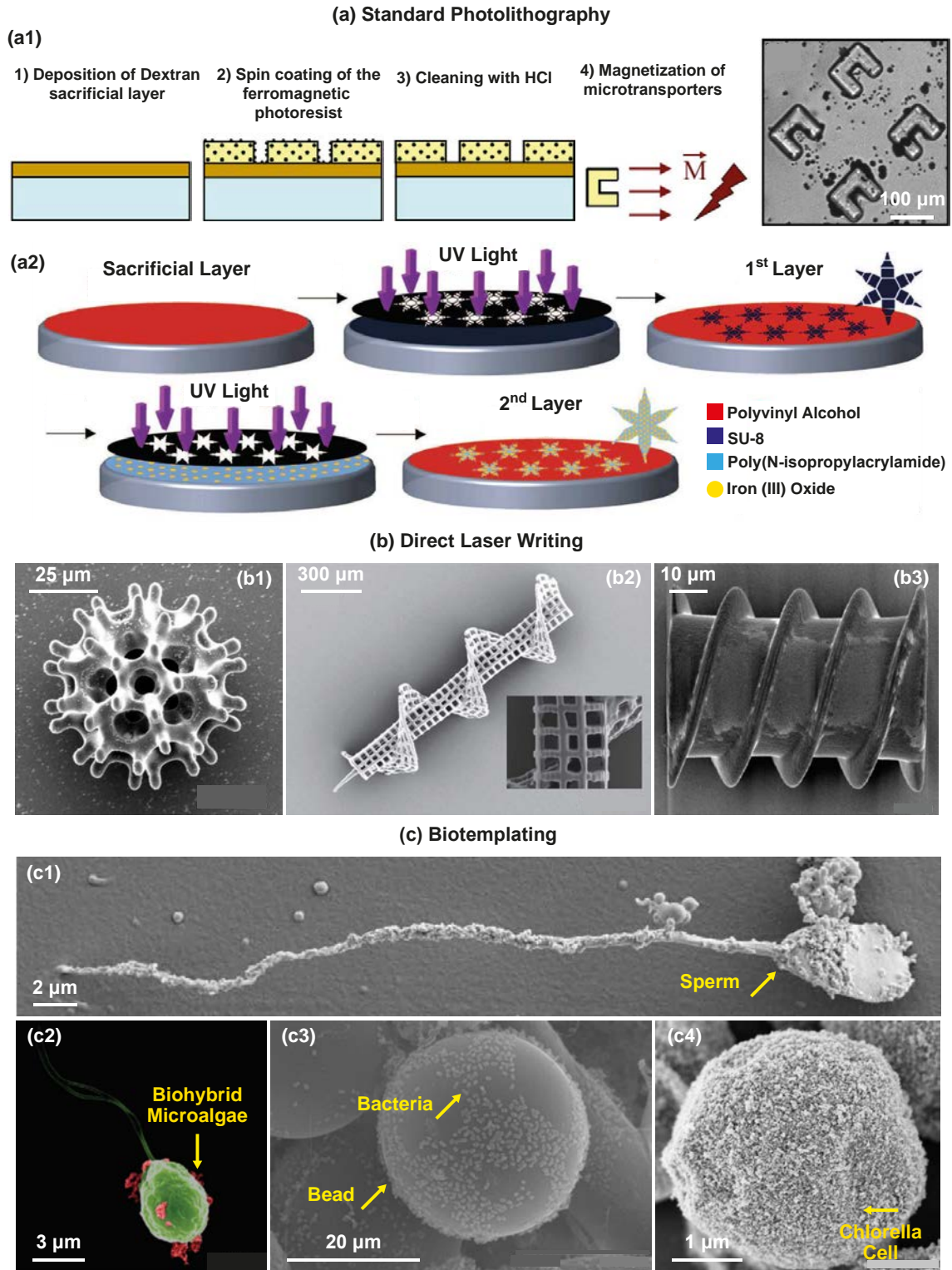


Figure 1.3: Three commonly used techniques for micro-agent fabrication. (a1) and (a2) Cell carrier [38] and thermo-responsive micro-gripper fabrication [48] using standard photolithography, respectively. (b1)-(b3) 3D printed micro-agents with intricate geometries [14, 49, 50], respectively. (c1)-(c4) Biohybrid micro-agents fabricated by adding magnetic nanoparticles to the surface of sperm [3], microalgae [45], bacteria [51], and chlorella cell [52], respectively.

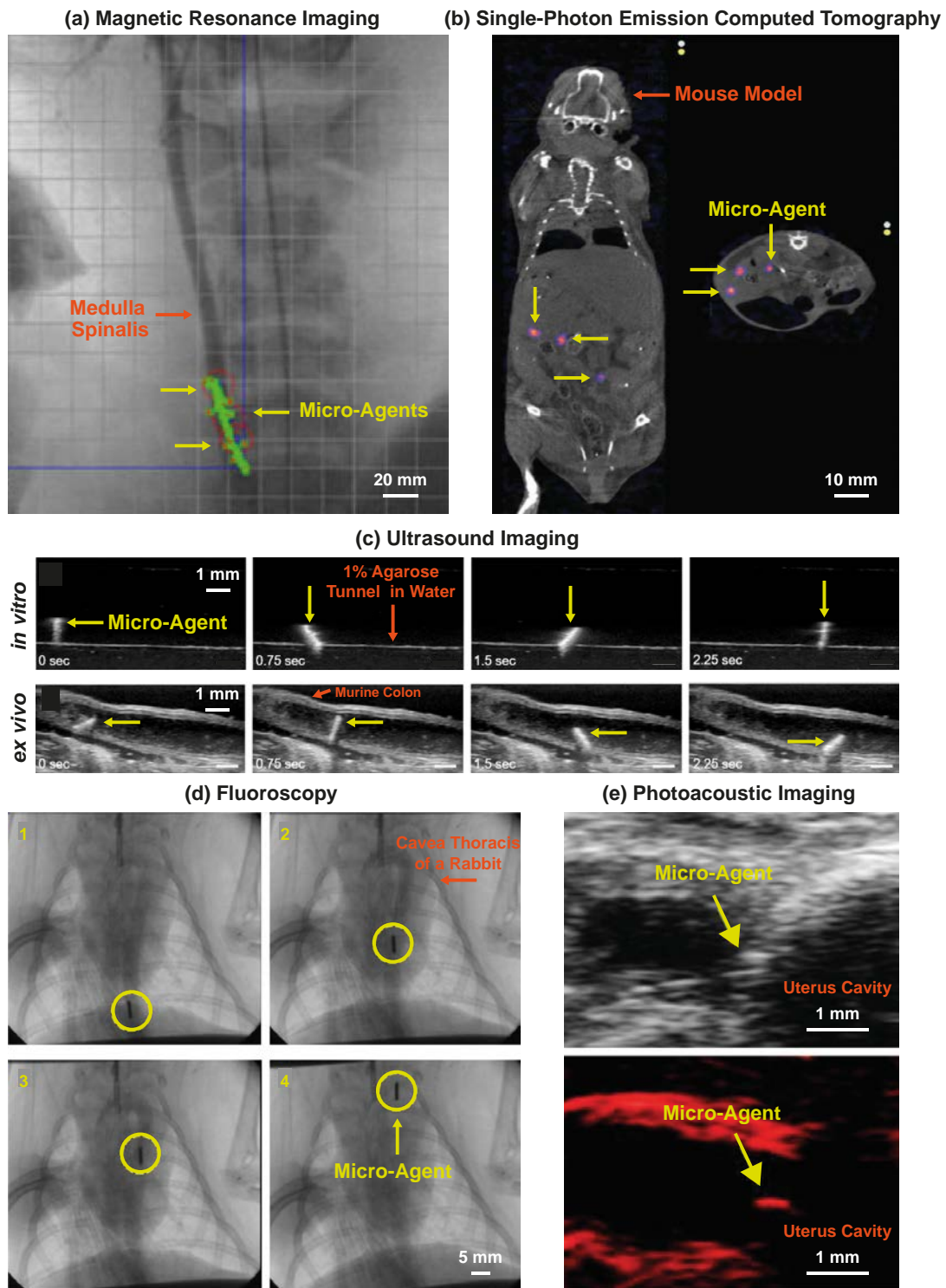


Figure 1.4: Visualization of micro-agents using medical imaging modalities. (a) Magnetic resonance image showing the motion of micro-agents in a blood vessel [55]. (b) Single-photon emission computed tomography of the micro-agents containing a radioactive compound inside the mouse [56]. (c) Ultrasound images show the tumbling motion of micro-agents under *in vitro* and *ex vivo* conditions [66]. (d) The fluoroscopic image sequence shows the movement of a micro-agent in a rabbit aorta [31]. (e) Photoacoustic versus ultrasound imaging of a micro-agent inside a tissue [65].

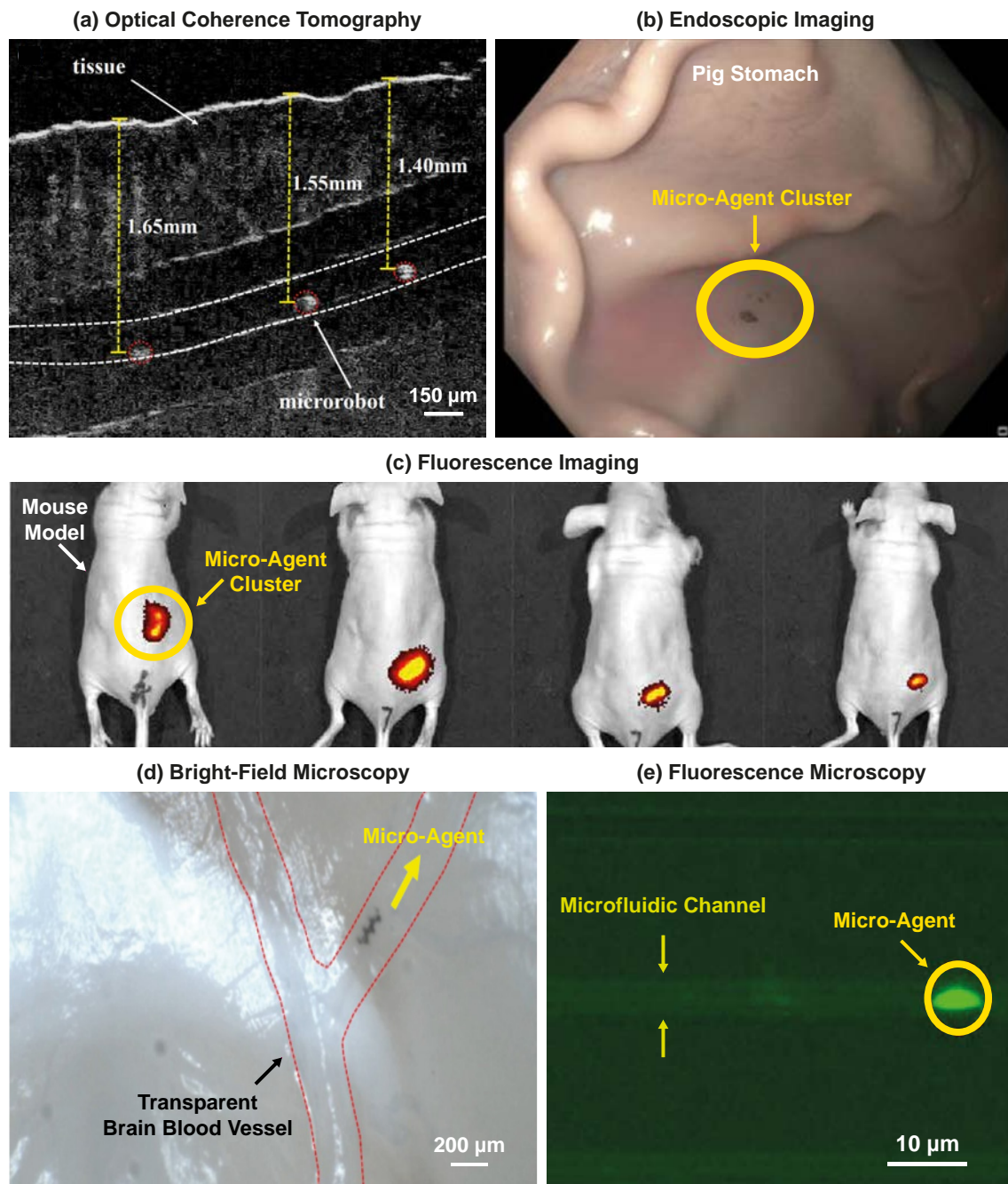


Figure 1.5: Visualization of the micro-agents using optical imaging techniques. (a) Optical coherence tomography image of a micro-agent inside the tissue [67]. (b) Visualizing a micro-agent cluster on the surface of a pig stomach with an endoscopic system [68]. (c) *In vivo* fluorescence imaging of the micro-agents in a mouse [69]. (d) Bright-field imaging of a micro-agent inside a decellularized vessel [71]. (e) Single-band fluorescence microscopy for a micro-agent in a channel [77].

in real-time by color assignment to spectrally resolved images using multicolor microscopy. Fabrication, imaging, and actuation setups are designed and assembled to demonstrate that real-time multicolor microscopy provides the required clear visualization for a wide range of microrobotics applications. The following section explains the working principle of multicolor fluorescence microscopy in detail.

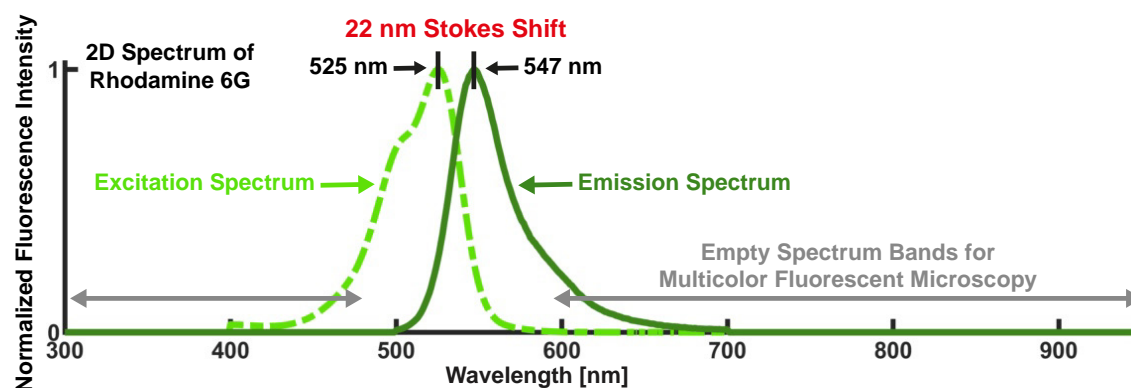


Figure 1.6: 2D ultraviolet-visible-near Infrared spectrum of a fluorescent dye (Rhodamine 6G). The spectrum data is downloaded from SpectraViewer (Thermo Fisher Scientific Inc., USA).

1.2 Multicolor Fluorescence Microscopy

The working mechanism of the multicolor fluorescence microscopy technique is based on staining a sample using fluorophores with different spectral characteristics [78, 79]. A fluorophore is a chemical compound that absorbs the incoming light at a specific wavelength, defined as excitation wavelength, and emits light at a longer wavelength, defined as emission wavelength. Although the overlap between excitation and emission spectrum exists, there is a difference between peak wavelengths, known as the Stokes shift (Fig. 1.6). In order to perform fluorescence imaging, non-overlapping excitation and emission wavelength ranges are selected using optical filters. Thus, excitation light is blocked and only emitted fluorescence light is collected for spectrally resolved image formation. Relatively narrow wavelength ranges for excitation and emission enable image acquisition from different spectrum bands using multiple fluorophores. Acquired spectrally-resolved images are overlaid to form a single multicolor image upon assigning the pseudo-colors (color coding), which render identification, discrimination, and tracking of each micro-component in a sample [80].

A wide range of fluorophore combinations is available to visualize an entire sample with color-coding. Conventional fluorescent dyes, endogenous fluorophores, and fluorescent proteins have a relatively small Stokes shift, emit light between the ultraviolet to near-infrared spectra, and allow image formation with up to six colors [81–83]. Since the current fluorophore technology is optimized for single-band fluorescence microscopy, it puts a color barrier for multicolor microscopy [84]. In order to break the color barrier, fluorophore groups that can be excited with the same wavelength range and have different emission spectrums hold potential [85]. Another appealing remedy for breaking the color barrier is quantum dots, which are excited with ultraviolet light and have tunable emission spectra [86]. Excitation of multiple fluorophores (including quantum dots) with the same wavelength range enables performing multicolor microscopy up to ten colors and decreases the design complexity of the microscopes. Once the fluorophore combination is determined depending on the application and the number of wavelength bands (color channels), optical components are selected for microscope design. Multicolor image formation by efficiently collecting the emitted light requires matching the spectra of the fluorophore combination and microscope components (e.g., light sources, imaging sensors, dichroic beam splitters, filters, lenses) [87].

Widefield [88], total internal reflection (TIRF) [89], confocal [90], light sheet [91], and two-photon microscopes [92] have been designed to acquire multicolor fluorescence

images using diverse fluorophore groups. Widefield microscopes form multicolor images by simultaneously exciting the fluorophore molecules in samples along the illumination path. TIRF microscopes generate thinner optical sections than widefield microscopes to decrease blurring effects in the formed multicolor fluorescence images. In contrast to TIRF and widefield microscopes, confocal microscopes use point illumination (via a spatial pinhole) to block out-of-focus fluorescence light and render image formation with higher contrast. Light sheet microscopes scan samples with optical sectioning and allow multicolor image formation with a higher speed than confocal microscopes. Compared to other microscopes, two-photon microscopes excite the fluorophores using near-infrared femtosecond lasers for multicolor image acquisition from deeper inside the tissue (up to 1.6 mm). Regardless of their design, multicolor microscopes often excite fluorophores simultaneously or sequentially to acquire spectrally resolved images.

Simultaneous excitation of the fluorophores ensures image acquisition without delay through a common optical path [79, 93]. Since combining multiple fluorophores induce spectral overlap, simultaneous excitation leads to crosstalk and disables the coding of a micro-object using a unique color. Sequential excitation of the fluorophores overcomes the crosstalk by wavelength multiplexing and provides spectrally resolved images containing direct segmentation of each micro-object for unambiguous color-coding [94]. However, the specific time interval between each spectrum band causes a lower rate of multicolor image acquisition with sequential excitation than simultaneous excitation. Based on the details provided regarding multicolor microscopy, the following section presents the research questions tackled in this doctoral study to design an imaging system for microrobotics.

1.3 Research Objectives

R.Q. 1 How to acquire visualization of mobile micro-agents and dynamic surroundings with encoded information for clear visualization?

The field of microrobotics benefits from the advances in micro/nano-fabrication technologies [25, 95]. Although micro-agents with intricate geometries can be fabricated, size limitations create a barrier to sensor integration. Therefore, imaging modalities have been employed as external sensors to validate the functionalities of the micro-agents. In the literature, samples containing micro-agents have been visualized using medical (e.g., magnetic resonance imaging, fluoroscopy, ultrasound) [53, 56, 65, 96, 97] and optical imaging techniques (e.g., optical coherence tomography, bright-field, fluorescence) [67, 71, 98]. Acquired images provide spatial resolution for manipulation of the micro-agents to desired targets. However, they do not contain information on the identification of micro-agents, targets, and surrounding media, which are the three main components for the manipulation. Besides, images are often acquired with a grayscale colormap, which hinders the distinction of the micro-agents from physical surroundings [31, 65, 67]. Encoding each manipulation component with a visual cue can facilitate recognition, localization, and tracking, enabling the necessary clear visualization. This doctoral thesis first introduces a microscopy technique that generates images fully encoded with a visual cue for the application domain of microrobotics.

R.Q. 2 How to design a real-time multicolor fluorescence microscope for magnetic microrobotics applications?

Performing multicolor fluorescence microscopy for microrobotics has four challenges. (1) Real-time multicolor image acquisition (> 3 frames per second) by relatively fast spectrum band changing (multiplexing) is an essential request in microrobotics. (2) There might be height differences between micro-agents and surroundings. The multicolor microscope should allow focused image acquisition from different planes to correct blur associated with the height differences. (3) Fluorophores have a limited lifespan, and the intensity of emitted photons decreases during the image acquisition due to photobleaching. Excitation with minimal time interval is necessary to prolong the imaging duration [93]. (4) The combination of multiple fluorophores leads to crosstalk due to overlap in excitation and emission spectra [99]. Crosstalk disables unambiguous identification by rendering micro-objects visible in more than one spectrum band. Research conducted in this dissertation addresses these challenges to develop a multicolor microscope for microrobotics applications. The microscope is employed to visualize samples containing magnetically-actuated micro-agents.

R.Q. 3 How to build a coil driver for magnetic manipulation of the micro-agents?

Only commercial drivers have been used to manipulate the micro-agents by powering the electromagnetic coils [32, 100–104]. Most drivers amplify pulse width modulation (PWM) signals to generate the magnetic field intensity in a controlled manner. The effect of PWM frequency on the magnetic field generation has not been considered in the actuation systems. Besides, the drivers are designed for applications requiring relatively low PWM frequencies. Magnetic fields with relatively high frequencies have been employed in the applications such as controlled drug release from the therapeutic micro-agents. A coil driver for both manipulation and release decreases the complexity of the actuation systems designed for targeted drug delivery using micro-agents. This

thesis fills the gap in the literature by presenting (1) a driver architecture to power the coils with higher PWM frequencies compared to conventional drivers and (2) PWM frequency selection for the coil used in the magnetic manipulation. Multiple drivers are built and coupled with an electromagnetic coil array to manipulate micro-agents. In order to obtain automated quantitative data about the micro-agents as well as the non-magnetic organic bodies mobilized by the micro-agents, a visual tracker is implemented.

R.Q. 4 How to visually track magnetically-actuated micro-agents without using specific detection and thresholding procedure?

In most studies, micro-agents are tracked with various imaging modalities to verify their functionality, provide feedback for the controllers and obtain quantitative information [105–108]. The tracking methods used in the literature indicate a two-stage pattern: micro-agents detection in each frame and application of the Kalman filter for noise cancellation. This pattern is prone to failure since detecting micro-agents in each frame is not feasible due to the lack of robustness and complex image dynamics. Besides, detection methods require thresholding procedures, and values change by image. The detection fails unless the thresholding values are appropriately tuned. When the detection stage fails, the Kalman filter can not accurately estimate the positions of the micro-agents. This thesis presents a visual tracking framework to overcome the shortcomings in the tracking methods for the micro-agents. It is demonstrated that the framework can track the micro-agents without a specific detection and thresholding.

1.4 Thesis Outline

This doctoral thesis is organized to address the stated research questions in three parts containing five chapters. **Part I (Chapters 2-4)** presents the scientific tools for microscopy, actuation, and tracking. A widefield fluorescence microscope is developed to excite the fluorophores in a round-robin manner and synchronously acquire spectrally resolved images. **Chapter 2** addresses **R.Q. 2** by describing the optical and electronics layout of the developed multicolor microscope. A tumor environment is created by placing cancer cell spheroids and polystyrene beads as surrogates for therapeutic micro-agents in a microfluidic channel. The tumor environment is used as an experimental testbed to validate that multicolor microscopy provides spectrally resolved image acquisition of micro-agents, organic bodies (cancer cell spheroids), and surrounding media (microfluidic channel). Experiments are devised to demonstrate that the round-robin image acquisition strategy (1) delineates spatial compartments without crosstalk, (2) reduces photodamage on the fluorophores for prolonging imaging time, and (3) permits real-time multicolor microscopy by relatively fast spectral multiplexing.

Chapter 3 provides an answer for **R.Q. 3** and presents the electronic system of the coil driver, designed to actuate micro-agents using field gradients or rotating fields. The driver is tested by studying the effect of varying pulse width modulation (PWM) frequencies on ohmic loss, current, and magnetic field. Besides, finite element simulations are performed to visualize field fluctuation and force acting on a permanent magnet at varying PWM frequencies. **Chapter 4** addresses **R.Q. 4** and introduces template-based visual tracking of micro-agents using the sum of squared differences and normalized cross-correlation cost functions. In template-based tracking, a micro-agent is localized once and tracked by computing its motion parameters between two consecutive frames. The performance of the template-based tracker is demonstrated by tracking micro-agents with different

geometries in 2D ultrasound and bright-field microscope images. Additionally, multi-rate state estimation is applied to obtain intersample states of the micro-agents between two consecutive measurement instants. The output of the visual tracker is provided as a measurement to the state estimators for upsampling the actual image acquisition rate.

The tools developed in **Part I (Chapters 2-4)** are used in **Part II (Chapter 5)** to report the performance of real-time multicolor microscopy through experiments in which micro-agents are manipulated using magnetic fields. For the experiments, fluorescent and magnetic micro-agents at varying aspect ratios are fabricated using the electrospinning technique. **Chapter 5** answers **R.Q. 1** by visualizing the fabricated micro-agents within an open reservoir, 3D tumor-on-a-chip, and vasculature networks. Various imaging experiments are conducted to validate that multicolor microscopy generates color-coded images in real-time for mobile micro-agents and dynamic surroundings. A microfluidic chip is developed to achieve the following: (1) Immobilizing a single cancer spheroid in a fixed location for micro-agent attachments. (2) Establishing a stable and controllable platform for multicolor image acquisition. (3) Maintaining micro-agents attached spheroids for dynamic and long-term multicolor image acquisition. Single and cluster micro-agents are attached to immobilized cancer cell spheroids in the chip as a proof-of-concept targeted drug delivery demonstration. In order to demonstrate that multicolor microscopy provides spectrally resolved visualization of the micro-agents within vascularized environments, two experimental testbeds are employed: (1) *in vitro* perfusable vascular network engineered on a microfluidic system and (2) *ex ovo* chorioallantoic membrane of the chick embryo.

Part III (Chapter 6) concludes this thesis by connecting the main findings in **Chapters 2-5** with the envisioned microrobotics applications. **Chapter 6** presents future directions regarding the fabrication of micro-agents containing drug particles, visualizing drug release using live-cell imaging, and performing multicolor microscopy under *in vitro* conditions.

1.5 Research Framework and Scientific Outputs

The research project presented in this thesis has been supported by the European Research Council under the European Union's Horizon 2020 Research and Innovation programme under Grant 638428—project ROBOTAR: Robot-Assisted Flexible Needle Steering for Targeted Delivery of Magnetic Agents. The scientific tools (multicolor fluorescence microscope, electrospinning setup, orthogonal array of four iron-core electromagnetic coils with drivers) are assembled at the Surgical Robotics Laboratory – Laser and Imaging Lab SRL-LIL, Department of Biomechanical Engineering, University of Twente, Enschede, the Netherlands. All the experiments have been carried out at the SRL-LIL. Polymer solutions for fluorescent and magnetic micro-agent fabrication using the electrospinning technique have been prepared at the Histology Laboratory at the University of Twente. The microfluidic channel molds have been fabricated at the Nanolab facility of the MESA+ at the University of Twente. Cancer cell spheroids, *in vitro* vascular network, and *ex ovo* chick embryo have been prepared by the Vascularization Laboratory, Department of Biomechanical Engineering, University of Twente, the Netherlands. The context of this doctoral thesis has been created with the following journal papers and conference proceedings published or under review:

Peer-Reviewed Journal Papers

- **M. Kaya**, U. Sakthivel, I. S. M. Khalil, and S. Misra, “Development of a Coil Driver for Magnetic Manipulation Systems”, *IEEE Magnetics Letters*, 10(1), pages 1–5,

December 2019.

- **M. Kaya**, F. Stein, J. Rouwkema, I. S. M. Khalil, and S. Misra, “Serial Imaging of Micro-Agents and Cancer Cell Spheroids in a Microfluidic Channel using Multicolor Fluorescence Microscopy”, *PLoS One*, 16(6), e0253222, June 2021.
- S. Mohanty, R. J. Fidler, P. Mendes, C. M. Heunis, **M. Kaya**, N. Blanken, and S. Misra, “SonoTweezer: An Acoustically-Powered End-Effector for Underwater Micromanipulation”, *IEEE Transactions on Ultrasonics, Ferroelectrics, and Frequency Control*, 69(3), pages 988–997, March 2022.
- **M. Kaya**, F. Stein, P. Padmanaban, Z. Zhang, J. Rouwkema, I. S. M. Khalil, and S. Misra, “Visualization of Micro-Agents and Surroundings by Real-Time Multicolor Fluorescence Microscopy”, *Nature Scientific Reports*, 12(13375), August 2022.
- M. Richter, **M. Kaya**, J. Sikorski, L. Abelmann, V. K. Venkiteswaran, and S. Misra, “Magnetic Soft Helical Manipulators with Local Dipole Interactions for Flexibility and Forces”, *Soft Robotics*, 2022 (Under Review).
- V. D. Trikalitis, N. J. J. Kroese, **M. Kaya**, C. C. Fabres, S. ten Den, I. S. M. Khalil, S. Misra, B. Koopman, R. Passier, V. Schwach, and J. Rouwkema, “Embedded 3D Printing of Dilute Particle Suspensions into Complex Organoid Fibers”, *Biofabrication*, 2022 (Under Review).
- L. Capuano, J. J. J. Huaroto, I. Hlukhau, **M. Kaya**, S. Mohanty, F. C. C. Assayag, G. W. Romer, and S. Misra, “Two-Photon Microscopy for Visualizing Micro-Robotic Agents Within Biological Tissue”, in preparation, will be submitted to *Applied Physics Letters*.

International Conference Proceedings

- A. Denasi, F. Khan, K. J. Boskma, **M. Kaya**, C. Hennersperger, R. Gobl, M. Tirindelli, N. Navab, and S. Misra, “An Observer-Based Fusion Method using Multicore Optical Shape Sensors and Ultrasound Images for Magnetically-Actuated Catheters”, in *Proceedings of the IEEE International Conference on Robotics and Automation (ICRA)*, pages 50–57, Brisbane, Australia, May 2018.
- **M. Kaya**, A. Denasi, S. Scheggi, E. Agbahca, C. Yoon, D. H. Gracias, and S. Misra, “A Multi-Rate State Observer for Visual Tracking of Magnetic Micro-Agents using Slow Medical Imaging Modalities”, in *Proceedings of the IEEE/RSJ International Conference on Intelligent Robots and Systems (IROS)*, pages 1-8, Madrid, Spain, October 2018.



Scientific Tools

2	Multicolor Fluorescence Microscope .	35
2.1	Introduction	
2.2	Materials and Methods	
2.3	Results	
2.4	Conclusions	
3	Electromagnetic Coil Driver	57
3.1	Introduction	
3.2	Coil Driver	
3.3	Experiments	
4	Template-Based Visual Tracking	67
4.1	Introduction	
4.2	Visual Tracking of Magnetic Micro-Agents	
4.3	Multi-Rate State Estimation	
4.4	Collaborative Tracking using Observers	
4.5	Experiments	
4.6	Conclusions	

PREFACE

Multicolor fluorescence microscopy is a powerful imaging technique that enables the visualization of complex and dynamic biological systems by encoding spatial compartments with colors. Generating color-coded images, which helps make micro-objects distinguishable, is the unique feature of multicolor microscopy compared to other imaging techniques, including magnetic resonance imaging, computed tomography, and ultrasound. **Part I (Chapters 2-4)** of this doctoral thesis combines multicolor microscopy with the field of microrobotics and introduces custom-made scientific tools to track magnetic agents by acquiring color-coded images. The research conducted in the first part starts with presenting a multicolor microscope developed for visualizing micro-agents and physical surroundings by spectral resolving. The microscope is designed using a 3D non-vascularized tumor model for the envisioned microrobotics application of drug delivery.

The tumor model is created by randomly placing cancer cell spheroids and polystyrene beads as surrogates for therapeutic agents in a microfluidic channel. A microscope design to be used in manipulation by acquiring color-coded visualization of end-effector (micro-agents), target (spheroids), and path (surrounding media) requires the identification of three considerations. (1) Visualization of mobile micro-agents and dynamic surroundings demands real-time multicolor microscopy, which is possible with relatively fast image acquisition from different spectrum bands using a common optical path. (2) There is a height difference between the micro-components in the tumor model. Focused spectrally resolved image acquisition from multiple planes is necessary to generate multicolor fluorescence images without blur caused by height differences. (3) Optical elements in the microscope are selected according to the fluorophores, which render agents, spheroids, and channels visible in different spectrum bands. Fluorophores with fairly well-separated spectrum characteristics and relatively high photobleaching resistance are also essential for real-time multicolor image acquisition without crosstalk. **Chapter 2** explains the multicolor fluorescence microscope development by addressing these considerations.

The multicolor microscope provides a relatively large working space to integrate actuation systems that mobilize micro-agents using external stimuli. Magnetic fields, widely preferred external stimuli, are employed to acquire real-time multicolor fluorescence images containing mobile micro-agents. Time-varying magnetic fields for the remote actuation are generated in a controlled manner using a coil array. **Chapter 3** describes a circuit architecture to power the coils by amplifying pulse width modulation (PWM) signals and details the driver design requirements for magnetic manipulation systems. PWM is a commonly used technique to control the magnetic field intensity since it has the advantage of relatively high efficiency, low power losses, and noise immunity. The architecture allows powering the coils with higher PWM carrier frequencies than the commercial drivers used in magnetic manipulation studies. Various coil types are powered with the driver to show the relationship between PWM carrier frequency and fluctuations in the magnetic field, which has never been questioned in prior works. In order to extract automated quantitative information about magnetic actuation from the multicolor fluorescence images, a visual tracker is implemented.

Chapter 4 proposes a framework for tracking mobile micro-agents regardless of their shapes. The working mechanism of the framework is computing motion parameters

between the previous appearance and the recently collected image of a micro-agent. Computing motion parameters enable tracking of micro-agents without any detection and thresholding procedure. Visual tracking methods are prone to failure due to complex image dynamics, sudden changes, and residual error in the optimization. Multiple experiments show that the framework is resilient to quick intensity changes, abrupt motions, and drift caused by residual error accumulation. The tracking framework is combined with multi-rate state estimation to (virtually) increase the position information between two consecutive frames. This method provides a remedy for upsampling the position measurement of micro-agents in case images can not be acquired fast enough.

2. Serial Imaging of Micro-Agents and Cancer Cell Spheroids in a Microfluidic Channel using Multicolor Fluorescence Microscopy

Note: The following content is an adapted version of the paper "Serial imaging of micro-agents and cancer cell spheroids in a microfluidic channel using multicolor fluorescence microscopy" by **M. Kaya**, F. Stein, J. Rouwkema, I. S. M. Khalil, and S. Misra published in "*PLoS One*", 16(6), e0253222, June 2021. ■

Abstract

Multicolor fluorescence microscopy is a powerful technique to fully visualize many biological phenomena by acquiring images from different spectrum channels. This study expands the scope of multicolor fluorescence microscopy by serial imaging of polystyrene micro-beads as surrogates for drug carriers, cancer spheroids formed using HeLa cells, and microfluidic channels. Three fluorophores with different spectral characteristics are utilized to perform multicolor microscopy. According to the spectrum analysis of the fluorophores, a multicolor widefield fluorescence microscope is developed. Spectral crosstalk is corrected by exciting the fluorophores in a round-robin manner and synchronous emitted light collection. To report the performance of the multicolor microscopy, a simplified 3D tumor model is created by placing beads and spheroids inside a channel filled with the cell culture medium is imaged at varying exposure times. As a representative case and a method for biohybrid drug carrier fabrication, a spheroid surface is coated with beads in a channel utilizing electrostatic forces under the guidance of multicolor microscopy. Our experiments show that multicolor fluorescence microscopy enables crosstalk-free and spectrally-different individual image acquisition of beads, spheroids, and channels with the minimum exposure time of 5.5 ms. The imaging technique has the potential to monitor drug carrier transportation to cancer cells in real-time.

2.1 Introduction

The functionalization of tetherless manipulatable micro-agents as drug carriers offers a remedy for required dose delivery to cancer cells. Microfluidic channels have been used as a controlled experimental environment to validate the effectiveness of such micro-agents [109, 110]. Since the channels are fabricated using optically transparent materials, microscopy is the most widely used method for imaging [111]. Among the microscopy techniques, fluorescence microscopy is the most effective way to visualize a specific target structure with a relatively high contrast-to-noise ratio by eliminating the background. In the literature, only micro-agents are imaged and localized using single-band fluorescence microscopy [14, 60, 70, 77, 98, 112, 113]. To study the drug transportation mechanism using micro-agents, imaging and localization of cancer cells and channels are also required. In this study, a multicolor widefield fluorescence microscope is developed to serially acquire images of micro-agents, cancer cells, and microfluidic channel. The main contribution of this study is that multicolor fluorescence microscopy is applied for spectrally-different and high-contrast visualization to monitor the interaction between micro-agents and cancer cells in a channel.

In numerous application domains ranging from single-cell visualization to rapid diagnosis, multicolor fluorescence microscopy is recognized as a key emerging technology [79, 81, 88, 93, 114–122]. The working principle of this microscopy technique is based on performing imaging using spectrally-different conventional fluorescent dyes [88], endogenous fluorophores [81], fluorescent proteins [123], or quantum dots [124]. Relatively narrow excitation and emission wavelength ranges enable image acquisition from different spectrum bands with multiple fluorophores. Acquired spectrally-different images, defined as individual fluorescence images, are overlaid to form a multicolor fluorescence image. Different configurations are developed to perform multicolor fluorescence microscopy. The simplest way is to collect multicolor images using a combination of an imaging sensor and single-band filters. Individual fluorescence images are collected by changing the filters with different bandwidths [116, 125]. However, performing imaging by positioning the filters either manually or using a motorized drive creates a delay and limits the image acquisition rate. An appealing solution for stationary components is to use a multi-band emission filter [88, 120]. Since the delay associated with the spectrum band change is removed, the acquisition is limited by the frame rate of the imaging sensor. Depending on the spectrum of the fluorophores, the acquired images suffer from crosstalk [119]. To minimize the crosstalk, emitted light from the fluorophores is separated using dichroic mirrors and direct to individual imaging sensors using a common optical path [79, 81, 114, 115, 121]. Under simultaneous excitation of the fluorophores, the individual images still contain crosstalk due to the overlapping of emission spectra [93]. To overcome crosstalk, our multicolor microscope is configured to excite one fluorophore at a time and synchronously trigger the designated camera for individual image acquisition. We experimentally validate that the crosstalk is corrected by the assignment of emitted light from each fluorophore to the specified camera.

For imaging experiments, cancer cell spheroids with a diameter of 200 μm are formed using HeLa cells and placed inside a microfluidic channel filled with cell culture medium to create a simplified 3D tumor model. Polystyrene beads with a diameter of 20 μm are employed as surrogates for drug carriers and injected in the channel [5, 126, 127]. In our simplified tumor model, there are height differences between beads, spheroids, and channel. To form focused multicolor fluorescence images using widefield microscopy, individual image acquisition from different focal planes is required. Since micro-structures in the pre-

viously used samples have almost the same height, defocus correction is not addressed for widefield multicolor imaging [78, 88, 121, 128]. In this study, our multicolor fluorescence microscope is specially developed for defocus correction by spectrally-different image acquisition from multiple focal planes within the simplified tumor model. Fluorescein, CellTracker Red CMTPX, indocyanine green, fluorophores with different spectral properties, are used to render beads, spheroid, and channel visible by fluorescence imaging, respectively. Spectrum analysis of the fluorophores is carried out using a spectrofluorometer to determine effective wavelength ranges for excitation and fluorescence photon emission. Fluorophores are excited in a round-robin manner, and acquired individual images in one-round are overlaid to form time-lapse multicolor images. The achievable maximum multicolor image acquisition rate using the round-robin method is measured by exposure time analysis. Photobleaching curves of the fluorophores are studied to determine the duration of the multicolor imaging. To demonstrate the application of the microscope for the investigation of drug targeting, HeLa cell spheroids are coated with micro-beads utilizing electrostatic forces. An optical flow method is used to compute motion information between consecutive time-lapse images. Our experiments show that multicolor fluorescence microscopy enables more information collection for localization and providing feedback by image acquisition from multiple spectrum bands compared to bright-field and single-band fluorescence microscopy.

2.2 Materials and Methods

2.2.1 Spectrum Analysis

Excitation and emission spectrum of the fluorophores are measured using a spectrofluorometer (FP-8300, Jasco, Japan) in the range of 200 nm and 900 nm with 1 nm data interval. For spectrum analysis, 2.5 μM indocyanine green (I2633-25MG, Sigma-Aldrich, USA) solution is prepared by dissolving 1.5 μg indocyanine green in 700 μL fetal bovine serum (16000044, Thermo Fisher Scientific, USA). The solution is placed in a water bath at 37°C for 2 hours to bind indocyanine green to proteins in the culture medium [129]. A 10 μM working CellTracker Red CMTPX (Thermo Fisher Scientific, USA) solution is prepared in a serum-free medium by mixing 50 μg CMTPX dye in the vial with 7.29 μl dimethyl sulfoxide (D2650-100ML, Sigma-Aldrich, USA). Micro-beads stained with fluorescein (42-00-204, Micromod, Germany) are obtained in a solution form. 2 μL CMTPX and micro-beads solutions are diluted with 700 μL Milli-Q water and placed in quartz cuvettes (CV10Q700F, Thorlabs, USA) for the analysis. The spectrum graphs are illustrated in Fig. 2.1-(a). The peak excitation and emission wavelengths are measured as 492 nm and 513 nm for fluorescein, 583 nm and 611 nm for CMTPX, and 773 nm and 799 nm for indocyanine green, respectively. The multicolor widefield fluorescence microscope is developed based on the spectrum analysis for effective excitation of the fluorophores and accurate emitted light collection.

2.2.2 Multicolor Fluorescence Microscope Architecture

The microscope consists of illumination and emission units. The illumination unit generates discrete light beams with the center wavelengths of 470 nm, 565 nm, and 780 nm for sharp excitation of the fluorophores using three individual narrow-spectrum light-emitting diodes (LEDs) (M470L3, M565L3, M780LP1, Thorlabs, USA). The spectrum of LEDs is plotted in Fig. 2.1-(f). LEDs are collimated using 20 mm focal length aspheric condenser lenses (ACL2520U-A, ACL2520U-B, Thorlabs, USA) and coupled with filters (ET470/40x,

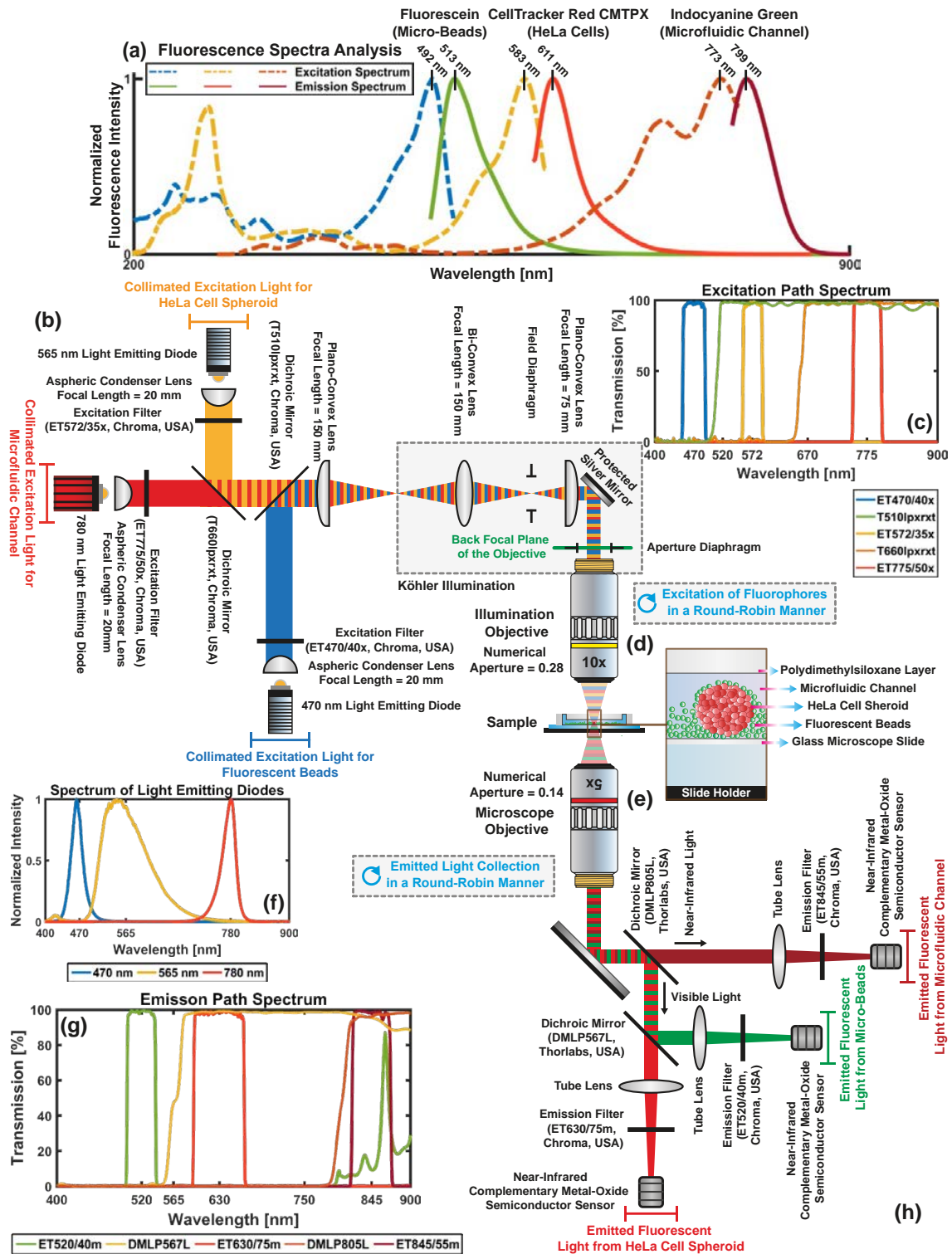


Figure 2.1: Optical layout of the multicolor fluorescence microscope developed for monitoring interaction between polystyrene micro-beads as surrogates for drug carriers and cancer cells in a microfluidic channel. (a) Two-dimensional excitation and emission spectrum of fluorescein, CellTracker Red CMTX, and indocyanine green measured by a spectrofluorometer in the range of 200 nm and 900 nm. The peak excitation and emission wavelengths are shown with vertical lines. (b) and (h) Illumination and emission units. (c) and (g) Spectrum of excitation and emission paths, respectively. (d) and (e) Illumination and microscope objectives that employed for focusing excitation light on the sample and collection of emitted light from the fluorophores, respectively. (f) Spectrum of light-emitting diodes.

ET572/35x, ET775/50x, Chroma, USA) for selection of the excitation wavelengths. Generated three discrete and collimated light beams are combined using two dichroic mirrors (T660lpxrxt, T510lpxrxt, Chroma, USA) for excitation of the fluorophores using a single optical path. The spectrum for the excitation path is shown in Fig. 2.1-(c). Collimated light provides non-homogeneous illumination, which results in artifact formation in the acquired fluorescence images. To achieve uniform illumination, Köhler illumination is used [130]. Collimated light is focused for Köhler illumination using a 150 mm focal length plano-convex lens (LA1417, Thorlabs, USA). Köhler optics is constructed with the combination of a 150 mm focal length bi-convex lens (LB1374, Thorlabs, USA), a 75 mm focal length plano-convex lens (LA1145, Thorlabs, USA), and two iris diaphragms (SM2D25D and CP20S, Thorlabs, USA). The incoming light is first focussed and then collimated using bi-convex and plano-convex lenses, respectively. Images of the LED chips are obtained on the front focal plane of the plano-convex lens. A protective silver mirror (PF10-03-P01, Thorlabs, USA) is utilized to direct the collimated light. A 10x long working distance objective lens (Plan Apo, Mitutoyo, Japan) is employed to focus the excitation light on the sample. The objective is placed in a way that its back focal plane intersects with the image plane of LED chips. To control illumination area and intensity at the sample plane, two individual irises (i.e., field and aperture diaphragms) are placed to back focal planes of plano-convex and objective lenses, respectively. Emitted light from fluorophores is collected using a 5x long working distance objective (Plan Apo, Mitutoyo, Japan) and transmitted towards the emission unit by a protective silver mirror (PF20-03-P01, Thorlabs, USA). The emission unit separates the emitted fluorescence light into its spectral components for individual image formation of channels, HeLa cells, and micro-beads using two dichroic mirrors (DMLP567L and DMLP805L, Thorlabs, USA). Individual fluorescence light beams are directed onto tube lenses (ITL200, Thorlabs, USA) to form images onto complementary metal-oxide-semiconductor (CMOS) cameras (CS135MUN, DCC3240N, Thorlabs, USA). To block excitation light and select fluorescence wavelengths, emission filters (ET845/55m, ET623/60m, ET520/40m, Chroma, USA) are placed in front of the cameras. The spectrum for the emission path is plotted in Fig. 2.1-(g).

2.2.3 Demultiplexer Interface

Simultaneous excitation of the fluorophores leads to crosstalk between acquired fluorescence signals due to spectral overlap (Fig. 2.1). To prevent crosstalk, the microscope is coupled with a demultiplexer interface to excite fluorophores in a round-robin manner and synchronically acquire fluorescence images using two individual pulse trains. Multicolor fluorescence images are obtained by overlapping serially acquired images from three different spectrum ranges in one round. The demultiplexer interface architecture and timing diagram are illustrated in Fig. 2.2. Pulse train signals are generated using a dual-channel signal generator (33510B, Keysight, USA). A demultiplexer integrated circuit (74HC4052, Texas Instruments, USA) is used to distribute generated pulses to the corresponding LED driver (LEDD1B, Thorlabs, USA) and CMOS camera by channel selection using a microcontroller. Line drivers and voltage followers are connected to the inputs and outputs of the circuit to match the impedance and provide isolation, respectively.

2.2.4 Cell Culture and Spheroid Formation

HeLa cells are cultured in Dulbecco's modified Eagle's medium (11-965-092, Fisher Scientific Ltd. Canada), supplemented with 10% fetal bovine serum (F7524-500ML,

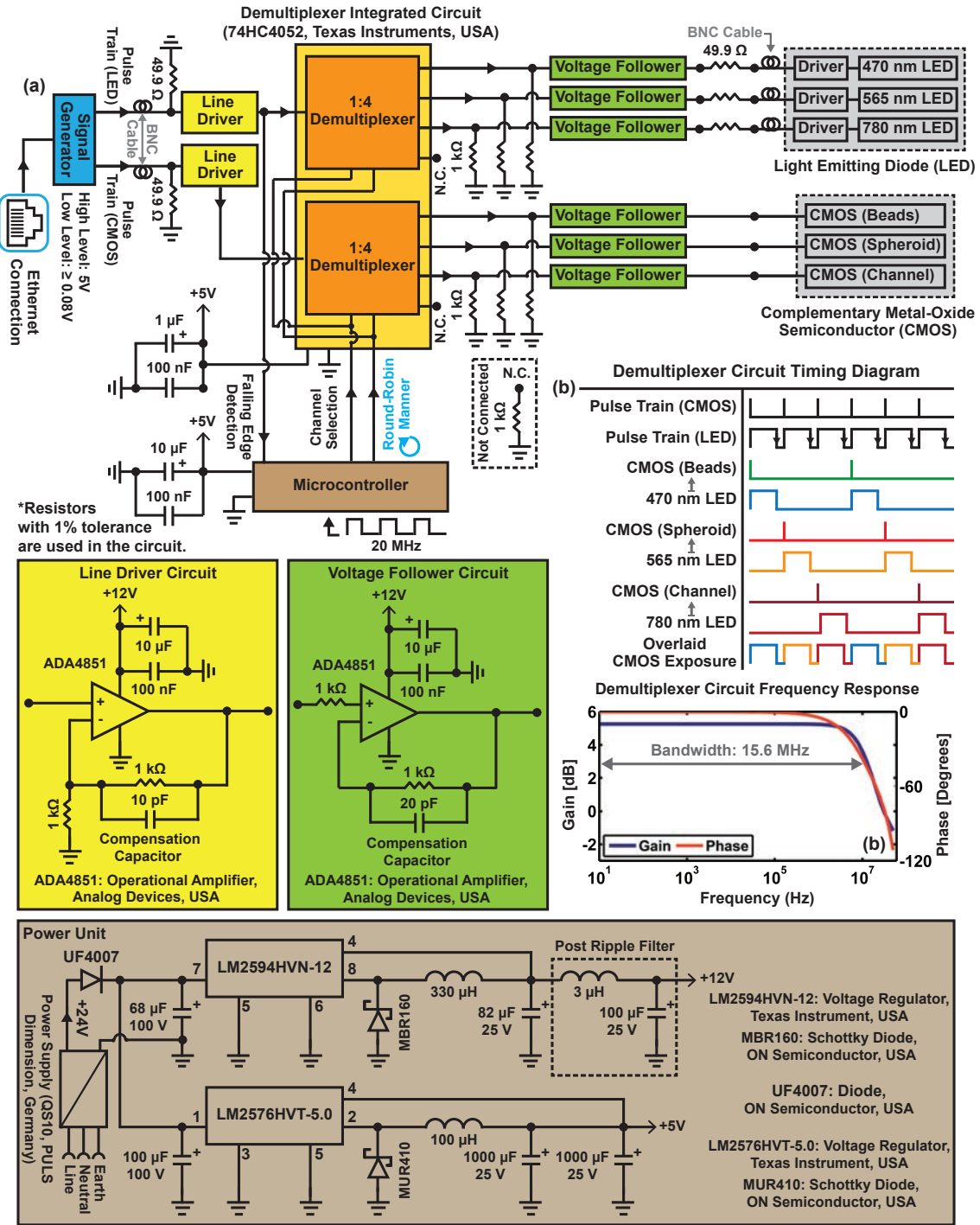


Figure 2.2: Demultiplexer Circuit Diagram. Schematic representation of the demultiplexer interface used for preventing crosstalk between fluorophores by synchronically triggering light-emitting diodes (LEDs) and complementary metal-oxide-semiconductor (CMOS) cameras in a round-robin manner using two individual pulse trains. (a and c) Architecture and computed frequency response plot of the demultiplexer circuit. (b) Timing diagram for input pulse trains generated using a signal generator (33510B, Keysight, USA) and output trigger signals for each LED and CMOS sensor combination.

Sigma-Aldrich, USA), and 1% penicillin-streptomycin (15-140-122, Thermo Fisher Scientific Inc., USA). During the culture period, the cells are maintained at 37°C in a humidified atmosphere containing 5% carbon dioxide. In the 2D cell culture, the medium is changed

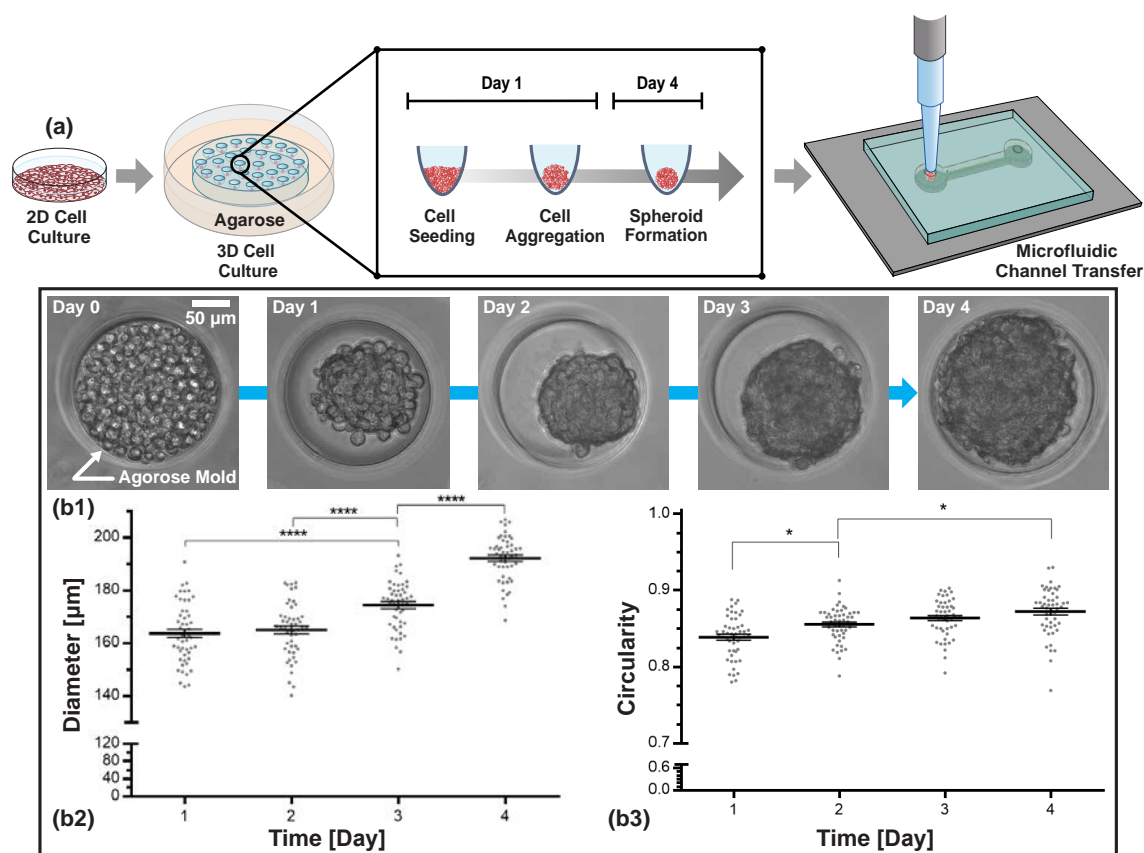


Figure 2.3: HeLa cell spheroid formation. (a) Schematic of cell spheroid formation in microwell array from micropatterned agarose well. (b) After the expansion of HeLa cells in standard tissue culture plates, cells were transferred into agarose microarrays for 3D cell spheroid formation with a diameter of 200 μm . Circularity and diameter of the spheroid versus time are plotted in (b2) and (b3), respectively.

every 48 hours. When cells reach 80% confluency, the cells are trypsinized, counted, and resuspended in cell culture medium at a concentration of 2×10^6 cells/ml. In the next step 0.2 mL of cell suspension is then placed on top of an agarose mold, which was previously placed in the well of a 12-well plate for spheroid formation (Fig. 2.3-(a)). This results in spheroids which on average contain approximately 270 cells. Half of the medium is replaced daily. For measuring the spheroid morphology, images are taken every day (Fig. 2.3-(b)). The measured spheroid perimeter is used to determine the average spheroid diameter by calculating the surface area.

2.2.5 Agarose Molds

Agarose microarrays for nonadherent 3D cell culture are formed by replica molding [131]. Elastomeric stamps of polydimethylsiloxane (PDMS) (Sylgard 184 Silicon Elastomer Kit, Dow Corning, USA) are molded over the SU-8 photoresist master. Before use, the stamps are sterilized by 30 minutes incubation in 70% ethanol (84010059.5000, Boom Lab, the Netherlands). Afterward, 3% agarose (weight/volume) (16500500, ultra-pure agarose, Invitrogen, USA) is cast onto the PDMS stamps and placed into 12-well round-bottom plates after polymerization. Each agarose mold contains 1500 microwells with depth and a diameter of 200 μm .

2.2.6 Cell Labelling using CMTPX and Fixation

The 10 μM CMTPX working solution is prepared in a serum-free medium and subsequently incubated for 30 minutes with the cells in monolayer and spheroids which have compacted for 3 days under cultivation conditions. Afterward, the working solution is removed, and the culture medium is added again. For long-term storage, HeLa cell spheroids stained with CMTPX are fixated for 15 minutes with 4% formaldehyde (F8775-25ML, Sigma-Aldrich, USA) at room temperature. This is followed by washing twice with Dulbecco's phosphate-buffered saline.

2.2.7 Microfluidic Channel Fabrication

To create a simplified 3D tumor model, HeLa cell spheroids stained with CMTPX are embedded in microfluidic channels with a height of 187 μm using a micropipette. The channels are fabricated using a standard soft lithography process [132]. Negative molds of microfluidic channels on a silicon wafer are prepared in the cleanroom using SU-8 photoresist. A mixture of 10:1 Sylgard 184 PDMS and the curing agent is poured onto the wafer and cured in the oven at 70°C overnight. The cured PDMS layer is gently removed from the wafer, and inlet-outlet ports are punched. Finally, the microfluidic channels are obtained by bonding the PDMS layer to a microscope slide using plasma-oxidation. For imaging experiments, the microfluidic channels are filled with 250 $\mu\text{g/ml}$ indocyanine green in the culture medium [133].

2.2.8 Image Acquisition

The image acquisition and post-processing software is implemented in MATLAB (version R2017b, Mathworks Inc., USA) and run on a 64-bit Windows 10 computer, which has an Intel(R) Core(TM) i7-6700 CPU running at 3.40 GHz and 32 GB of RAM. The signal generator is configured through Ethernet communication to generate pulse trains for external trigger and exposure time. 8-bit grayscale fluorescence images with the size of 1280 \times 1024 pixels captured by CMOS cameras are transmitted to the computer through the USB 3.0 interface. In our samples, micro-beads and microfluidic channels are located at different image planes with respect to HeLa cell spheroids due to height differences. For multicolor fluorescence microscopy, the objective lens is focused on the image plane of the spheroids. Focused fluorescence images of beads and channel are obtained by placing each camera at a calibrated distance away from the tube lenses [131]. In order to align the images, CMOS cameras are coupled with a combination of the kinematic mirror (KM200CP/M, Thorlabs, USA) and XY translation mounts (ST1XY-S/M, Thorlabs, USA) that allows pixel shift elimination by fine positioning. An overview of our microscope assembly is shown in Fig. 2.4.

2.3 Results

2.3.1 Multicolor Fluorescence Image Acquisition

We report the performance of the multicolor fluorescence microscope by imaging micro-beads and HeLa cell spheroids placed inside a microfluidic channel. Fig. 2.5-(a) and (b) show the multicolor imaging areas with 5x and 10 x objectives, respectively. Fluorophores are excited between 450 nm and 490 nm, 554.5 nm and 589.5 nm, and 750 nm and 800 nm, for fluorescein, CMTPX, and indocyanine green, respectively (Fig. 2.6-(a)). To acquire 8-bit individual grayscale images of beads, spheroids, and channel with the minimum noise level, emitted light from the fluorophores is collected with 0 dB gain and 66 ms

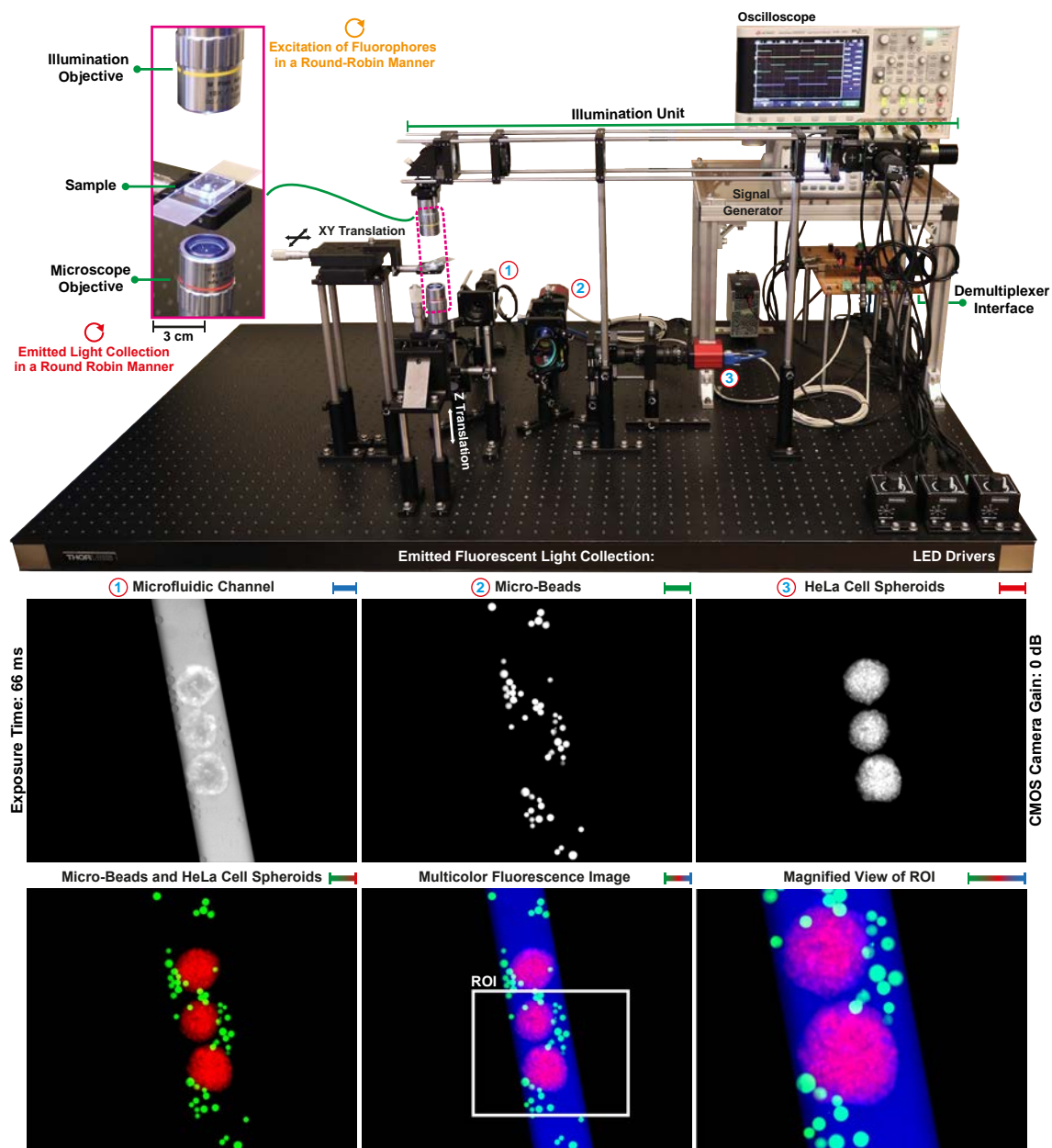


Figure 2.4: Multicolor fluorescence microscope used for real-time image acquisition of microfluidic channel, HeLa cell spheroids, and micro-beads in a round-robin manner. Scale bar: $100\ \mu\text{m}$.

exposure time in the wavelength ranges of $500\text{--}540\ \text{nm}$, $592.5\text{--}667.5\ \text{nm}$, and $817.5\text{--}875.5\ \text{nm}$, respectively. Multicolor fluorescence images are formed by overlapping acquired individual fluorescence images with dimensions of $1231\ \mu\text{m} \times 983\ \mu\text{m}$ (horizontal \times vertical). Fig. 2.6 shows multicolor image formation for two representative cases. Acquired individual grayscale images are shown in Fig. 2.6-(b)-(d) and formed multicolor images are shown in Fig. 2.6-(f). For visualization and interpretation of the multicolor images, intensity values in grayscale images of beads, spheroids, and channel are represented using black-green, black-red, black-blue color maps, respectively. To reveal further details in the multicolor images, the region of interests (ROIs) with dimensions of $521\ \mu\text{m} \times 417\ \mu\text{m}$ are magnified and shown in Fig. 2.6-(g). The channel contains higher beads concentration in Fig. 2.6-(g2) than Fig. 2.6-(g1). Although relatively high bead concentration leads

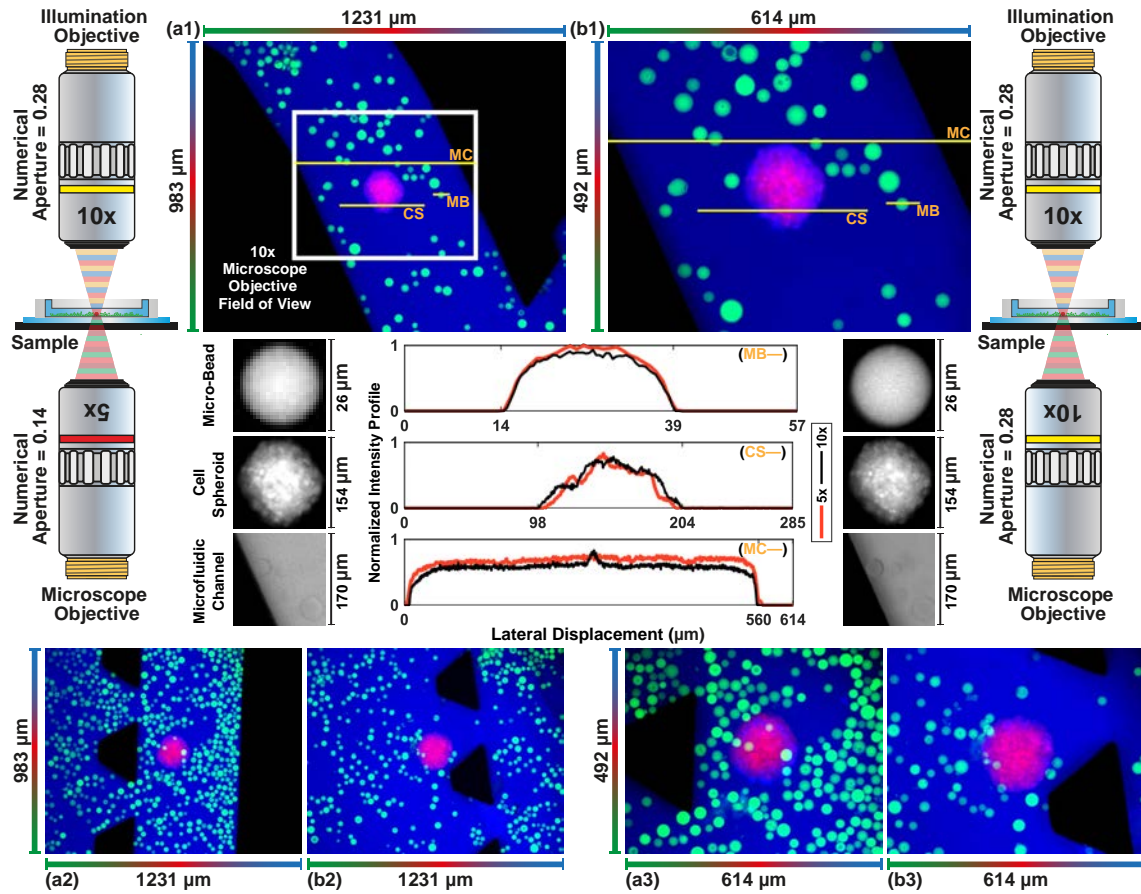


Figure 2.5: (a) and (b) Multicolor image formation using 5x and 10x microscope objectives, respectively.

to occlusion in the multicolor image (Fig. 2.6-(f2)), individual images include complete visualization of the beads, spheroids, and channel (Fig. 2.6-(b2)-(d2)). Our experiments validate that multicolor microscopy enables occlusion-free visualization of the sample by spectrally-different image acquisition.

2.3.2 Crosstalk Analysis for the Multicolor Fluorescence Microscopy

Crosstalk analysis is carried out to visualize the effect of excitation light and emitted fluorescence signals on the acquired individual fluorescence images [119, 134]. Fluorophores are excited with single, double, and triple combinations of the center wavelengths at 470 nm, 565 nm, and 775 nm. Emitted fluorescence signals are simultaneously acquired from 500–540 nm, 592.5–667.5 nm, and 817.5–875.5 nm spectrum bands for micro-beads, HeLa cell spheroids, and microfluidic channel, respectively. According to the status of the center wavelength, we observe the following:

- 470 nm: ON, 565 nm: OFF, 780 nm: OFF (Fig. 2.7-(a1)): Fluorescence signal emitted from beads is collected without crosstalk from the 500–540 nm band. Relatively low-level crosstalk makes beads and spheroid visible in the image acquired from 592.5–667.5 nm band. No crosstalk is observed at the image acquired from the 817.5–875.5 nm band.
- 470 nm: OFF, 565 nm: ON, 780 nm: OFF (Fig. 2.7-(a2)): No crosstalk is observed at the images acquired from the 500–540 nm and 817.5–875.5 nm bands. Fluorescence signal emitted from spheroid is collected without crosstalk from the 592.5–667.5 nm

band.

- 470 nm: OFF, 565 nm: OFF, 780 nm: ON (Fig. 2.7-(a3)) and 470 nm: OFF, 565 nm: ON, 780 nm: ON (Fig. 2.7-(a5)): No crosstalk is observed at the 500–540 nm band. Emitted light from the medium inside the channel is collected without crosstalk from the 817.5–875.5 nm band. The excitation light generated by 780 nm LED is collected from the 592.5–667.5 nm band and blocks the image acquisition.
- 470 nm: ON, 565 nm: ON, 780 nm: OFF (Fig. 2.7-(a4): Fluorescence image of beads is acquired from 500–540 nm band. The image acquired from the 592.5–667.5 nm band contain beads, spheroid, and channel as a result of crosstalk. Besides, excitation of CMTPIX by 470 nm LED results in increasing the fluorescence signal intensity emitted from spheroid Fig. 2.1-(a). No crosstalk is observed at 817.5–875.5 nm band.
- 470 nm: ON, 565 nm: OFF, 780 nm: ON (Fig. 2.7-(a6)) and 470 nm: ON, 565 nm: ON, 780 nm: ON (Fig. 2.7-(a7)): Spectrum analysis shows that there is no overlap between fluorescein and indocyanine green (Fig. 2.1-(a) and Fig. 2.6-(a)). However, the emission filter used for image acquisition of beads (ET520/40m, Chroma, USA) transmits the light with the wavelength range of 791–1000 nm (Fig. 2.1-(g)). Therefore, both beads and channel are visible at the image acquired from 500–540 nm. Excitation light generated by 780 nm LED blocks the image acquisition from 592.5–667.5 nm band. Fluorescence image of channel is acquired without crosstalk from 817.5–875.5 nm band.

The crosstalk is corrected and the blockage is removed by exciting the fluorophores in a round-robin manner and synchronically trigger cameras for individual image acquisition (Fig. 2.7-(a8)). The effect of crosstalk on the individual images acquired using continuous (Fig. 2.7-(a7)) and round-robin (Fig. 2.7-(a8)) methods is quantified by image quality assessment using structural similarity index measure (SSIM) metric [135]. Single-band fluorescence images of micro-beads (500–540 nm band), HeLa cell spheroid (592.5–667.5 nm band), and microfluidic channel (817.5–875.5 nm band) are used as references for the measurements (Fig. 2.7-(a1)-(a3)). SSIM values for the individual images of beads (Fig. 2.7-(f1)) and spheroid (Fig. 2.7-(f2)) acquired using the continuous method are computed as 0.24 due to the crosstalk and the blockage, respectively. Individual images of the channel are acquired using both continuous and round-robin methods with the SSIM value of about 0.91 (Fig. 2.7-f(3) and g(3)). Since indocyanine green is not able to be excited with 470 nm and 565 nm LEDs and the emission filter (ET845/55m, Chroma, USA) blocks the fluorescent photons emitted from fluorescein and CMTPIX (Fig. 2.1). We compute that the individual images are acquired using the round-robin method with the SSIM values of above 0.90, which enables spectral unmixing of micro-beads, HeLa cell spheroid, and microfluidic channel for dynamic real-time imaging (Fig. 2.7-(g)).

2.3.3 Exposure Time Analysis

Exposure time (τ), defined as the amount of time that a photodetector is subjected to the light for image formation, is the key factor for the maximum frame acquisition rate. For simultaneous multicolor imaging, the maximum frame acquisition rate equals $1/(\tau)$ [88, 118, 121]. Since a multicolor image is formed by the sequential acquisition of emitted fluorescence light from three different spectrum bands using the round-robin method, the maximum frame rate is computed as $1/(3\tau)$. To determine the maximum achievable frame rate, individual fluorescence images with the size of 1280×1024 pixels are captured with a 5 fps increment starting from 5 fps to 60 fps. The multicolor images at varying exposure

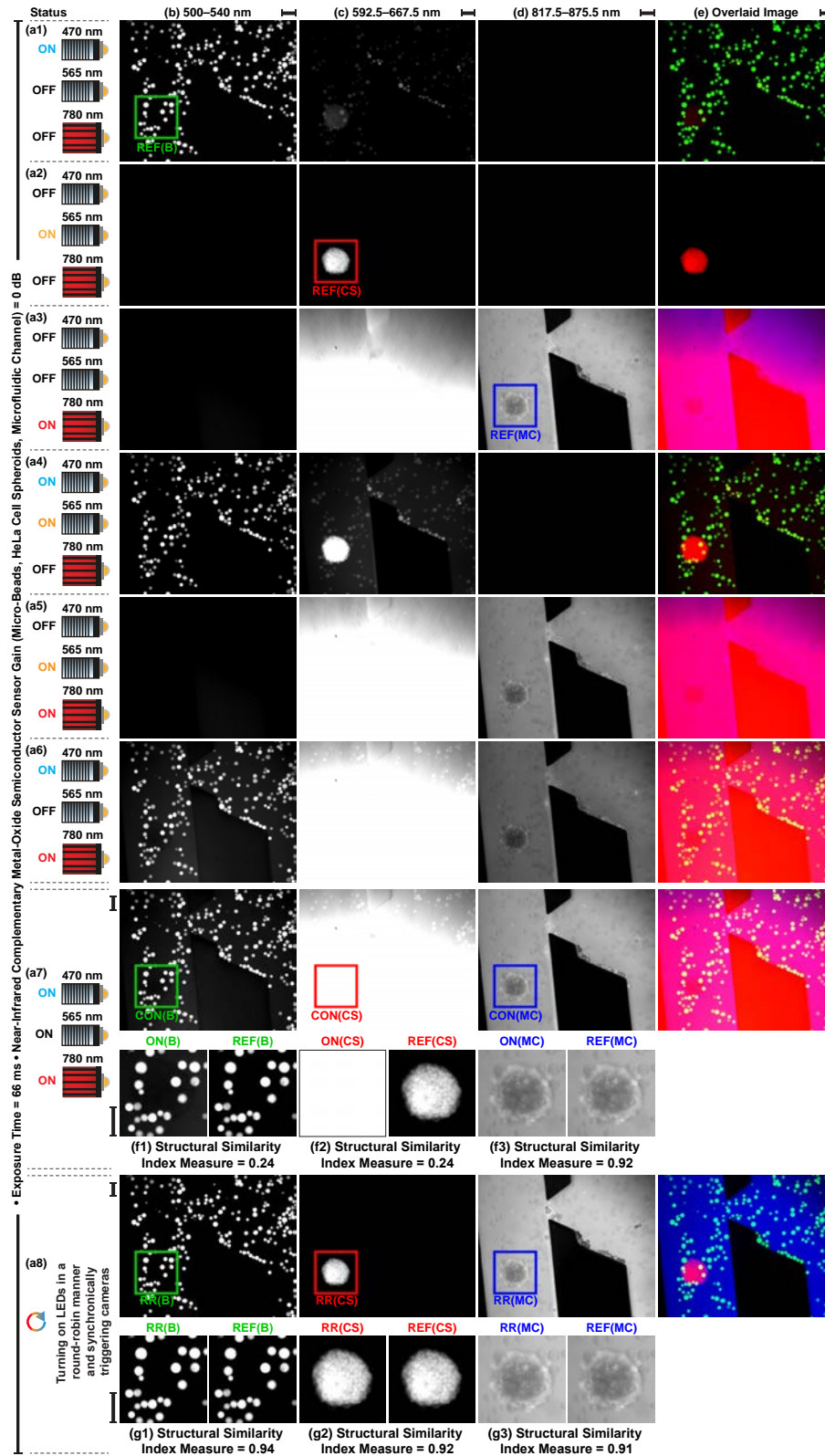


Figure 2.7: Crosstalk analysis. (a) Status of light-emitting diodes. (b)-(d) Acquired fluorescence images from 500–540 nm, 592.5–667.5 nm, and 817.5–875.5 nm spectrum bands, respectively. (e) Formed image by overlapping acquired images. (f) and (g) Quantitative crosstalk analysis by computing structural similarity measure index between reference images (REF) and images acquired using continuous (CON) and round-robin (RR) methods, respectively. Scale bar: 100 μm .

times are shown in Fig. 2.8-(a). To reveal details of beads, spheroid, and pillar inside the channel, magnified views of the ROI defined on the multicolor image plane are shown in Fig. 2.8-(b). Both camera gain and LED power versus exposure time are plotted in Fig. 2.8-(c). Spectrally-different fluorescence images of micro-beads, HeLa cell spheroid, and microfluidic channel are acquired with 1 dB gains until 33 ms exposure time, which enables frame acquisition up to 10 fps without the noise associated with amplification. For enhancing fluorescence signal intensity, gains are increased to 5.3 dB when the exposure time is 33 ms for channel, 13.2 ms for beads, and 9.4 ms for spheroid, respectively.

To study the effect of exposure time on the multicolor fluorescence images, horizontal lines are defined on the beads, spheroid, and channel for contrast characterization [136]. Pixel intensities on the lines versus exposure time are plotted in Fig. 2.8-(d). When the exposure time is decreased from 66.0 ms to 5.5 ms for multicolor image acquisition with 60 fps, maximum pixel intensities of beads and channel drops by 13.3% and 25.6% at the full excitation power, respectively. No change is measured for the maximum pixel intensity of the spheroid since the increase in both LED power and camera gain bypasses the drop regarding exposure time. Peak signal-to-noise ratio (PSNR) and structural similarity index measure (SSIM) are used to quantify the multicolor image quality [135]. For both measurements, ROI acquired with 66.0 ms exposure time is used as the reference and computed values versus exposure time are plotted in Fig. 2.8-(e). We compute that decreasing exposure time from 33 ms to 5.5 ms reduces PSNR and SSIM by 27.6% and 12.9%, respectively. Our imaging experiments show that multicolor fluorescence images are able to be acquired at full sensor resolution up to 60 fps, which equals to maximum frame acquisition rate of the CMOS camera used for microfluidic channel imaging (DCC3240N, Thorlabs, USA).

2.3.4 Uptake of Indocyanine Green by HeLa Cell Spheroids

Indocyanine green is a near-infrared fluorescent dye and one of its prominent application domains is cancer cells labeling [137, 138]. The microfluidic channels contain indocyanine green in the culture medium, which is a suitable environment for fluorescence labeling of cells. HeLa cell spheroids stained with CMTPX uptake indocyanine green after placed in the channels and becomes visible in the acquired individual fluorescence images of the microfluidic channel (Fig. 2.6). Time-lapse imaging for dynamic uptake of indocyanine green in spheroids is shown in Fig. 2.9-(a) and (b). The effect of staining a spheroid with CMTPX and indocyanine green uptake on the formed multicolor fluorescence images are shown in Fig. 2.9-(c). CMTPX and indocyanine green enable dual-color fluorescence microscopy for the spheroid by image acquisition from 592.5–667.5 nm and 817.5–875.5 nm spectrum bands. Therefore, four-color fluorescence microscopy is performed utilizing fluorescein, CMTPX, and indocyanine green for dynamic imaging of micro-agents and 3D cancer cell spheroids in a microfluidic setup.

We observe that heating of the illuminated area results in a temperature gradient, which creates a flow inside the channel. To image the flow, a microfluidic channel contains 250 $\mu\text{g/ml}$ indocyanine green in the culture medium is continuously excited. The acquired time-lapse image sequence is shown in Fig. 2.9-(d). For the first 81 minutes, indocyanine green bleaches so pixel intensities drop. The flow starts to bring the non-bleached fluorescent molecules area to the imaging area at 81-minutes, and pixel intensities start to increase (Fig. 2.9-(d2)). The effect of the flow on a spheroid is shown in Fig. 2.9-(b). Indocyanine green uptake is saturated at 30-minute and then the fluorescence signal decreases until 95-minutes as a result of photobleaching. The spheroid starts to uptake the non-bleached

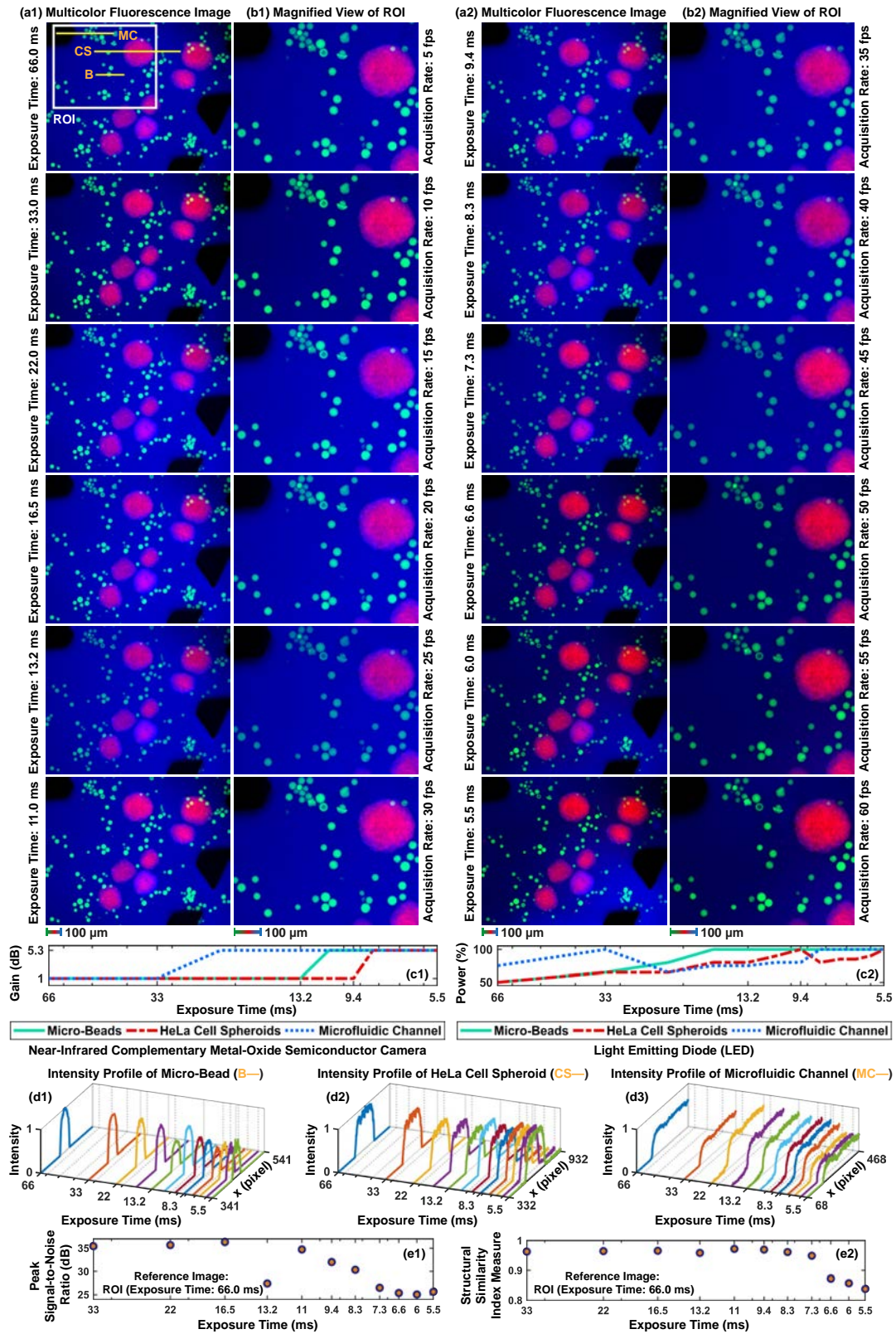


Figure 2.8: (a) Multicolor fluorescence images at varying exposure times. (b) Magnified view of the region of interest (ROI). (c1) and (c2) Camera gain and LED power during the image acquisition, respectively. (d1)-(d3) Intensity profiles of the lines defined on the beads, spheroid, and channel, respectively. (e1) and (e2) Measured peak signal-to-noise ratio and structural similarity measure index between multicolor images in (b) and the reference (multicolor image with 66.0 ms exposure time), respectively.

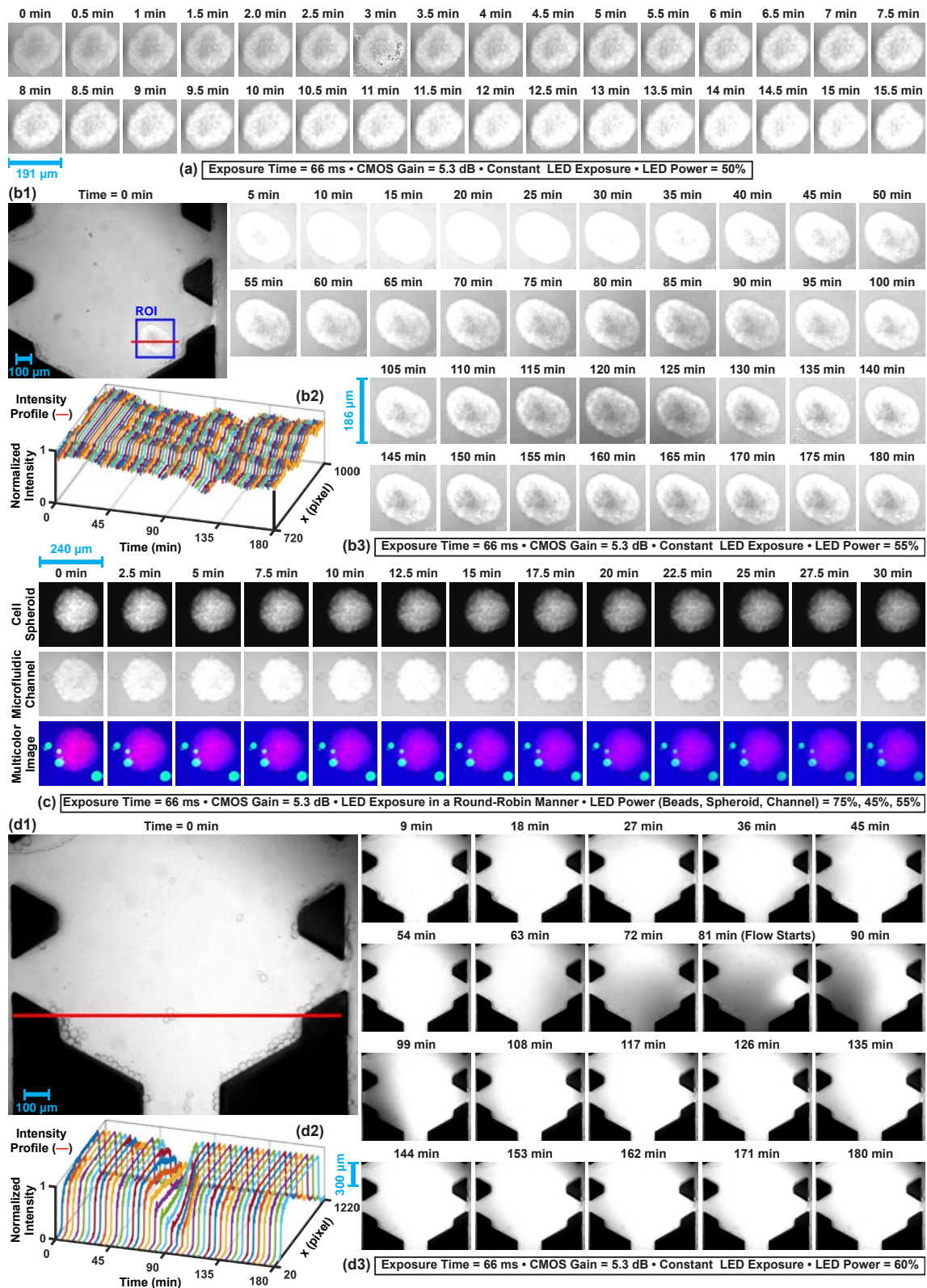


Figure 2.9: (a)-(b) Time-lapse imaging for dynamic uptake of indocyanine green in a HeLa cell spheroid. (c) Effect of staining a spheroid using both CellTracker Red CMTPIX and indocyanine green on the multicolor fluorescence images. (d) Time-lapse imaging of the flow created by temperature gradient. (b2) and (d2) Expressing effect of the flow on the fluorescence signal by plotting normalized pixel intensities over time on the defined red-lines in (b1) and (d1), respectively.

indocyanine green molecules brought by the flow at 95-minutes (Fig. 2.9-(b2)). Our imaging experiments show that the flow created by temperature gradient prolongs the imaging time of both microfluidic channels and HeLa cell spheroids at 817.5–875.5 nm band by recovering the fluorescence signals [139].

2.3.5 Photobleaching Resistance

When a fluorophore starts to be excited, emission light intensity decays over time. After a decay time, the emission of fluorescence photons is not possible due to irreversible photochemical alterations in the fluorophore molecules. This phenomenon is called photobleaching [140]. The photobleaching resistance of fluorescein, CMTPX, and indocyanine green is studied using time-lapse multicolor fluorescence microscopy of micro-beads, HeLa cell spheroids, and microfluidic channels, respectively. Multicolor fluorescence images are acquired under constant excitation power for 60 minutes with 66.0 ms, 33.0, 22.0, and 16.5 ms exposure times (Fig. 2.10-(a)). To express the effect of the photobleaching mechanism on the emitted fluorescence intensity, the normalized average intensity profiles of beads, spheroids, and channels over time are plotted in Fig. 2.10-(b). When the exposure time is 16.5 ms, we compute that the normalized average intensity of beads, spheroids, and channels decreases to 0.8 at 1.1 minutes, 29.5 minutes, and 60.0 minutes, respectively. Compared to fluorescein and indocyanine green, CMTPX exhibits a greater photobleaching resistance. Although beads and channels are not fully visible in the fluorescence images due to photobleaching, the spheroids are imaged with the normalized average intensity of more than 0.8 (Fig. 2.10-(a3) and (a4)). We also observe that the flow created by temperature gradient and indocyanine green uptake by spheroids create a fluctuation in the intensity profile of the microfluidic channel (Fig. 2.9 and Fig. 2.10-(b3)). The flow also fully recovers fluorescence imaging of microfluidic channel when the exposure time is 66.0 ms. Fluorescence recovery is not observed when the exposure time is lower than 66.0 ms. Imaging with higher exposure times increases the rate of recovery owing to a decrease in the photodamage on the fluorescence molecules brought by the flow [139].

2.3.6 Photodamage Analysis

Performing excitation in a round-robin manner inherently prolongs the fluorescence imaging time by reducing the photodamage on the fluorophores. To monitor the effect of photodamage on fluorescein, CMTPX, and indocyanine green, time-lapse fluorescence microscopy with continuous and round-robin excitation methods is performed for micro-beads, HeLa cell spheroids, and microfluidic channel, respectively (Fig. 2.11). Photobleaching curves are obtained by computing normalized average intensity over time for photodamage characterization (Fig. 2.11-(a2)-(c2)). Our experiments show that the round-robin excitation method increases the fluorescence half-lives of beads, spheroids, and channels 2.0-fold, 1.6-fold, and 1.5-fold, respectively. Approximately 0.5-fold drop in the half-lives of spheroid and channel is measured since CMTPX and indocyanine green are also excited by LEDs with the center wavelengths of 470 nm and 565 nm as a result of spectral overlap, respectively (Fig. 2.7). We also observe that the flow created by temperature gradient does not occur with the continuous excitation due to relatively high excitation power [139]. On the other hand, round-robin excitation enables flow generation and fluorescence signal recovery of the channel by decreasing the photodamage on the indocyanine green.

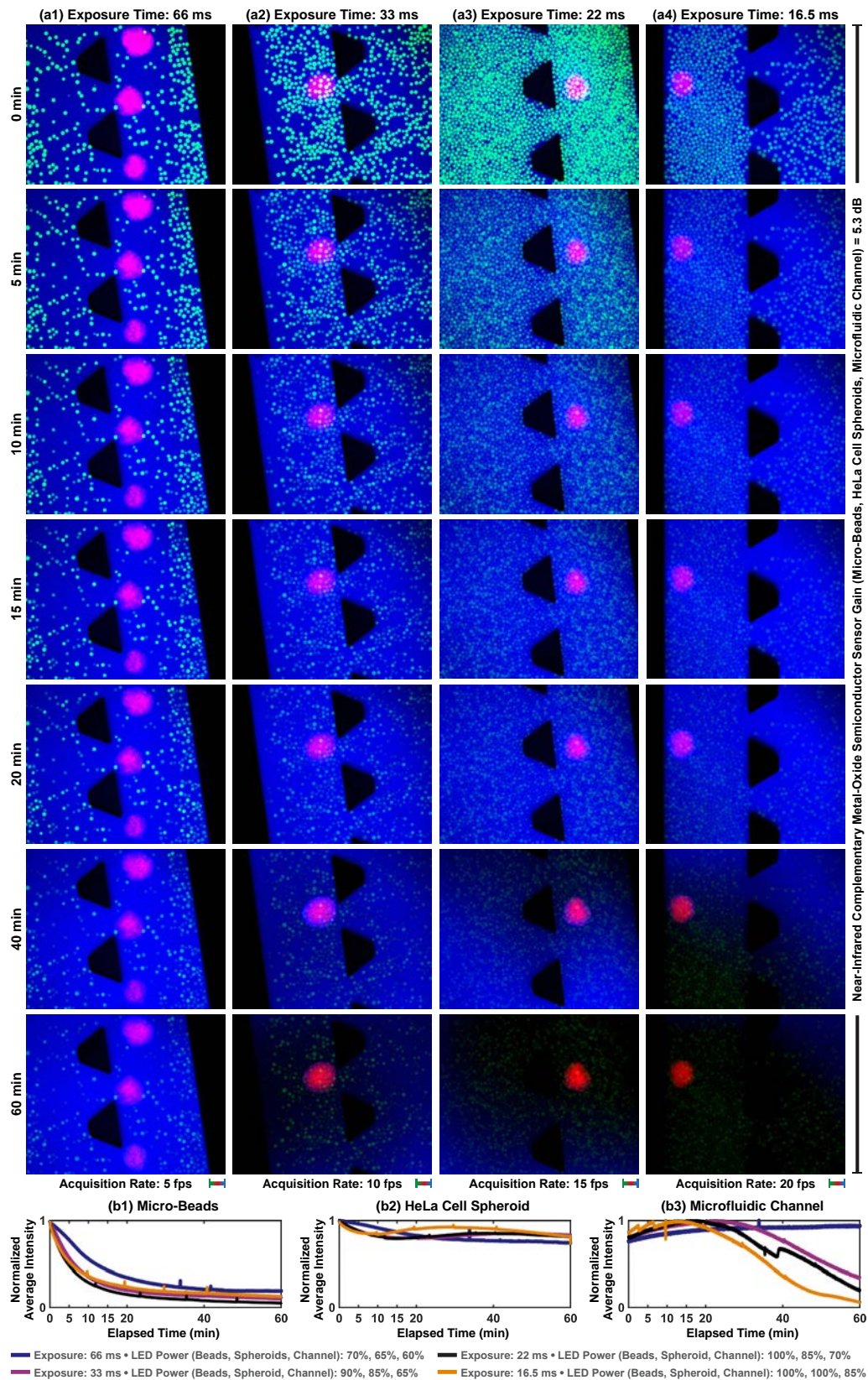


Figure 2.10: The effect of photobleaching mechanism on multicolor fluorescence microscopy under constant excitation power. (a) Time-lapse multicolor fluorescence images at varying exposure times. (b1)-(b3) Normalized average intensity profiles of micro-beads, HeLa cell spheroids, and microfluidic channel, respectively. Scale bar: $100 \mu\text{m}$.

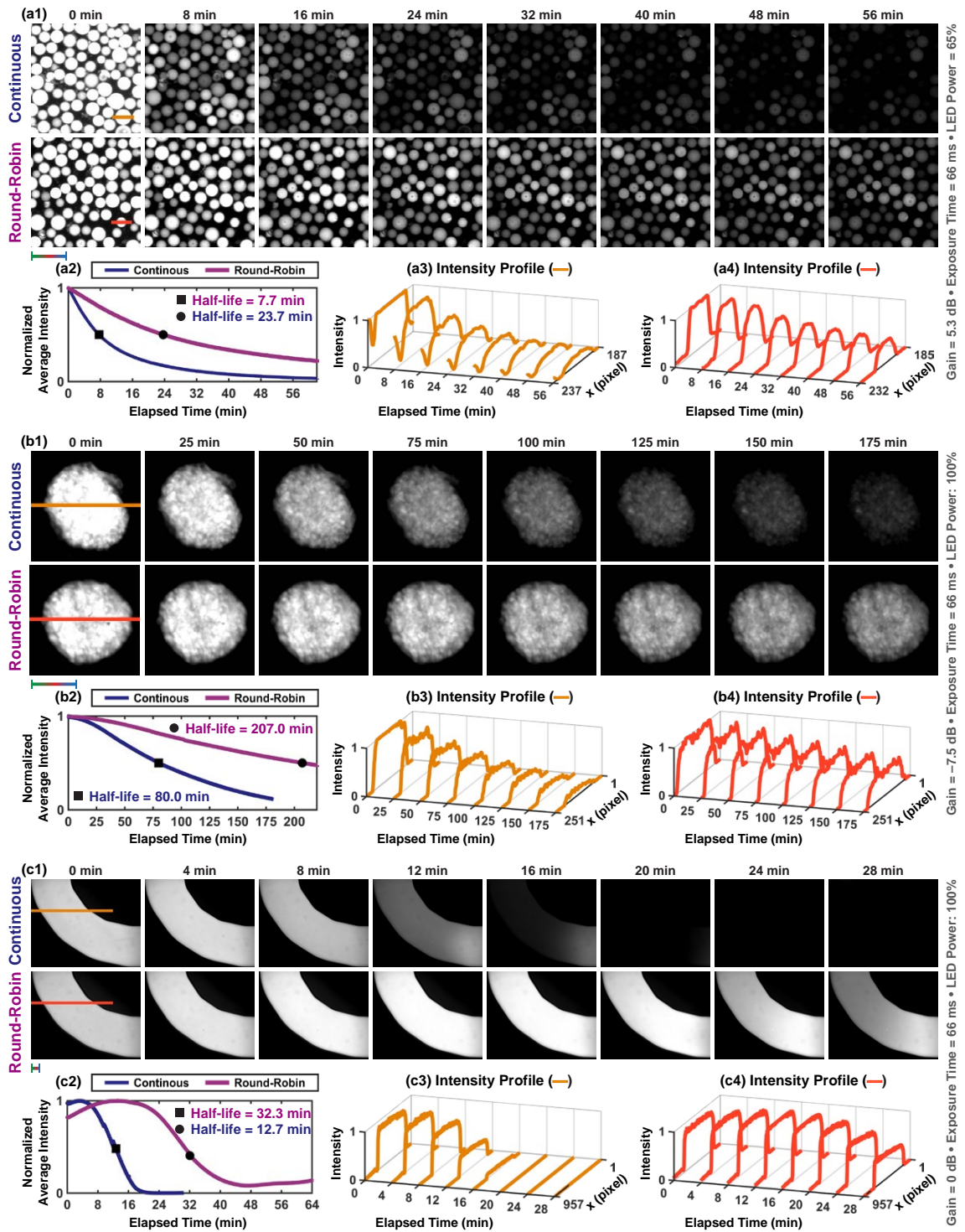


Figure 2.11: The effect of continuous and round-robin excitation methods on photodamage mechanism. (a1)-(c1) Acquired time-lapse fluorescence images of micro-beads, HeLa cell spheroids, and microfluidic channel, respectively. (a2)-(c2) Photobleaching curves by computing normalized average pixel intensity in each image. (a3)-(a4) – (c3)-(c4) Intensity profiles of the lines defined on beads, spheroids, and channel, respectively. Scale bar: 100 μm .

2.3.7 Real-time Multicolor Fluorescence Microscopy

HeLa cell spheroids and polystyrene micro-beads are negatively and positively charged, respectively. Utilizing electrostatic forces, beads are able to be attached to the surface of

spheroids without functionalization, which a self-assembly method used for biohybrid micro-agent fabrication [3]. As a representative application, the attachment of micro-beads to a HeLa cell spheroid in a microfluidic channel is imaged using multicolor fluorescence microscopy. For the imaging experiment, the channel is fixed on the sample holder attached to a translation stage (PT3/M, Thorlabs, USA). The holder is manually and randomly moved in horizontal and vertical directions until no further bead capture by the spheroid takes place due to the neutralization (Fig. 2.12). Individual fluorescence images of the beads, spheroid, and channel are acquired with 22 ms exposure time and 5.3 dB gain at 15 fps and overlaid to form multicolor images. The motion of beads, spheroid, and channel between consecutive individual fluorescence images are analyzed using the Lukas-Kanade optical flow technique [141]. The analyzed motion at 63 seconds and 518 seconds is represented as three independent vector fields and overlaid onto the fluorescence images (Fig. 2.12-(c)). Our experiment shows that individual motion of micro-agents, 3D cancer cell spheroids, and microfluidic setup is able to be imaged in real-time by spectrally different image acquisition.

2.4 Conclusions

This study presents multicolor fluorescence microscopy to visualize polymeric drug carriers, organic bodies, as well as their surroundings. Polystyrene micro-beads and HeLa cell spheroids are employed as an example of polymeric drug carriers and organic bodies, respectively. We develop a simplified 3D tumor model to validate spectrally-different image acquisition of beads, spheroids, and channel, using multicolor fluorescence microscopy. A multicolor widefield fluorescence microscope is developed as a tool to acquire images from three different spectrum bands using a common optical path. To correct the spectral crosstalk, fluorophores with fairly well-separated emission spectra are excited in a round-robin manner and the emitted light is synchronously collected. In this study, we experimentally validate that multicolor fluorescence microscopy enables crosstalk-free visualization of beads, spheroids, and channel by individual image acquisition from different spectrum bands with a minimum exposure time of 5.5 ms. Our measurements show that multicolor fluorescence microscopy using round-robin method provide clear visualization by containing direct segmentation of beads, spheroids, and channel. We utilize multicolor fluorescence microscopy for real-time visualization of the interaction between drug carriers and cancer cells in a microfluidic channel.

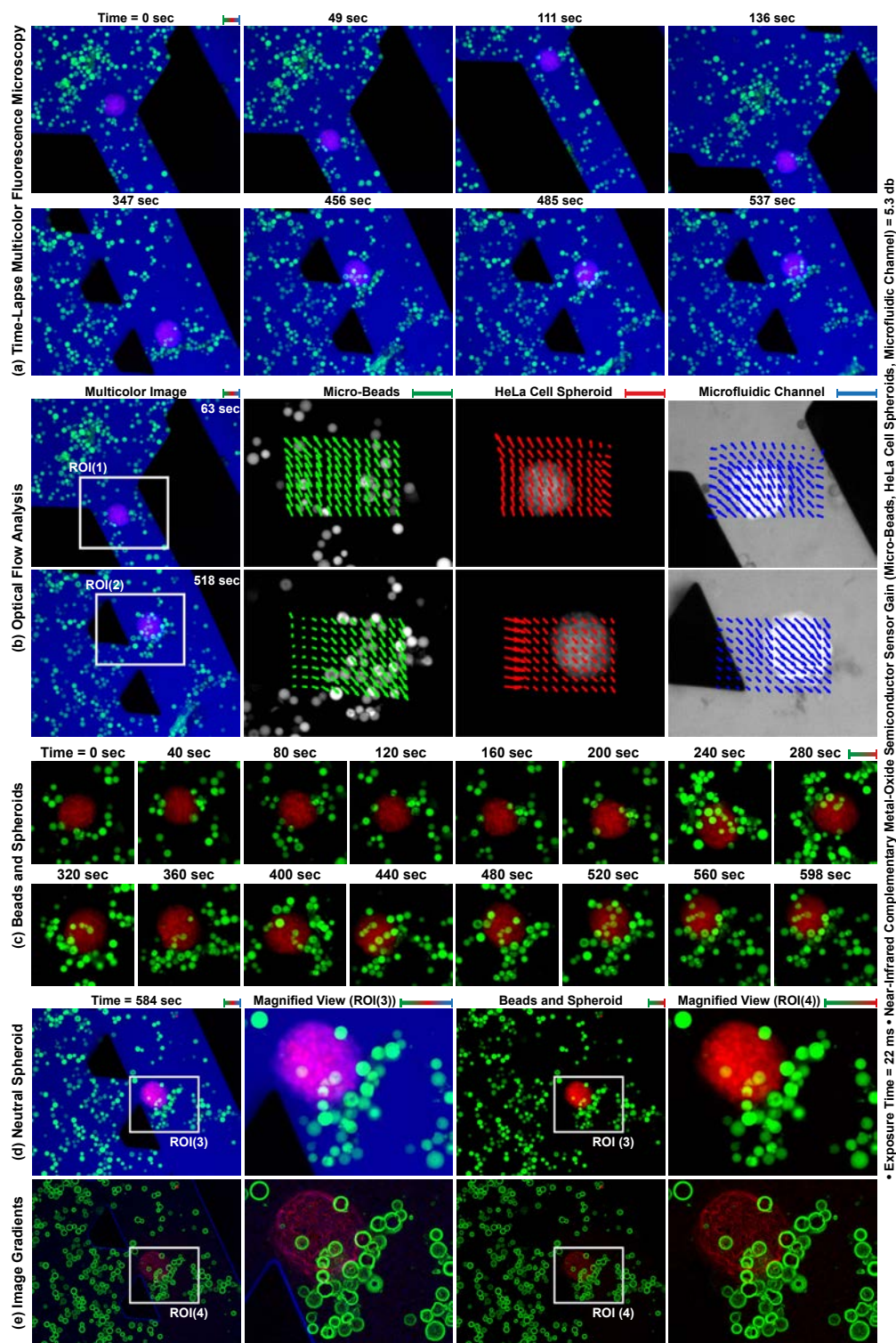


Figure 2.12: Multicolor fluorescence microscopy for the attachment of polystyrene micro-beads to a HeLa cell spheroid surface utilizing electrostatic forces. (a) Time-lapse multicolor fluorescence image sequence acquired at 15 frames per second. (b) The analyzed motion using Lukas-Kanade optical flow in ROI(1) and ROI(2) at 63 seconds and 518 seconds is represented as vector fields and overlaid on the fluorescence images. The spectrally different motion information of beads, spheroid, and channel is represented using green, red, and blue arrows, respectively. (c) Time-lapse fluorescence image sequence of beads and spheroid. (d) Neutral HeLa cell spheroid covered with micro-beads. (e) Gradients of the images in (d) for contrast visualization. Scale bar: $100 \mu\text{m}$.

3. Development of a Coil Driver for Magnetic Manipulation Systems

Note: The following content is an adapted version of the paper "Development of a coil driver for magnetic manipulation systems" by **M. Kaya**, U. Sakthivel, I. S. M. Khalil, and S. Misra published in "*IEEE Magnetics Letters*", 10(1), pages 1–5, December 2019.

Abstract

Pulse width modulation (PWM) is the most commonly used technique to drive electromagnetic coils in magnetic manipulation systems. Relatively low PWM frequencies generate high magnitude current ripple and magnetic field fluctuation. In this study, coils are powered by a driver at PWM frequencies close to their self-resonant frequencies to generate high-frequency magnetic fields and minimize current ripple and magnetic field fluctuation. In order to protect the driver against the penetration of stray electromagnetic and magnetic fields, a multi-layer shielding enclosure is employed. The coil driver is used to study the effect of varying PWM frequencies on current, magnetic field, and ohmic loss using Helmholtz, air and iron core coils. The current ripple magnitude is significantly minimized when the coils are driven at PWM frequencies close to their self-resonant frequencies. This results in reduction of magnetic field fluctuation and provides more accurate measurement of magnetic field magnitude. Our experiments show that increasing the PWM frequency from 100 Hz to 25 kHz decreases the current ripple and magnetic fluctuation by two orders of magnitude, and a negligible effect on the ohmic loss.

3.1 Introduction

The field of magnetic manipulation has been witnessing a substantial progress in recent years. Its most prominent application domains are minimally invasive surgery, drug delivery, assembly of micro-scale objects [5, 100, 142]. Electromagnetic coils produce magnetic fields by inducing current through the loops. These coils are used in magnetic manipulation systems by adjusting the amplitude of the current [73]. Pulse width modulation (PWM) is the most frequently used technique to control the current, since it provides high efficiency, low power loss, and robustness to noise [143]. However, PWM produces high magnitude current ripples at relatively low frequencies. As a result of the current ripples, magnetic field fluctuation occurs. These fluctuations limit the operating time of the coils and decrease the predictability of the field, which is an essential component for the manipulation. Although coil configuration has been extensively studied for magnetic manipulation systems, there is a lack in the literature regarding development of coil drivers for precise magnetic manipulation [144–148]. The relationship between PWM frequency and magnetic field fluctuation has not been considered. The majority of drivers used in the literature are designed for low-frequency drive applications. PWM resolution in such drivers also changes with the PWM frequency, which leads to relatively low motion resolution for the manipulation.

In this study, a coil driver is developed to minimize the magnetic field fluctuations and improve the motion resolution of magnetic manipulation systems. A multi-layer shielding enclosure is specifically machined to protect the driver by blocking stray magnetic and electromagnetic fields. Unlike the drivers used in magnetic manipulation systems, coils are driven at higher PWM frequencies which are close to their self-resonant frequencies using the developed coil driver [149–153]. This method minimizes magnetic field fluctuation by reducing current ripple magnitude, which provides more predictable field. In addition, the developed driver is essential for the applications where the high-frequency magnetic field generation is required like hyperthermia-based drug delivery using magnetic micro-agents [154]. Magnetic manipulation and drug release can be performed using the developed driver without an external magnetic induction unit, which decreases the complexity of the system. The driver is experimentally validated using Helmholtz, air and iron core coils. At varying PWM frequencies, current through coil terminals, magnetic field magnitude, and ohmic loss are monitored (Fig. 3.1). Finite element analysis is also performed to simulate the effect of varying PWM frequencies on the current, magnetic field, ohmic loss, and magnetic force. In the following section, coil driver architecture is explained. The experimental setup and our results are presented in Section 3.3.

3.2 Coil Driver

3.2.1 Driver Architecture

The lumped element model of a coil consists of an inductor (L) in series with a resistor (R) and a capacitor connected in parallel with L and R [151]. When the voltage is applied to the coil, current reaches its steady-state value at five times coil time constant (5τ). τ is the required time for a current to reach its 63.2% steady-state value and calculated as L/R . If the PWM signal with a frequency of $1/(5\tau)$ is applied to coils, sawtooth current waveform (also known as current ripple) is observed. The peak-to-peak amplitude of the current ripple minimizes when PWM frequency is on the order of $1/(5\tau)$. The frequency can be increased up to coil self-resonant frequency ($1/(2\pi\sqrt{LC})$), since exceeding self-resonant frequency results in capacitive behavior of the coil. This can also be observed from frequency (f)

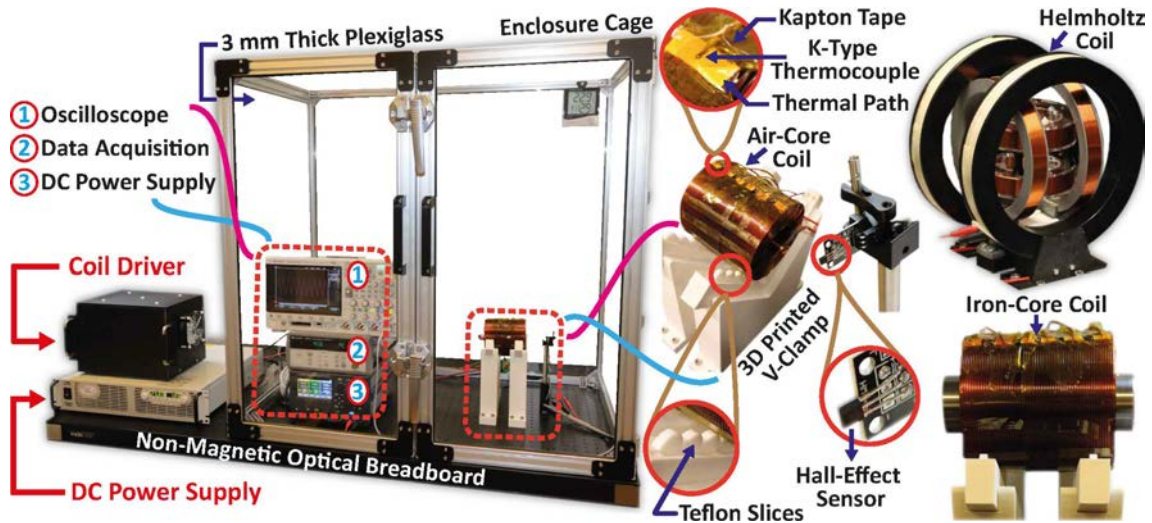


Figure 3.1: Overview of the experimental setup used for monitoring effect of varying pulse width modulation frequencies on the current through coil terminals, magnetic field, and ohmic loss using the coil driver.

dependent impedance analysis of the coil ($(R + j2\pi fL)/(j2\pi fCR - (2\pi f)^2LC + 1)$). In order to drive the coils at PWM frequencies that are close to their self-resonant frequencies, a coil driver is developed.

The developed coil driver architecture is illustrated in Fig. 3.2-(a). The driver circuit is capable of generating a 14-bit PWM signal and amplifying it up to 1 MHz. PWM signal with 14-bit resolution is generated by a comparator using cosine wave with reference voltage. PWM carrier frequency and duty cycle are adjusted by changing frequency of cosine wave and level of reference voltage, respectively. Cosine wave at desired frequency and reference voltage are generated using a 14-bit direct digital synthesizer (DDS) and a 16-bit digital-to-analog converter (DAC), respectively. Outputs of both DDS and DAC are currents that provide high slew rate and robustness to noise. Transimpedance amplifier is used to convert the output of DDS and DAC currents to voltage. In order to use a single channel PWM signal for bidirectional coil drive, a combination of logic gates is configured. Generated PWM signal has a constant resolution of up to 1 MHz, unlike the conventional drivers. It is amplified using a switch-mode full-bridge amplifier consists of four metal-oxide-semiconductor field-effect transistors (MOSFETs) driven by two gate drivers. In order to get precise coil drive, fluctuation in power line during the switching is filtered using a passive power rail filter with a cutoff frequency of 110 Hz.

Accurate sensing of current through coil terminals is one of the vital elements of any designed driver for a precise magnetic manipulation, since current data is used to fed back to the controllers. For current sensing, a four-wire Kelvin resistor is connected between the full-bridge amplifier and ground. The output of Kelvin resistor is connected to differential amplifier. Offset measurement circuit is built to cancel the inherent offset voltage of the differential amplifier. In order to measure offset voltage of the amplifier, a second differential amplifier circuit is built and its outputs are connected to the ground [155]. Since the voltage difference between input terminals is zero, output signal equals offset voltage of the amplifier. The signal that is obtained using this circuit is subtracted from the differential input signal for relatively accurate measurements. In addition, a temperature sensor is placed on the Kelvin resistor to compensate resistor change related to temperature. Noise characterization of the driver is done by supply and coil voltage

measurement circuits. 16-bit analog-to-digital converter (ADC) is used to digitize outputs of current and voltage measurement circuits. Anti-aliasing filters are placed between the measurement circuit outputs and ADC to filter high-frequency noise. Utilizing the current and voltage measurement circuits, impedance curve of the coils are obtained. This property allows characterizing different type of coils without using a specific electronic equipment. A single board computer (SBC) establishes communication with both ADC and PWM generator via serial peripheral interface (SPI). The driver is cooled by two SBC controlled fans placed as push and pull configuration [156]. MOSFET cooling is additionally maintained by attached heat sinks. Temperature sensors placed on the heat sink surfaces provide feedback to adjust fan speed.

3.2.2 Magnetic and Electromagnetic Shielding

Magnetic manipulation systems inherently generate stray magnetic and electromagnetic fields. These fields might damage the driver electronics, since they significantly degrade the accuracy of both measurement and control signals. Therefore, a proper shielding plays an important role in precise coil drive and magnetic manipulation. In order to prevent possible interference, a shielding enclosure is machined using both 1 mm thickness steel (CR4, cold rolled) and Mu-metal. Although steel has high relative permeability of 100 to 5,000 and generates a low-resistance path for both electromagnetic and magnetic fields, it might not be enough to attenuate the magnitude of stray fields [157]. On the other hand, Mu-metal which is a nickel-iron alloy provides extremely high relative permeability of 80,000 to 100,000 and stronger shielding [158]. When steel and Mu-metal are used together, interference is attenuated by steel as pre-processing step layer then removed by Mu-metal. Path resistance is decreased by increasing the number of steel sheets, known as multi-layer shielding [159], [160]. Therefore, three individual steel sheets are placed in parallel and isolated using two 3D printed dividers. Inside of these steel layers, a Mu-metal enclosure is placed to protect sensitive driver parts. Honeycomb structures are placed onto the side surfaces of the steel and the Mu-metal enclosures to circulate air with fans. Schematic of the shielding enclosure is illustrated in Fig. 3.2-(b).

3.3 Experiments

3.3.1 Finite Element Results

Finite element analysis using ANSYS Electronics (Swanson Analysis Systems Inc., USA) was performed to simulate magnetic field fluctuation, ohmic loss, and magnetic force. For simulations, air, vacoflux, and iron core coils were used to visualize both fluctuation and ohmic loss at varying PWM frequencies. Further, magnetic field fluctuation in and around Helmholtz coil was simulated to monitor coupling between the coil pair. Dimensions, equivalent circuits, and computed impedance and phase curves of both air core and Helmholtz coils are given in Fig. 3.3-(a). PWM at varying frequencies with 55 V amplitude and 50% duty cycle was applied to the coils for extreme boundary conditions.

Simulations were run with 15 kHz, 5 kHz, 1 kHz PWM frequencies for air, vacoflux, and iron core coils, respectively. Low frequency response of the coils was simulated at 100 Hz. Helmholtz coil was simulated at 1 kHz, 10 kHz, and 100 kHz. Simulations show that substantial magnetic field fluctuation occurs at low frequencies, whereas fluctuation is significantly reduced at high frequencies (Fig. 3.3-(a)). Substantially improved coupling between Helmholtz pair and a more uniform magnetic field were observed compared to the low PWM frequency. Further, the increase in frequency does not highly affect ohmic loss.

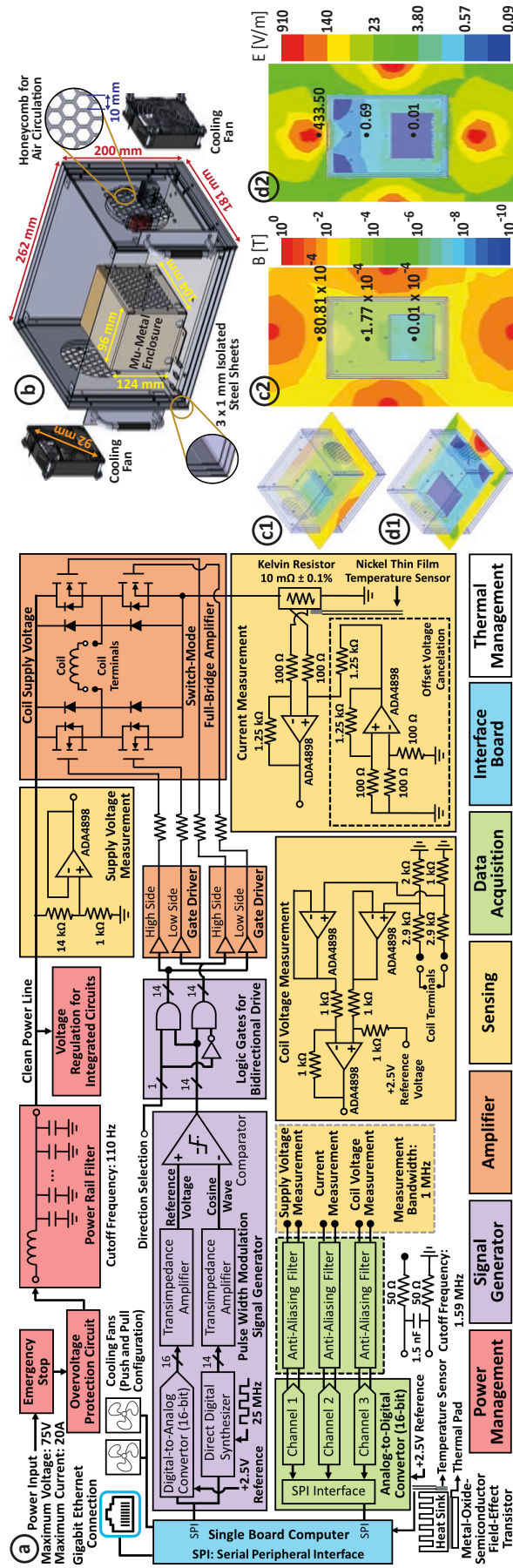


Figure 3.2: Schematic representation of the coil driver. (a) Architecture of the driver circuit. (b) Computer-aided design model of the machined multi-layer shielding enclosure. (c), (d) Finite element results for the attenuation efficiency of the electromagnetic and magnetic shielding enclosure. Magnetic and electromagnetic field distributions in and around the shielding enclosure are shown (c), (d) and (c), (d), respectively.

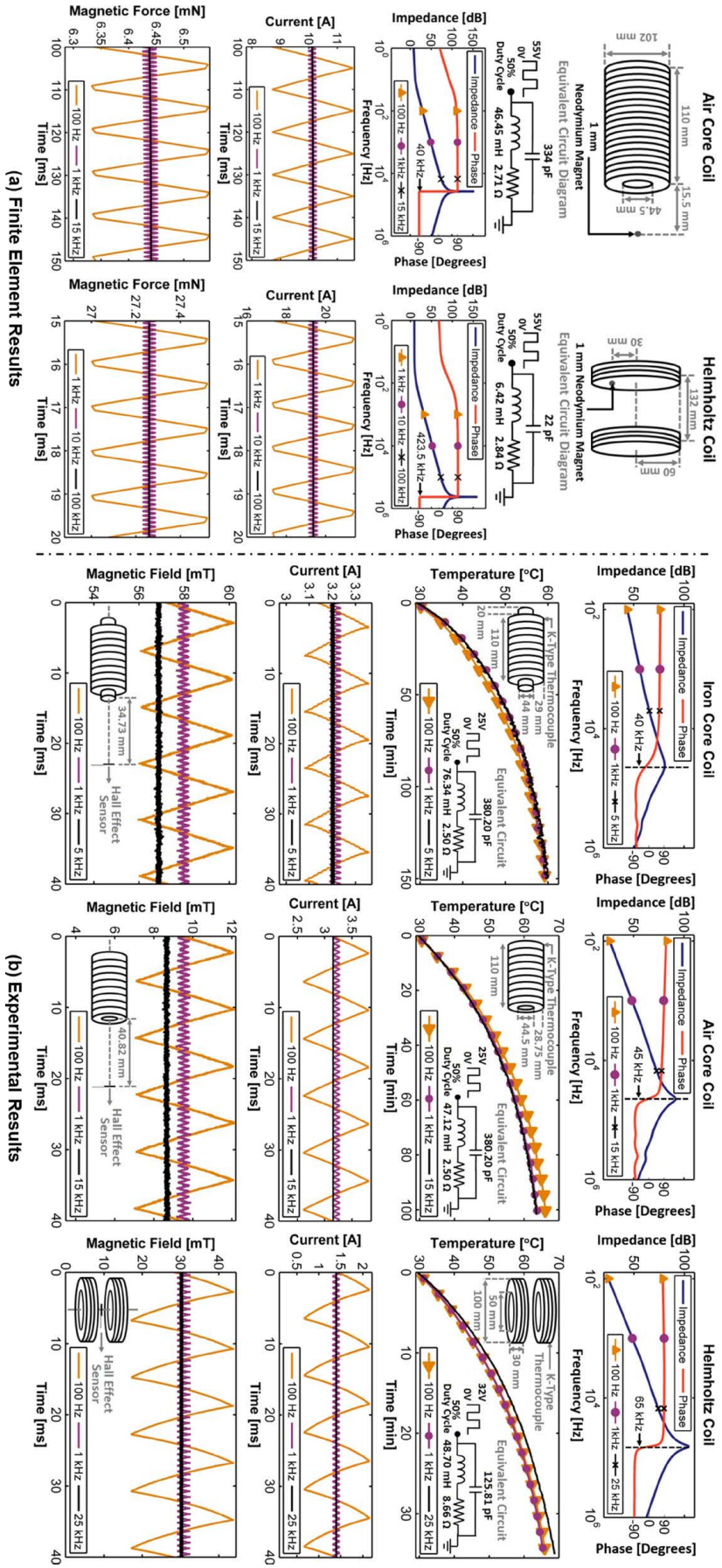


Figure 3.3: Finite element and experimental results of magnetic force acting on a magnet for iron core, air core, and Helmholtz coils. a) Finite element results of magnetic force acting on a magnet are shown for iron core, air core, and Helmholtz coils. b) Experimental results of coil drive are shown for iron core, air core, and Helmholtz coils.

The effect of PWM frequency on magnetic force ripple acting on 1 mm spherical magnet using air core and Helmholtz coils were simulated. The magnet locations are depicted in Fig. 3.3-(a). In order to monitor relationship between PWM frequency and magnetic force, air core coil was simulated at 100 Hz, 1 kHz, and 15 kHz. Force ripple magnitudes at these frequencies were computed as 0.22 mN, 0.14 mN, and 0.01 mN, respectively. For Helmholtz coil, force magnitude ripples at 1 kHz, 10 kHz, and 100 kHz were computed as 0.52 mN, 0.19 mN, and 0.02 mN, respectively. In both of these simulations, the force ripple magnitude was reduced by nearly 96% when PWM frequency was changed from lowest to highest frequency. Current and magnetic force waveforms are plotted in Fig. 3.3-(a).

Electromagnetic and magnetic field attenuation efficiency of the shielding enclosure was computed using four air core coils and four dipole antennas. Coils and antennas were arranged to generate 8 mT magnetic field and 430 V/m electric field on the side surfaces of the enclosure, respectively. Magnetic and electromagnetic field distributions are shown in Fig. 3.2-(c) and (d). Multi-layer steel configuration attenuates magnetic and electromagnetic signal amplitudes by 97.82% and 99.99%, respectively (Fig. 3.2-(c) and (d)). Further, attenuated wave magnitudes by the steel is degraded by 99.99% inside Mu-metal. Results show that combination of steel and Mu-metal provides strong blockage against electromagnetic and magnetic contamination.

3.3.2 Experimental Setup

Helmholtz, air and iron core coils were used to test performance of the coil driver at varying PWM frequencies. A Hall-effect sensor (49E, YZPST, China) was used to monitor high-frequency fluctuation in the magnetic field. The sensor was supplied with a DC power supply (E36313A, Keysight, USA) and its analog output was acquired using an oscilloscope (DSOX3014T, Keysight, USA). In order to provide a disturbance free measurement environment, the experimental setup was mounted on a non-magnetic optical breadboard (PBG52514, ThorLabs, USA). Coil surface temperature was measured to observe ohmic losses using six K-type thermocouples (34307A, Keysight, USA). Temperature data was acquired using a data acquisition unit (34901A and 34972A, Keysight, USA) with a sampling rate of 1 Hz. In order to provide same air convection conditions during the experiments, an enclosure cage with a volume of $670 \times 920 \times 950 \text{ mm}^3$ was fabricated [161, 162]. The cage was specifically sealed to avoid any external air flow and keep the effect of coil temperature on the global temperature at minimum to accurately measure ohmic loss and eliminate disturbance inside enclosure cage. Air and iron core coils were placed onto a custom-made 3D printed V-clamp. Teflon slices were placed between the clamp and the coil to prevent temperature rise and heat conduction. During the experiments, the driver was supplied with a DC power supply (N8738A, Keysight, USA). The experimental setup is shown in Fig. 3.1.

3.3.3 Experimental Results

Impedance and phase curves were analyzed using a Hewlett Packard 4194A impedance/gain-phase analyzer to determine equivalent circuits and self-resonant frequencies of the coils. Frequency dependent impedance and phase plots, the equivalent circuits and dimensions of the coils are plotted in the first two rows of Fig. 3.3-(b). The self-resonance frequencies of iron core, air core, Helmholtz coils were measured as 40 kHz, 45 kHz, and 65 kHz, respectively. During the experiments, coil surface temperature, current through coil terminals, and fluctuation in magnetic field at a specified location were monitored at varying PWM

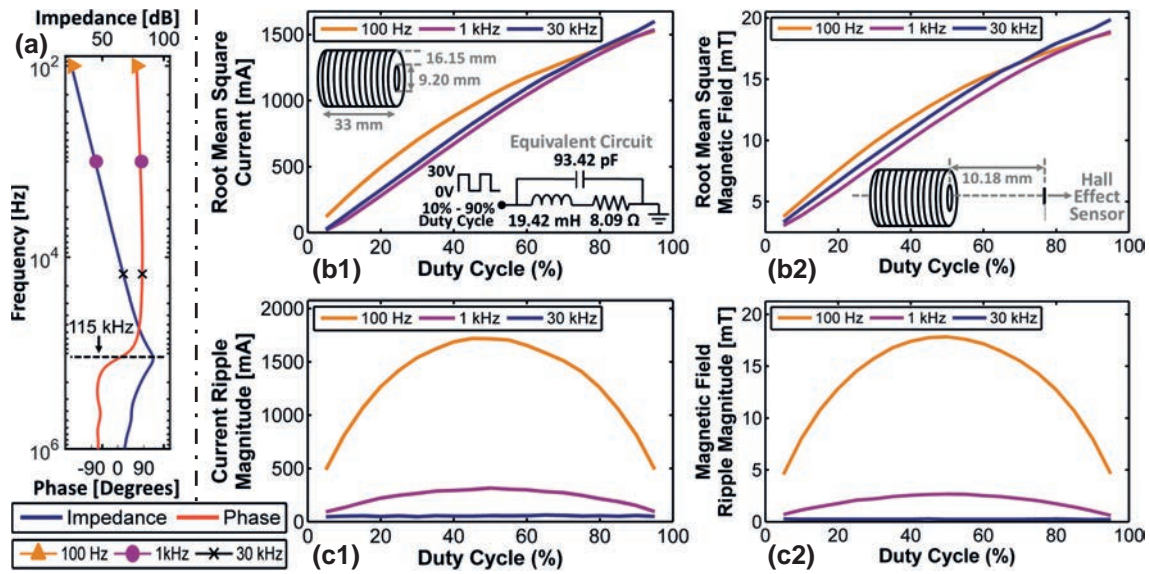


Figure 3.4: Experimental results of coil drive with varying duty cycles. (a) Impedance and phase curves of the air core coil used in the experiments. Root mean square current and magnetic field magnitudes versus current and magnetic field magnitudes versus duty cycle are shown in (b1) and (b2), respectively. Current and magnetic field ripple magnitudes versus duty cycle are shown in (c1) and (c2), respectively.

frequencies with 50% duty cycle. Experiments were carried out to monitor low and high frequency behavior of each coil configuration under constant PWM duty cycle and supply voltage. All of the coil configurations were driven at 100 Hz and 1 kHz to observe their low frequency behaviour. In order to monitor high-frequency behaviour of the coils, iron core, air core, Helmholtz coils were driven at 5 kHz, 15 kHz, and 25 kHz, respectively. These frequencies were chosen to keep magnitude of current ripple below 20 mA. PWM signal amplitude was set to 32 V and 25 V for Helmholtz, air core and iron core coils, respectively. Effect of duty cycle on current and magnetic field ripples was observed by driving an air core coil with 115 kHz self-resonant frequency. Impedance and phase plots, the equivalent circuit and dimensions of the coil are shown in Fig. 3.4-(a) and Fig. 3.4-(b). The coil was driven with varying duty cycles starting from 5% to 95% with 5% increment at 100 Hz, 1 kHz, and 30 kHz. PWM signal amplitude was set to 30 V to pass 1500 mA root mean square current (RMS) from the coil when the duty cycle was 90%.

In order to monitor ohmic losses, coil surface temperature was recorded until it exceeded 60°C, since saturation temperatures of the coil configurations were between 60°C and 80°C. Initial coil surface temperatures were kept as 29°C. Temperature plots are shown in the second row of Fig. 3.3-(b). Ohmic loss change between low and high frequencies is negligible, as observed in the finite element analysis.

Current and magnetic field waveforms of coils at varying PWM frequencies are plotted in the third and fourth row of Fig. 3.3-(b), respectively. Mean, standard deviation, and ripple magnitude of current and magnetic waveforms are shown in TABLE 3.1. RMS and ripple magnitudes of current and magnetic waveforms at varying duty cycles are plotted in Fig. 3.4-(b) and Fig. 3.4-(c). In accordance with our expectations, magnitudes of current and magnetic ripples are significantly reduced when the coils are driven at PWM frequencies close to their resonance frequencies. When PWM drive frequency of Helmholtz coil is changed from 100 Hz to 25 kHz, ripple magnitudes of current and magnetic field are reduced 95,81% and 99,40%, respectively. Hence, driving coils at high

Table 3.1: Mean, standard deviation (std), ripple magnitude (Ripple), root mean square (RMS) of current and magnetic waveforms are presented to show the effect of PWM frequency on current and magnetic field.

	PWM Frequency	Current (mA)				Magnetic Field (mT)			
		Mean	Std	Ripple	RMS	Mean	Std	Ripple	RMS
Iron Core Coil	100 Hz	3,218	75.4	280.2	3,219	58.1	1.2	4.3	58.1
	1 kHz	3,212	14.8	51.5	3,212	58.0	0.1	0.7	58.0
	5 kHz	3,199	4.6	18.9	3,199	56.9	0.1	0.5	56.9
Air Core Coil	100 Hz	3,210	347.2	1,197.2	3,228	9.6	1.4	5.2	9.7
	1 kHz	3,217	35.4	120.6	3,217	9.5	0.2	0.8	9.5
	15 kHz	3,156	1.9	10.1	3,156	8.7	0.1	0.5	8.7
Helmholtz Coil	100 Hz	1,409	447.3	1,497.0	1,478	30.4	7.9	27.1	31.4
	1 kHz	1,397	47.0	167.3	1,397	30.6	0.8	3.7	30.6
	25 kHz	1,397	1.6	9.0	1,397	30.0	0.3	1.1	30.0

frequencies provides nearly two orders of magnitude reduction in ripple magnitudes. This results in the increasing predictability of the field.

RMS values of both the magnetic field and current magnitudes in response to low and high PWM frequencies are close to each other, although there is a significant difference between the ripple magnitudes (see Fig. 3.4 and TABLE 3.1). Even though Teslameters have been used for measuring the RMS value of the magnetic field waveforms in magnetic manipulation studies, they are not suitable for monitoring magnetic field fluctuation at both low and high frequencies [162–164]. This leads to poor current to magnetic field map, which is one of the key components for magnetic manipulation. On the other hand, the experimental setup presented in this paper provides the instantaneous magnitude of the magnetic field and holds a great promise for accurate measurement of both current and magnetic field ripple magnitudes. Besides, the setup significantly minimizes magnetic field magnitudes by driving the coils at higher PWM frequencies. Thus, overall efficiency is significantly improved for precise magnetic manipulation.

4. A Multi-Rate State Observer for Visual Tracking of Magnetic Micro-Agents using Slow Medical Imaging Modalities

Note: The following content is an adapted version of the paper "A multi-rate state observer for visual tracking of magnetic micro-agents using slow medical imaging modalities" by **M. Kaya**, A. Denasi, S. Scheggi, E. Agbahca, C. Yoon, D. H. Gracias, and S. Misra published in "*in Proceedings of the IEEE/RSJ International Conference on Intelligent Robots and Systems (IROS)*", pages 1-8, Madrid, Spain, October, 2018. ■

Abstract

Minimally invasive surgery can benefit greatly from utilizing micro-agents. These miniaturized agents need to be clearly visualized and precisely controlled to ensure the success of the surgery. Since medical imaging modalities suffer from low acquisition rate, multi-rate sampling methods can be used to estimate the intersample states of micro-agents. Hence, the sampling rate of the controller can be virtually increased even if the position data is acquired using a slow medical imaging modality. This study presents multi-rate Luenberger and Kalman state estimators for visual tracking of micro-agents. The micro-agents are tracked using sum of squared differences and normalized cross correlation based visual tracking. Further, the outputs of the two methods are merged to minimize the tracking error and prevent tracking failures. During the experiments, the micro-agents with different geometrical shapes and sizes are imaged using a 2D ultrasound machine and a microscope, and manipulated using electromagnetic coils. The multi-rate state estimation accuracy is measured using a high speed camera. The precision of the tracking and multi-rate state estimation are verified experimentally under challenging conditions. For this purpose, an elliptical-shaped magnetic micro-agent with a length of 48 pixels is used. Maximum absolute error in x and y axes are 2.273 and 2.432 pixels for an 8-fold increase of the sample rate (25 frames per second), respectively. During the experiments, it was observed that the micro-agents could be tracked more reliably using normalized cross correlation based visual tracking and intersample states could be estimated more accurately using

Kalman state estimator. Experimental results show that the proposed method could be used to track micro-agents in medical imaging modalities and estimate system states at intermediate time instants in real-time.

4.1 Introduction

The field of microrobotics has been witnessing a significant progress thanks to the developments in micro-fabrication, sensing and actuation technologies. Minimally invasive surgery (MIS) is among one of its most prominent and promising application domains. Utilizing micro-agents in MIS can reduce patient treatment and recovery time greatly compared to conventional surgery [5]. A successful medical intervention by an operator using microrobotic agents requires clear visualization, accurate sensing and precise feedback control. Numerous studies can be found in the literature about micro-agents controlled using visual feedback. In the following, examples of some of the studies are outlined.

Scheggi *et al.* [165] investigated the closed-loop control of hydrogel grippers using electromagnetic actuation and 2D US images for feedback. Further, collision-free paths were planned using a combination of linear quadratic regulator and rapidly-exploring random tree algorithms. Keuning *et al.* [166] controlled paramagnetic micro-particles using 2D microscope images. Hong *et al.* [167] extracted the 3D position of microrobots from 2D microscope images based on digital in-line holography. Further, a cylindrical permanent magnet was tracked and controlled in 3D. Martel *et al.* [53] developed a platform for steering of magnetic nanorobots using magnetic resonance imaging. In order to provide feedback to the controller, nanorobots were tracked in 3D using their magnetic signatures. Diller *et al.* [145] controlled multiple magnetic microrobots in 3D using magnetic gradient. Microrobots were tracked using two CCD cameras.

The aforementioned studies utilize medical imaging modalities as a feedback source for the controllers since traditional sensors like encoders cannot be embedded on the micro-agents due to their small size. But, these imaging modalities suffer from low acquisition rate. Image acquisition rates of magnetic resonance imaging and computed tomography are in the range of 10 to 20 frames per seconds (fps) and 6 to 15 fps, respectively. Maximum image rates of fluoroscopy and ultrasound imaging can reach up to 30 fps and 100 fps, respectively [5, 168]. An appealing remedy for this drawback is multi-rate state estimation. This method provides estimates of the system states for intermediate time instants where measurements are not available. Multi-rate state estimation has been applied to various fields such as vehicle motion control systems [169], hard disk drive servo control systems [170], and visual servoing of manipulators [171]. In this study, we propose to apply multi-rate Luenberger and Kalman state estimators for the visual tracking outputs of micro-agents in order to have intermediate position data between two consecutive frames. The contribution of this study is that the multi-rate state estimation is applied to the field of microrobotics to virtually increase the sampling rate of position data for control using low-rate visual feedback.

In the literature, detection-based tracking methods are commonly used to find the micro-agents location in the image plane [165, 166]. In these methods, micro-agents are first detected in each frame and then Kalman filter is applied for tracking. Detection of the micro-agents in each frame requires thresholding procedure and values for thresholding change by image. Thus, tracking is prone to failure unless the thresholding values are tuned properly. Besides, this approach ignores the motion information of the micro-agents in the image plane. But, motion information is an important cue and can be used to track

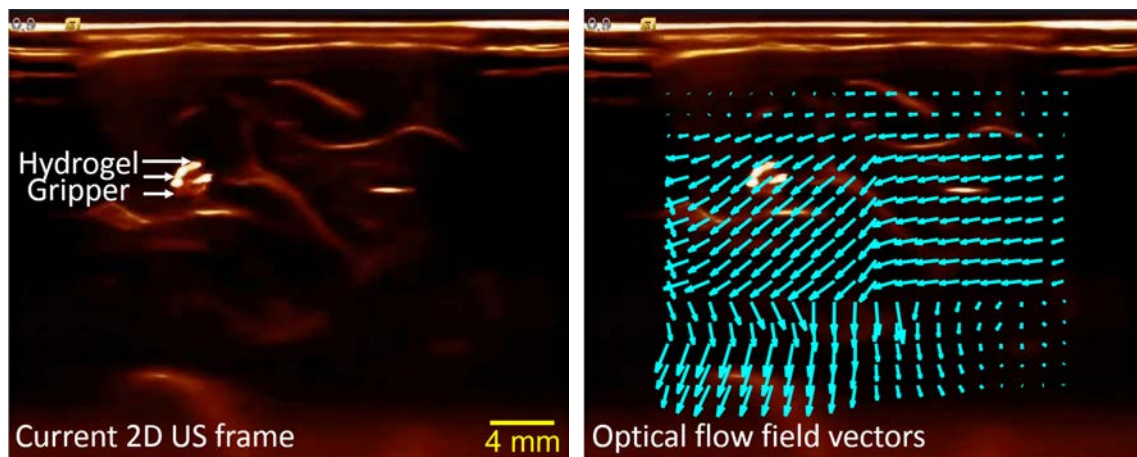


Figure 4.1: Optical flow analysis of the current frame while a hydrogel gripper is magnetically steered. The image on the left shows the current 2D ultrasound (US) frame that contains the hydrogel gripper. The image on the right shows the optical flow field vectors overlaid on the current frame.

the micro-agents. Due to the shortcomings of this approach, micro-agents are tracked in the image plane using similarity functions also known as template-based tracking. In this method, an object is detected once and then tracked by calculating its motion parameters between two close frames without applying any specific detection method. The pixels of micro-agents have considerable motion information when they are steered. The motion analysis of an electromagnetically actuated hydrogel gripper with images acquired from 2D US is shown in Fig. 4.1. The motion in this image is analyzed using the Lucas-Kanade optical flow method [172]. The analyzed motion is represented as a vector field and overlaid onto the current image that is shown in Fig. 4.1. This example shows that micro-agents with different shapes can often be visually tracked using similarity functions with images acquired from any medical imaging modality. In this study, the sum of squared differences (SSD) and the normalized cross correlation (NCC) cost functions are used as similarity functions. During the tracking, the outputs of SSD and NCC methods are merged using Luenberger and Kalman state observers to minimize the tracking error.

In the following section, visual tracking of the micro-agents is explained in detail. Section 4.3 states the multi-rate state estimation problem. This is followed by observer based fusion of SSD and NCC visual tracking methods in Section 4.4. In Section 4.5, experimental setup is introduced and results are given. Finally, conclusions are drawn in Section 4.6.

4.2 Visual Tracking of Magnetic Micro-Agents

Visual tracking provides an estimate of the position of an object in the image plane over time by registering the previous appearance of the object with the current one. The previous image is called the template $T(\mathbf{x})$, and the recent one is called the current image $I(\mathbf{w}(\mathbf{x}, \mathbf{p}))$, where $\mathbf{w}(\mathbf{x}, \mathbf{p})$ denotes the motion model (also known as warping function). This model maps the vector $\mathbf{x} = [x, y]$ with the x - and y - coordinates of $T(\mathbf{x})$ onto $I(\mathbf{w}(\mathbf{x}, \mathbf{p}))$ using the motion parameter vector, \mathbf{p} . The main goal of registration is to find the vector \mathbf{p} that minimizes the difference between $T(\mathbf{x})$ and $I(\mathbf{w}(\mathbf{x}, \mathbf{p}))$ using an optimization algorithm. Briefly, registration process consists of two consecutive stages performed iteratively. In the first stage, the similarity between $T(\mathbf{x})$ and $I(\mathbf{w}(\mathbf{x}, \mathbf{p}))$ is measured using a similarity

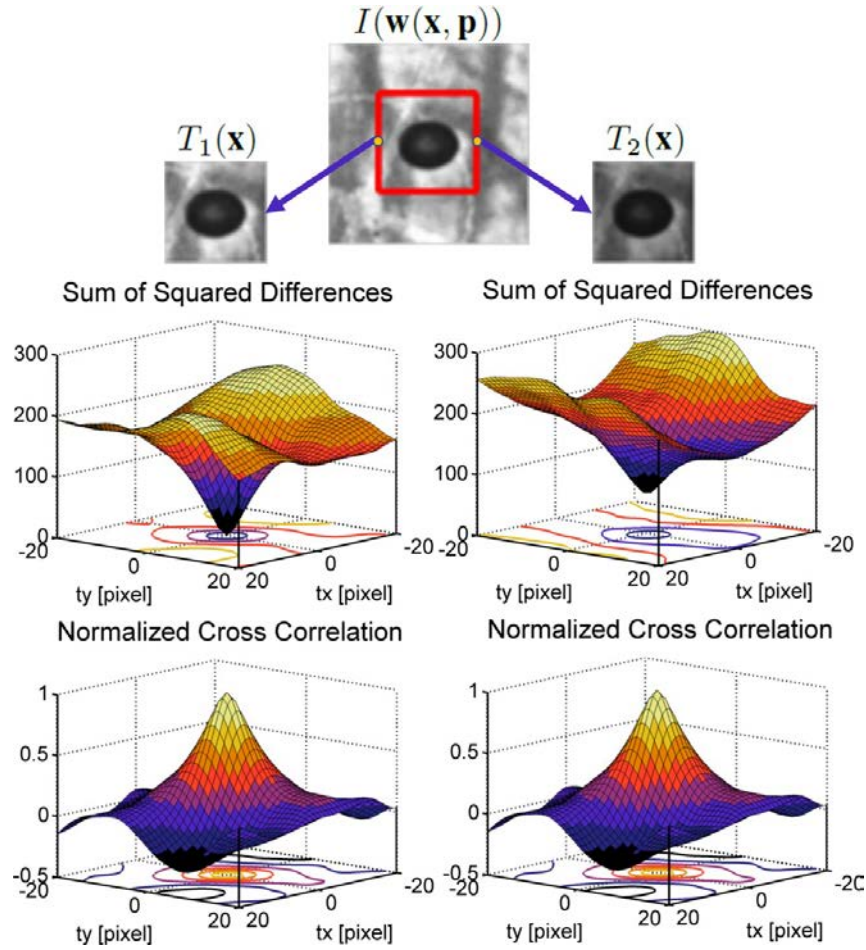


Figure 4.2: 3D similarity plots of sum of squared differences and normalized cross correlation cost functions. Left columns contains similarity plots between $I(\mathbf{w}(\mathbf{x}, \mathbf{p}))$ and $T_1(\mathbf{x})$; right column contains similarity plots between $I(\mathbf{w}(\mathbf{x}, \mathbf{p}))$ and $T_2(\mathbf{x})$. Further, tx and ty are the pixel increments of $T_1(\mathbf{x})$ and $T_2(\mathbf{x})$ with respect to the center of $I(\mathbf{w}(\mathbf{x}, \mathbf{p}))$.

function. In the second stage, the vector \mathbf{p} is calculated.

SSD and NCC cost functions are used to measure the similarity during the registration process. In order to evaluate the performance of these functions, a template image $T_1(\mathbf{x})$ is cropped from $I(\mathbf{w}(\mathbf{x}, \mathbf{p}))$ that contains the micro-agent. The similarity between this image pair is measured by translating $T_1(\mathbf{x})$ from -20 to 20 pixels with 1 pixel increment in x - and y - axes from the center of $I(\mathbf{w}(\mathbf{x}, \mathbf{p}))$. A second template $T_2(\mathbf{x})$ is also created by changing the contrast of $T_1(\mathbf{x})$ to evaluate the performance of the cost functions under intensity changes. Similarity values are plotted in Fig. 4.2. As seen from Fig. 4.2, SSD values reach local minimum and NCC values reach local maximum for two cases in the center of the plots, which confirms that SSD and NCC cost functions can be used for visual tracking of micro-agents. In the rest of this section, motion model selection and visual tracking using SSD and NCC similarity functions are explained.

4.2.1 Motion Model

One of the most significant layers of visual tracking is determining the motion of a micro-agent in the image plane. The motion model describes the transformation between the template and current images. The motion of a micro-agent in the image plane can be

decomposed into translation, rotation, and scaling transformations. These transformations can be described by an affine motion model, $\mathbf{w}(\mathbf{x}, \mathbf{p}) : \mathbb{R}^2 \times \mathbb{R}^6 \rightarrow \mathbb{R}^2$, given as follows:

$$\mathbf{w}(\mathbf{x}, \mathbf{p}) = \begin{bmatrix} (1+p_1) & p_3 \\ p_2 & (1+p_4) \end{bmatrix} \begin{bmatrix} x \\ y \end{bmatrix} + \begin{bmatrix} p_5 \\ p_6 \end{bmatrix}, \quad (4.1)$$

where $\mathbf{p} \in \mathbb{R}^6$ is the 6-DOF motion parameter vector. Further, the motion model (4.1) can be used to track micro-agents with different geometric shapes.

During the visual tracking of micro-agents, illumination variations occur in microscope images and intensity variations occur in other medical imaging modalities (e.g. ultrasound). For successful tracking, illumination and intensity variations must be compensated. A scale-offset model can compensate these variations and consequently the compensated current image $I^*(\mathbf{w}(\mathbf{x}, \mathbf{q}))$, is written as follows:

$$I^*(\mathbf{w}(\mathbf{x}, \mathbf{q})) = (\alpha + 1)I(\mathbf{w}(\mathbf{x}, \mathbf{p})) + \beta, \quad (4.2)$$

where (α, β) are the model parameters. Using the affine motion and scale-offset models, a new parameter vector $\mathbf{q} \in \mathbb{R}^8$ where $\mathbf{q} = [\mathbf{p}^T, \alpha, \beta]^T$ are calculated for the transformation from the template to the current image during the visual tracking. The calculation of \mathbf{q} vector using SSD and NCC cost functions is explained next.

4.2.2 SSD-based Visual Tracking

SSD between $I^*(\mathbf{w}(\mathbf{x}, \mathbf{q}))$ and $T(\mathbf{x})$ can be computed as:

$$SSD(\mathbf{q}) = \sum_{\mathbf{x}} [I^*(\mathbf{w}(\mathbf{x}, \mathbf{q})) - T(\mathbf{x})]^2. \quad (4.3)$$

The main goal of SSD-based visual tracking is to find the vector \mathbf{q} that minimizes the SSD between $T(\mathbf{x})$ and $I^*(\mathbf{w}(\mathbf{x}, \mathbf{q}))$. For this purpose, forward or inverse compositional methods [173], first order optimization, or efficient second order minimization (ESM) methods [174] can be used. Forward and inverse compositional methods include calculation of Hessian matrix. However, calculation of Hessian matrix is computationally expensive. First order optimization method directly ignores calculation of Hessian matrix. But, Hessian matrix should be included in the optimization method to increase the precision of the tracking. In the ESM method, Hessian matrix is estimated using Jacobian of the current and template images, which makes this method more favorable within the four optimization methods. Using this estimation approach, tracking becomes more robust to noise. Besides, its convergence rate is higher as compared to the other optimization methods since the computation time of the \mathbf{q} vector decreases. Therefore, ESM method is used to find the vector \mathbf{q} in this study. Using ESM method, \mathbf{p} is iteratively computed by accumulating $\Delta\mathbf{q}$ in each iteration ($\mathbf{q} \leftarrow \mathbf{q} + \Delta\mathbf{q}$). $\Delta\mathbf{q}$ is computed as follows:

$$\Delta\mathbf{q} = -2(\mathbf{J}(\mathbf{q}_0) + \mathbf{J}(\mathbf{q}_c))^\dagger (I^*(\mathbf{w}(\mathbf{x}, \mathbf{q})) - T(\mathbf{x})), \quad (4.4)$$

where \dagger is the operator for the Moore-Penrose pseudoinverse of a matrix. Further, $\mathbf{J}(\mathbf{q}_0)$ and $\mathbf{J}(\mathbf{q}_c)$ are the Jacobian of $I^*(\mathbf{w}(\mathbf{x}, \mathbf{q}))$ [175, 176]. Before the iteration loop starts, $\mathbf{J}(\mathbf{q}_0)$ is pre-computed. During the iterations, first $\mathbf{J}(\mathbf{q}_c)$ is computed and then $\Delta\mathbf{q}$ is calculated using (4.4). Iterations last until the number of iterations reach a predefined maximum iteration number or sum of $\Delta\mathbf{q}$ vector elements are smaller than the predefined threshold.

4.2.3 NCC-based Visual Tracking

NCC between $I^*(\mathbf{w}(\mathbf{x}, \mathbf{q}))$ and $T(\mathbf{x})$ can be computed as:

$$NCC(\mathbf{q}) = \frac{\sum_{\mathbf{x}} (I^*(\mathbf{w}(\mathbf{x}, \mathbf{q})) - \bar{I}^*) (T(\mathbf{x}) - \bar{T})}{\sqrt{\sum_{\mathbf{x}} (I^*(\mathbf{w}(\mathbf{x}, \mathbf{q})) - \bar{I}^*)^2} \sqrt{\sum_{\mathbf{x}} (T(\mathbf{x}) - \bar{T})^2}}, \quad (4.5)$$

where \bar{T} and \bar{I}^* are the mean values of $T(\mathbf{x})$ and $I^*(\mathbf{w}(\mathbf{x}, \mathbf{q}))$, respectively. The main goal of NCC-based visual tracking is to find the \mathbf{q} that maximizes the NCC between $T(\mathbf{x})$ and $I^*(\mathbf{w}(\mathbf{x}, \mathbf{q}))$. Using Newton optimization method, \mathbf{q} can be iteratively computed by accumulating $\Delta\mathbf{q}$ in each iteration ($\mathbf{q} \leftarrow \mathbf{q} + \Delta\mathbf{q}$). $\Delta\mathbf{q}$ can be computed with the inverse of Hessian (\mathbf{H}^{-1}) matrix and gradient (\mathbf{g}) vector of (4.5) as follows [175]:

$$\Delta\mathbf{q} = -\mathbf{H}^{-1}\mathbf{g}. \quad (4.6)$$

Similar to SSD-based visual tracking, iterations last until the sum of the elements of the vector $\Delta\mathbf{q}$ is smaller than the predefined threshold or the number of iterations reaches the predefined maximum iteration number.

4.2.4 Pyramidal Implementation

In our experiments, it was observed that the motion of the micro-sized agents can be very large in the image plane. In this situation, the displacement of the agents between the previous and the current frames can be large. Hence, the number of iterations to calculate the motion parameters between the template and current images increases dramatically. Further, the agents can be so far away from the search region in the image plane that tracking might fail. In order to increase the convergence rate and robustness of the tracking, pyramidal implementation of the proposed template-based tracking method is applied. During the tracking, optimization methods are first applied to the coarsest level of pyramid and then, results are transferred to the next finer level of the pyramid. The number of pyramid layer for the frames in our data set and imaging system was selected as two [172]. If the number of pyramid layers in the experiments was more than two, significant texture loss was observed because our maximum template size is 60×60 square pixels.

4.2.5 Template Update Strategy

During the tracking, the template images are updated with a drift correction strategy to minimize the registration error and prevent template drifts [177]. This strategy consists of two steps. In the first step, the template and current images are registered. In the second step, the output image obtained in the first step is registered with the master template. The master template is the first appearance of the micro-agent and updated every $1.5 \times \text{fps}$ frames. After the second step, the template image is updated with the registration output obtained in the second step, and the position of the micro-agents is obtained in the image. This position serves as a measurement of the multi-rate state estimators presented in the next section.

4.3 Multi-Rate State Estimation

In this section, a simplified kinematics-based model used to design the multi-rate state estimators is described. This is followed by the theory and application of a multi-rate Luenberger state observer and a multi-rate Kalman filter.

4.3.1 System Description

In the following, we assume that the dynamics of the micro-agents can be approximated by a linear and time-invariant model. Further, the influence of deviations of the actual system from the linear system are modeled with a disturbance term. It is possible to use a sophisticated nonlinear model for multi-rate state estimation. However, the problem with such a model is the identification of its parameters and further the validation of these parameters due to the unavailability of sensors or ground truth in microrobotics. Hence, a disturbance term is used to locally represent the contributions of such nonlinear dynamics. The system (plant) dynamics is expressed in continuous-time as follows:

$$\dot{\mathbf{x}}_p = \mathbf{A}_{pc}\mathbf{x}_p + \mathbf{B}_{pc}\mathbf{u} + \mathbf{B}_{pc}\mathbf{d}, \quad (4.7)$$

$$\mathbf{y} = \mathbf{C}_{pc}\mathbf{x}_p + \mathbf{D}_{pc}\mathbf{u} + \mathbf{v}, \quad (4.8)$$

where $\mathbf{x}_p \in \mathbb{R}^{n_p}$ and $\mathbf{u} \in \mathbb{R}^m$ are the state of the plant and the control input, respectively. Further, $\mathbf{d} \in \mathbb{R}^{n_d}$, $\mathbf{v} \in \mathbb{R}^l$ and $\mathbf{y} \in \mathbb{R}^l$ represent the disturbance, the measurement noise and the measured output, respectively. The measurement noise is assumed to be zero-mean, Gaussian and white. Further, the dynamics of the disturbance term ((4.7) and (4.8)) is denoted as:

$$\dot{\boldsymbol{\eta}}_d = \mathbf{A}_{dc}\boldsymbol{\eta}_d + \mathbf{B}_{dc}\mathbf{w}, \quad (4.9)$$

$$\mathbf{d} = \mathbf{C}_{dc}\boldsymbol{\eta}_d, \quad (4.10)$$

where $\boldsymbol{\eta}_d \in \mathbb{R}^{n_\eta}$ and $\mathbf{w} \in \mathbb{R}^{n_w}$ are the state of the disturbance dynamics and an external driving signal, respectively. The signal \mathbf{w} can either be deterministic but unknown or stochastic with the assumption of being zero-mean, Gaussian and white. If the signal \mathbf{w} is deterministic but unknown and bounded, then a Luenberger state observer can be designed. But, if the signal \mathbf{w} is stochastic with the assumption of being zero-mean, Gaussian and white, then a Kalman filter can be designed. The plant dynamics given by (4.7)-(4.8) and the disturbance dynamics given by (4.9)-(4.10) can be combined into the following augmented system:

$$\dot{\mathbf{x}} = \mathbf{A}_c\mathbf{x} + \mathbf{B}_c\mathbf{u} + \mathbf{B}_{wc}\mathbf{w}, \quad (4.11)$$

$$\mathbf{y} = \mathbf{C}_c\mathbf{x} + \mathbf{D}_c\mathbf{u} + \mathbf{v}, \quad (4.12)$$

where

$$\begin{aligned} \mathbf{A}_c &= \begin{bmatrix} \mathbf{A}_{pc} & \mathbf{B}_{pc}\mathbf{C}_{dc} \\ \mathbf{0}_{n_d \times n_p} & \mathbf{A}_{dc} \end{bmatrix}, \mathbf{B}_c = \begin{bmatrix} \mathbf{B}_{pc} \\ \mathbf{0}_{n_d \times m} \end{bmatrix}, \mathbf{B}_{wc} = \begin{bmatrix} \mathbf{0}_{n_p \times n_w} \\ \mathbf{B}_{dc} \end{bmatrix}, \\ \mathbf{C}_c &= [\mathbf{C}_{pc} \quad \mathbf{0}_{l \times n_\eta}], \quad \mathbf{D}_c = \mathbf{D}_{pc}, \quad \mathbf{x} = [\mathbf{x}_p^T \quad \boldsymbol{\eta}_d^T]^T, \end{aligned} \quad (4.13)$$

where $\mathbf{0}$ is a zero-matrix of appropriate size. For systems with a low sampling rate, an appropriate discretization method should be selected. The sampled representation of a linear time-invariant system given by (4.11)-(4.12) can be obtained exactly using the exact discretization method. The system is discretized with a fast model sampling time, $T_f \in \mathbb{R}_{>0}$ and the measured outputs are obtained with a slower sampling time, $T_s \in \mathbb{R}_{>0}$. These two sampling times satisfy $T_s = NT_f$ where $N \in \mathbb{Z}_{>0}$. In imaging systems, T_s corresponds to reciprocal of the frames per second (1/fps) of the system. The block diagram of the dynamic system ((4.11) and (4.12)) with different sampling rates is shown in Fig. 4.3.

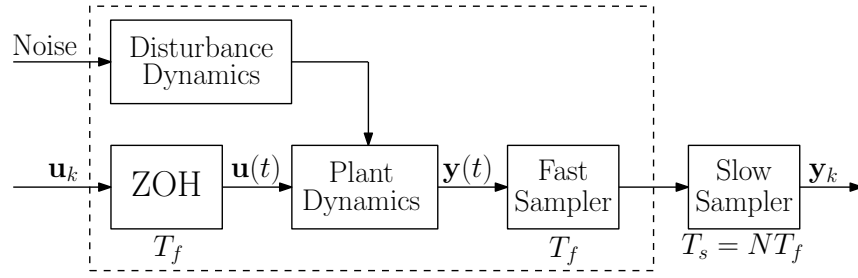


Figure 4.3: The block diagram of a dynamic system sampled at different rates is presented. The system is discretized with a fast model sampling time T_f and the measured outputs are obtained with a slower sampling time T_s .

After discretizing (4.11) and (4.12), the resulting system of difference equations are given as follows:

$$\mathbf{x}[(i+1)T_f] = \mathbf{A}_d \mathbf{x}[iT_f] + \mathbf{B}_d \mathbf{u}[iT_f] + \mathbf{B}_{wd} \mathbf{w}[iT_f], \quad (4.14)$$

$$\mathbf{y}[jT_s] = \mathbf{C}_d \mathbf{x}[jT_s] + \mathbf{D}_d \mathbf{u}[jT_s] + \mathbf{v}[jT_s]. \quad (4.15)$$

The matrices in (4.14)-(4.15) can be computed using

$$\begin{bmatrix} \mathbf{A}_d & \mathbf{B}_d & \mathbf{B}_{wd} \\ \mathbf{0} & \mathbf{I} & \mathbf{0} \\ \mathbf{0} & \mathbf{0} & \mathbf{I} \end{bmatrix} = \exp \left(\begin{bmatrix} \mathbf{A}_c & \mathbf{B}_c & \mathbf{B}_{wc} \\ \mathbf{0} & \mathbf{0} & \mathbf{0} \\ \mathbf{0} & \mathbf{0} & \mathbf{0} \end{bmatrix} T_f \right) \quad (4.16)$$

$$\mathbf{C}_d = \mathbf{C}_c, \mathbf{D}_d = \mathbf{D}_c \quad (4.17)$$

where $\exp(\cdot)$ is the matrix exponential operator [178]. Here, $\mathbf{0}$ and \mathbf{I} are the zero and identity matrices of appropriate size, respectively. For clarity of notation, the sampling time variables in (4.14)-(4.15) are omitted, and we obtain

$$\mathbf{x}(i+1) = \mathbf{A}_d \mathbf{x}(i) + \mathbf{B}_d \mathbf{u}(i) + \mathbf{B}_{wd} \mathbf{w}(i), (i = 1, 2, 3, \dots), \quad (4.18)$$

$$\mathbf{y}(j) = \mathbf{C}_d \mathbf{x}(j) + \mathbf{D}_d \mathbf{u}(j) + \mathbf{v}(j), (j = N, 2N, \dots). \quad (4.19)$$

The system (4.18)-(4.19) can be rewritten using a unified time step k ($k = 1, 2, 3, \dots$) as:

$$\begin{aligned} \mathbf{x}(kN+c+1) &= \mathbf{A}_d \mathbf{x}(kN+c) + \mathbf{B}_d \mathbf{u}(kN+c) + \mathbf{B}_{wd} \mathbf{w}(kN+c), \\ \mathbf{y}(kN) &= \mathbf{C}_d \mathbf{x}(kN) + \mathbf{D}_d \mathbf{u}(kN) + \mathbf{v}(kN), \end{aligned} \quad (4.20)$$

where $c = 0, 1, \dots, N-1$. The multi-rate system of (4.20) can be lifted into a single-rate system (T_s) as follows:

$$\mathbf{x}(kN+N) = \mathbf{A}_e \mathbf{x}(kN) + \mathbf{u}_e + \mathbf{w}_e, \quad (4.21)$$

$$\mathbf{y}(kN) = \mathbf{C}_d \mathbf{x}(kN) + \mathbf{D}_d \mathbf{u}(kN) + \mathbf{v}(kN), \quad (4.22)$$

where

$$\mathbf{A}_e = \mathbf{A}_d^N, \mathbf{u}_e = \sum_{c=0}^{N-1} \mathbf{A}_d^{N-1-c} \mathbf{B}_d \mathbf{u}(kN+c), \quad (4.23)$$

$$\mathbf{w}_e = \sum_{c=0}^{N-1} \mathbf{A}_d^{N-1-c} \mathbf{B}_{wd} \mathbf{w}(kN+c). \quad (4.24)$$

In the following, as an example of (4.11)-(4.12), the model used for estimating the 2D positions of a micro-agent in camera or 2D ultrasound images is explained. Consider the x- and y- position coordinates of the micro-agent denoted by $p_x \in \mathbb{R}$, $p_y \in \mathbb{R}$ and the corresponding velocities denoted by $v_x \in \mathbb{R}$, $v_y \in \mathbb{R}$. We consider the case when there are no control inputs, thus $\mathbf{u} = \mathbf{0}$ holds. Considering the state vector $\mathbf{x}_p = [p_x \ p_y \ v_x \ v_y]^T$ and the disturbance vector $\mathbf{d} = [d_x \ d_y]^T$, the system dynamics is given as follows:

$$\underbrace{\begin{bmatrix} \dot{p}_x \\ \dot{p}_y \\ \dot{v}_x \\ \dot{v}_y \end{bmatrix}}_{\dot{\mathbf{x}}_p} = \underbrace{\begin{bmatrix} 0 & 0 & 1 & 0 \\ 0 & 0 & 0 & 1 \\ 0 & 0 & 0 & 0 \\ 0 & 0 & 0 & 0 \end{bmatrix}}_{\mathbf{A}_{pc}} \underbrace{\begin{bmatrix} p_x \\ p_y \\ v_x \\ v_y \end{bmatrix}}_{\mathbf{x}_p} + \underbrace{\begin{bmatrix} 0 & 0 \\ 0 & 0 \\ 1 & 0 \\ 0 & 1 \end{bmatrix}}_{\mathbf{B}_{pc}} \underbrace{\begin{bmatrix} d_x \\ d_y \end{bmatrix}}_{\mathbf{d}}, \quad (4.25)$$

$$\mathbf{y} = \underbrace{\begin{bmatrix} 1 & 0 & 0 & 0 \\ 0 & 1 & 0 & 0 \end{bmatrix}}_{\mathbf{C}_{pc}} \mathbf{x}_p + \underbrace{\begin{bmatrix} v_x \\ v_y \end{bmatrix}}_{\mathbf{v}}, \quad (4.26)$$

where the matrices given by (4.7)-(4.8) are used. The system dynamics described by \mathbf{A}_{pc} in (4.25) with $\mathbf{d} = \mathbf{0}$ is commonly used in vision applications in the literature. However, in order to have a more general yet simple model, a disturbance term should be included. There are different ways to model the disturbance term depending on the application. In order to keep the formulation sufficiently general a polynomial function is selected [179]. The disturbance term can be locally represented by an $(n-1)^{\text{th}}$ degree family of Taylor polynomial function of time as follows:

$$d_j(t) = \sum_{i=0}^{n-1} d_{j,i} t^i + d_{j,r}(t), \quad (4.27)$$

where $j \in \{x, y\}$, $d_{j,i} \in \mathbb{R}$ and $d_{j,r}(t) \in \mathbb{R}$ are the coefficients of the polynomial and a residual term, respectively. It is assumed that the residual term, $d_{j,r}(t)$, is such that its time derivatives for $i \geq n$ satisfy $|d_{j,r}^{(i)}(t)| \leq \gamma_{i-r} \approx 0$, thus they are all uniformly absolutely bounded and small enough to be negligible [179]. This implies that the residual term is slowly varying with respect to time. When, the degree of the polynomial is n we obtain,

$$\underbrace{\begin{bmatrix} \dot{\eta}_{d,1} \\ \dot{\eta}_{d,2} \\ \vdots \\ \dot{\eta}_{d,n-1} \\ \dot{\eta}_{d,n} \end{bmatrix}}_{\dot{\boldsymbol{\eta}}_d} = \underbrace{\begin{bmatrix} \mathbf{0}_2 & \mathbf{I}_2 & \dots & \mathbf{0}_2 & \mathbf{0}_2 \\ \mathbf{0}_2 & \mathbf{0}_2 & \dots & \mathbf{0}_2 & \mathbf{0}_2 \\ \vdots & \vdots & \ddots & \vdots & \vdots \\ \mathbf{0}_2 & \mathbf{0}_2 & \dots & \mathbf{0}_2 & \mathbf{I}_2 \\ \mathbf{0}_2 & \mathbf{0}_2 & \dots & \mathbf{0}_2 & \mathbf{0}_2 \end{bmatrix}}_{\mathbf{A}_{dc}} \underbrace{\begin{bmatrix} \boldsymbol{\eta}_{d,1} \\ \boldsymbol{\eta}_{d,2} \\ \vdots \\ \boldsymbol{\eta}_{d,n-1} \\ \boldsymbol{\eta}_{d,n} \end{bmatrix}}_{\boldsymbol{\eta}_d} + \underbrace{\begin{bmatrix} \mathbf{0}_2 \\ \mathbf{0}_2 \\ \vdots \\ \mathbf{0}_2 \\ \mathbf{I}_2 \end{bmatrix}}_{\mathbf{B}_{dc}} \underbrace{\begin{bmatrix} d_{x,r}^{(n)} \\ d_{y,r}^{(n)} \end{bmatrix}}_{\mathbf{w}},$$

$$\underbrace{\begin{bmatrix} d_x \\ d_y \end{bmatrix}}_{\mathbf{d}} = \underbrace{\begin{bmatrix} \mathbf{I}_2 & \mathbf{0}_2 & \dots & \mathbf{0}_2 & \mathbf{0}_2 \end{bmatrix}}_{\mathbf{C}_{dc}} \boldsymbol{\eta}_d, \quad (4.28)$$

where $\mathbf{0}_2$ and \mathbf{I}_2 are zero and identity matrices, respectively. Further, in (4.28) each element of the state vector $\boldsymbol{\eta}_d$ satisfies $\boldsymbol{\eta}_{d,i} \in \mathbb{R}^2$. In the following subsections, the applications of multi-rate Luenberger state observer and multi-rate Kalman filter to the system described by (4.21) and (4.22) are detailed.

4.3.2 A Multi-Rate Luenberger Observer

The standard Luenberger observer uses the model of a given system together with a suitable update term to estimate state variables that cannot be measured. In order to apply it to the multi-rate augmented system dynamics ((4.14)-(4.15)) certain modifications are required [180]. First of all the system (4.21)-(4.22) should be observable. This condition is satisfied for the micro-agent dynamics described in Section 4.3.1. This is satisfied if the observability matrix $\mathcal{O}^T = \begin{bmatrix} \mathbf{C}_d^T & \mathbf{A}_e^T \mathbf{C}_d^T & \dots & (\mathbf{A}_e^{n_p+n_d-1})^T \mathbf{C}_d^T \end{bmatrix}$ has full rank, i.e. $\text{rank}(\mathcal{O}) = n_p + n_d$. Since $\mathbf{y}(kN)$ is only available every N^{th} step for the samples between kN and $kN + N$, the value $\mathbf{y}(kN)$ has to be used in the feedback term. Thus, the observer is given as follows:

$$\hat{\mathbf{x}}(kN + 1 + c) = \mathbf{A}_d \hat{\mathbf{x}}(kN + c) + \mathbf{B}_d \mathbf{u}(kN + c) - \mathbf{L}(\hat{\mathbf{y}}(kN) - \mathbf{y}(kN)) \quad (4.29)$$

for $c = 0, 1, \dots, N - 1$ with the observer state $\hat{\mathbf{x}}(kN + c)$ and feedback gain matrix \mathbf{L} . The observer state $\hat{\mathbf{x}}(kN + N)$ after N time steps is given as follows:

$$\hat{\mathbf{x}}(kN + N) = \mathbf{A}_e \hat{\mathbf{x}}(kN) + \mathbf{u}_e - \left(\sum_{c=0}^{N-1} \mathbf{A}_d^c \right) \mathbf{L}(\hat{\mathbf{y}}(kN) - \mathbf{y}(kN)) \quad (4.30)$$

and the observed output $\hat{\mathbf{y}}(kN)$ is given by

$$\hat{\mathbf{y}}(kN) = \mathbf{C}_d \hat{\mathbf{x}}(kN) + \mathbf{D}_d \mathbf{u}(kN). \quad (4.31)$$

Using (4.21), (4.22) and (4.30) and defining the observation error as $\mathbf{e}(kN) = \hat{\mathbf{x}}(kN) - \mathbf{x}(kN)$, the error dynamics can be given as follows:

$$\mathbf{e}(kN + N) = (\mathbf{A}_e - \bar{\mathbf{L}} \mathbf{C}_d) \mathbf{e}(kN) + \bar{\mathbf{L}} \mathbf{v}(kN) - \mathbf{w}_e, \quad (4.32)$$

where $\bar{\mathbf{L}} = (\sum_{c=0}^{N-1} \mathbf{A}_d^c) \mathbf{L}$ is an auxiliary feedback gain matrix. This is done such that if the system is observable, the eigenvalues of the nominal system (i.e. for $\mathbf{v} = 0$ and $\mathbf{w}_e = 0$) can be placed at arbitrary locations, for instance using Ackermann's formula. Consequently, the observer gain matrix \mathbf{L} can be selected as follows:

$$\mathbf{L} = \left(\sum_{c=0}^{N-1} \mathbf{A}_d^c \right)^{-1} \bar{\mathbf{L}} \quad (4.33)$$

when the inverse of the matrix $\sum_{c=0}^{N-1} \mathbf{A}_d^c$ exists. The nominal system is asymptotically stable if all of the eigenvalues are inside the unit disk. The stability of the error dynamics (4.32) can be shown using a variation of the input-to-state stability theorem [181].

4.3.3 A Multi-Rate Kalman Filter

The application of a Kalman Filter to a system with multiple sampling rates where the measurement sampling rate is low, is different as compared to a standard Kalman filter [170]. The multi-rate Kalman filter involves two steps; prediction and correction. In the prediction step, there are no available measurements in between the measurement sampling instants. Therefore, the prediction is based on the augmented system dynamics (4.18)-(4.19) which is an open-loop system. Denote $\hat{\mathbf{x}}(i|j)$ as the estimate of $\hat{\mathbf{x}}(i)$ based

on the measurement before and on time jT_s . At the time instants $t = (Nk + m)T_f$ ($\forall m = 1, 2, \dots, N$), the fast-rate estimate is given as follows:

$$\hat{\mathbf{x}}(Nk + m|Nk) = \mathbf{A}_d^m \hat{\mathbf{x}}(Nk|Nk) + \sum_{c=0}^{m-1} \mathbf{A}_d^{m-1-c} \mathbf{B}_d \mathbf{u}(kN + c). \quad (4.34)$$

At the time instants $t = N(k+1)T_f$, new measurements $\mathbf{y}(Nk+N)$ are available. Therefore, in the correction step the estimate is given as follows:

$$\begin{aligned} \hat{\mathbf{x}}(Nk+N|Nk+N) &= \hat{\mathbf{x}}(Nk+N|Nk) \\ &+ \mathbf{K}(k+1) [\mathbf{y}(Nk+N) - \mathbf{C}_d \hat{\mathbf{x}}(Nk+N|Nk)]. \end{aligned} \quad (4.35)$$

Consequently, the gain matrix \mathbf{K} is updated through

$$\mathbf{K}(k+1) = \mathbf{M}(k+1) \mathbf{C}_d^T [\mathbf{C}_d \mathbf{M}(k+1) \mathbf{C}_d^T + \mathbf{V}]^{-1} \quad (4.36)$$

$$\begin{aligned} \mathbf{M}(k+1) &= \mathbf{A}_e \mathbf{M}(k) \mathbf{A}_e^T + \mathbf{W}_e \\ &- \mathbf{A}_e \mathbf{M}(k) \mathbf{C}_d^T [\mathbf{C}_d \mathbf{M}(k) \mathbf{C}_d^T + \mathbf{V}]^{-1} \mathbf{C}_d \mathbf{M}(k) \mathbf{A}_e^T, \end{aligned} \quad (4.37)$$

where \mathbf{V} and \mathbf{W}_e are the covariances of the measurement \mathbf{v} and process noise \mathbf{w}_e , respectively. The covariance for the measurement noise is given by $\mathbf{V} = \text{cov}(\mathbf{v})$. Since, the correction step occurs every N samples with the slow sampling time T_s , the covariance of the process noise for (4.21) should be used. The covariance of the process noise \mathbf{w}_e for the system (4.21) with the slow sampling time T_s can be related to the covariance of the process noise \mathbf{w} for the system (4.18) with the fast sampling time T_f using (4.24) as:

$$\begin{aligned} \mathbf{W}_e &= \text{cov} \left(\sum_{c=0}^{N-1} \mathbf{A}_d^{N-1-c} \mathbf{B}_{wd} \mathbf{w}(kN+c) \right) = E [\mathbf{w}_e \mathbf{w}_e^T] \\ &= \left(\sum_{c=0}^{N-1} \mathbf{A}_d^{N-1-c} \mathbf{B}_{wd} \right) \mathbf{W} \left(\sum_{c=0}^{N-1} \mathbf{A}_d^{N-1-c} \mathbf{B}_{wd} \right)^T, \end{aligned} \quad (4.38)$$

where $\mathbf{W} = \text{cov}(\mathbf{w})$ and $E[\cdot]$ is the expectation operator.

4.4 Collaborative Tracking using Observers

One of the most important issues in visual tracking is error minimization. After the template and current images are registered to find the position of a micro-agent in the current image, there is a residual error called the registration error. If the registration error is not minimized during the tracking, the error accumulates over time and tracking eventually fails. In order to minimize the error, template update with drift correction strategy is used. This method is efficient when a micro-agent is tracked using only one of the visual tracking methods. In this study, SSD and NCC based visual tracking methods are used to collaboratively track the micro-agents [182]. If these two methods are used to track micro-agents in parallel, the outputs of these methods can be merged using either a Kalman or a Luenberger state observer to minimize the error. Thus, tracking becomes

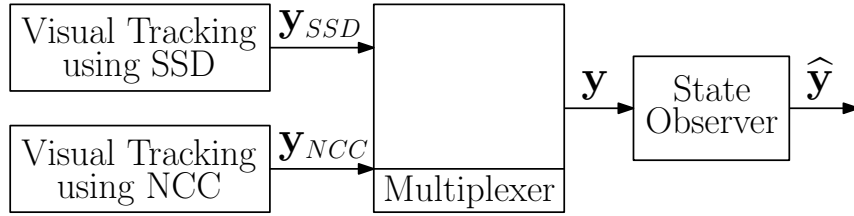


Figure 4.4: Observer based merging scheme for sum of squared differences (SSD) and normalized cross correlation (NCC) based tracking.

more accurate and resilient to failures. The data obtained from the SSD and NCC based visual tracking methods can be merged as follows:

$$\mathbf{y} = \begin{bmatrix} \mathbf{y}_{SSD} \\ \mathbf{y}_{NCC} \end{bmatrix} = \begin{bmatrix} \mathbf{C}_d \\ \mathbf{C}_d \end{bmatrix} \mathbf{x} + \begin{bmatrix} \mathbf{v}_{SSD} \\ \mathbf{v}_{NCC} \end{bmatrix}, \quad (4.39)$$

where \mathbf{y}_{SSD} and \mathbf{y}_{NCC} are the outputs of the SSD and NCC visual tracking methods, respectively. Further, \mathbf{v}_{SSD} and \mathbf{v}_{NCC} denote the registration errors of SSD and NCC, respectively. The scheme of the merging is shown in Fig. 4.4.

4.5 Experiments

In this section, the experimental setup is first described. This is followed by execution times and experimental results.

4.5.1 Experimental Setup

In the experiments, four iron-core coils placed on the same plane were used for planar manipulation of the micro-agents. Each coil was driven by an Elmo 1/60 Whistle DC servo drive. Further details about the electromagnetic setup can be found in our previous work [107, 165]. During the manipulation of the micro-agents, 2D US images were acquired using a Siemens ACUSON S2000 US machine with a 18L6HD linear 2D US probe. The acquired 2D US images were transferred to the computer using an Epiphan DVI2USB 3.0 frame grabber. Microscope images of the micro-agents were captured using an Optem FUSION 7:1 zoom lens module and a XIMEA xiQ USB 3.0 high speed camera pair.

4.5.2 Execution Times

The proposed method was implemented using both MATLAB and C++ with OpenCV library. All of the experiments were performed on a MacBook Pro which has a 2.9 GHz Intel Core i5 CPU with 8 GB RAM. During the tracking, the size of the template images was 60×60 square pixels. The maximum iteration number and the predefined threshold for terminating the iterations were set to 20 and 0.01, respectively. The average execution times were measured as 69.68 [ms] in MATLAB and 13.22 [ms] in C++, respectively. The execution time of the proposed method was significantly reduced in C++ implementation, up to five fold, that allows the real-time execution of the proposed method with the frame rate of the imaging device, which is about 75 *fps*.

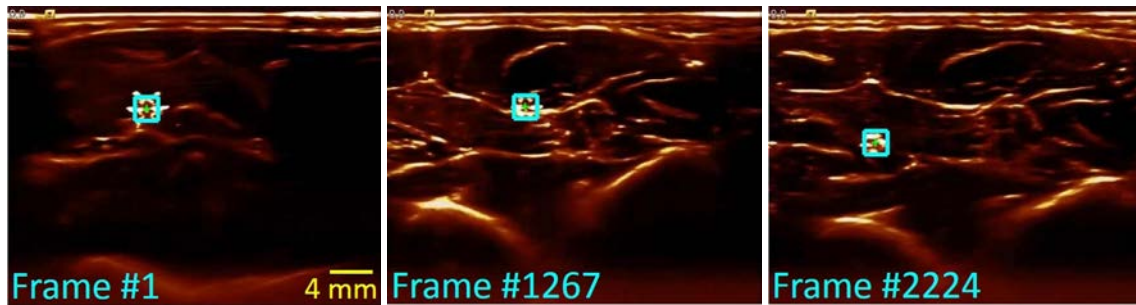


Figure 4.5: Tracking results for a gripper with a tip-to-tip distance of 4 mm in 2D ultrasound images.

4.5.3 Experimental Results

Visual Tracking Results

During the experiments, magnetic hydrogel grippers, spherical and elliptical-shaped micro-agents are used. All of the agents are imaged using a microscope and a 2D US machine. In total, 120652 images are acquired. During the image acquisition, minimum and maximum fps are 14 and 200, respectively. In order to evaluate the tracking performance, an elliptical-shaped micro-agent was manipulated using the electromagnetic system for 65 seconds. During the manipulation, frames were acquired at 198 fps and 12801 frames were captured in total. The tracking performance was quantitatively evaluated by computing both NCC and a combination of Forward-Backward error and NCC (FB+NCC) values [183]. NCC value was computed between the template image and the image obtained after registration. In order to compute the FB+NCC value, the image obtained after registration, called the forward image, and the previous frame was registered to obtain the backward image. NCC+FB value was calculated by computing NCC value between the backward and the template images. NCC and FB+NCC values were computed as 0.9943 ± 0.0117 and 0.9970 ± 0.0082 , respectively. As mentioned in Section II, SSD and NCC based visual tracking methods can fail if the agent moves too much between the measurements. This was experimentally tested by magnetically steering an elliptical-shaped micro-agent with a length of 48 pixels. It was observed that if the Euclidean distance between the agent positions in two consecutive frames is more than 38 pixels, which corresponds to a velocity of 163.57 mm/s , tracking fails. But such a movement is an extreme case in our system.

Visual tracking results of a magnetic hydrogel gripper with a tip-to-tip distance of 4 mm in 2D US images are shown in Fig. 4.5. The images are acquired at 30 fps and the gripper is manipulated using magnetic fields in a water filled tube. Synthetic artifacts are also added to the images to show that the proposed visual tracking method can track the micro-agents in a dynamic background and under realistic conditions. In order to obtain synthetic artifacts, abdominal region of a volunteer is scanned and recorded with a 2D US probe. After the raw image is acquired during manipulation of the gripper, the raw and abdominal images are superimposed.

A 1 mm elliptical-shaped micro-agent is tracked in microscope images. Before image acquisition, a printed vein pattern is placed at the bottom of the Petri dish and the agent is magnetically steered. The motion of the micro-agent in the images consists of translation and rotation transformations. The agent is successfully tracked using the proposed visual tracking method. During the tracking, images are acquired at 20 fps. Fig. 4.6 shows results of visual tracking.

Tracking results for a 1 mm spherical micro-agent in microscope images are shown in

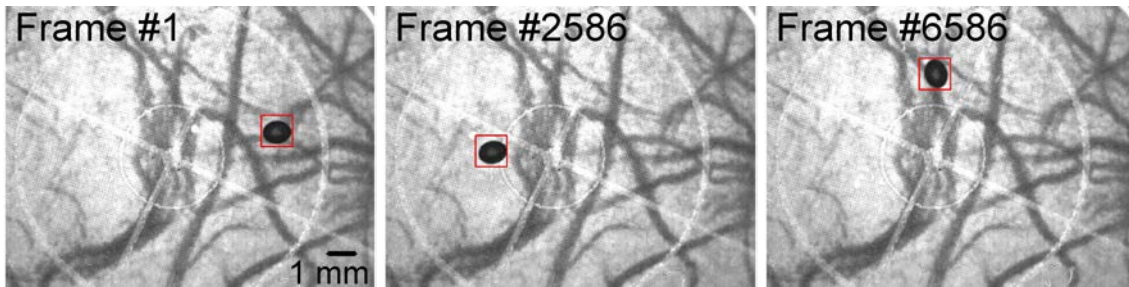


Figure 4.6: Tracking results for a 1 mm elliptical-shaped micro-agent in microscope images.

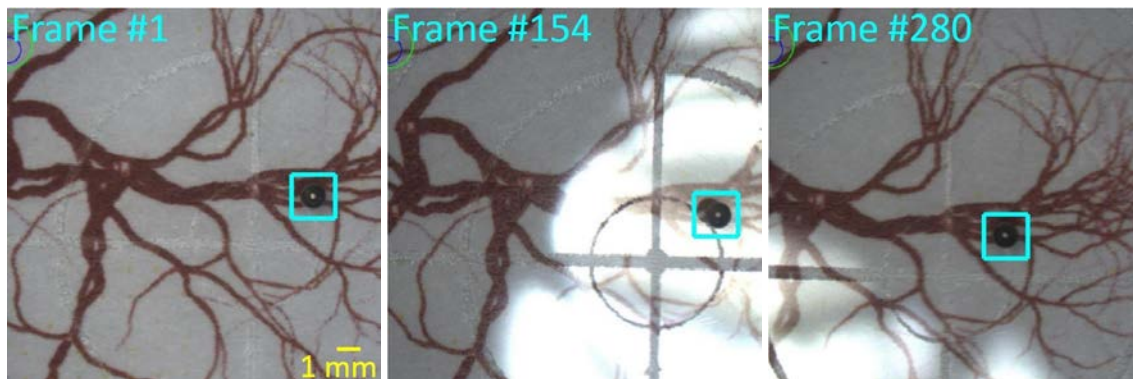


Figure 4.7: Tracking results for a 1 mm spherical-shaped micro-agent in microscope images under large motion displacements and significant illumination variations.

Fig. 4.7. Similar to the previous experiment, the Petri dish is put on a printed vein pattern. Images are acquired at 25 fps. Instead of moving the agents using magnetic fields, the Petri dish is moved by hand to test the tracking robustness under large motion displacements. Also, this image sequence suffers from strong illumination variations. The center image shown in Fig. 4.7 suffers from strong light intensity and shadow. Further, the right image shown in Fig. 4.7 suffers from low intensity. The agent is successfully tracked under these conditions which confirms the robustness of the proposed visual tracking method.

The proposed visual tracking method can also track multiple micro-sized agents. In our experiments, two spherically-shaped 100 μm agents are moved independently using the controller described in [107]. The micro-agents are imaged using a microscope and tracked using both SSD and NCC based methods. During the tracking, images are acquired at 40 fps and the micro-agents are tracked in parallel.

Multi-Rate State Estimation Results

The accuracy of multi-rate state estimation was evaluated using a high speed camera. We have implemented both Luenberger and Kalman state estimators offline. An elliptical-shaped micro-agent with a length of 48 pixels was magnetically steered for 50 seconds. During the manipulation, frames were acquired at 200 fps and 9091 frames were captured in total. The accuracy of multi-rate state estimation is evaluated by tracking the particle at 200 fps which serves as ground truth. Then, multi-rate state estimation was performed by reducing the acquisition rate to 25, 50, 100 fps for N equals to 2, 4, and 8, respectively. Note that $\mathbf{B}_d = \mathbf{0}$ and $\mathbf{D}_d = \mathbf{0}$ holds for the system (4.25) and (4.26). Maximum absolute error (M.A.E) in x - and y - axes, mean and standard deviation of the error for different

Table 4.1: Maximum absolute error (M.A.E), mean error, and standard deviation (std) are presented to compare performance between Luenberger and Kalman multi-rate estimation. All units are given in pixels.

		$n_d = 0$		$n_d = 1$		$n_d = 2$	
		(Luen.)	(Kalm.)	(Luen.)	(Kalm.)	(Luen.)	(Kalm.)
$N = 2$	M.A.E. -X	1.203	0.848	0.688	0.842	0.656	0.808
	M.A.E. -Y	1.364	0.977	0.794	0.759	0.761	0.745
	Mean	0.324	0.106	0.230	0.071	0.214	0.065
	Std	0.197	0.094	0.107	0.074	0.010	0.073
$N = 4$	M.A.E. -X	3.952	1.779	1.211	1.222	0.721	0.864
	M.A.E. -Y	2.590	1.676	1.082	1.310	0.765	1.360
	Mean	0.946	0.333	0.334	0.166	0.236	0.110
	Std	0.746	0.301	0.195	0.164	0.113	0.125
$N = 8$	M.A.E. -X	12.022	6.196	3.908	4.806	1.793	2.273
	M.A.E. -Y	6.883	4.496	3.093	4.060	1.186	2.432
	Mean	3.237	1.231	0.959	0.819	0.403	0.355
	Std	2.441	1.109	0.733	0.793	0.305	0.394

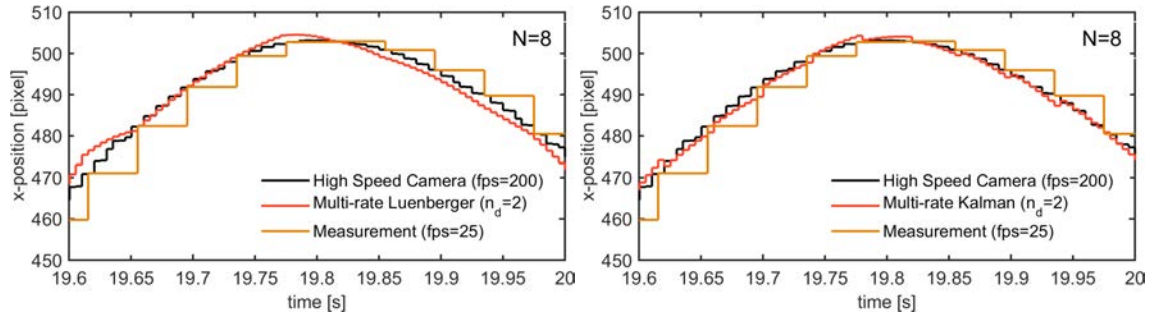


Figure 4.8: Multi-rate sampling results using a Luenberger observer (top) and a Kalman filter (bottom) along the x - axis for N equals to 8 and n_d equal 2.

values of N and n_d as described in Section 4.3.1 are tabulated in Table 4.1 in pixels. An example output of multi-rate state estimation using Luenberger observer and Kalman filter in x - axes for N equal to 8 and n_d equal to 2 were depicted in Fig. 4.8. It can be observed from Table 4.1, when n_d increases, the accuracy of the estimated state obtained using either a Kalman or a Luenberger state estimator and when N increases, the accuracy of the estimates reduces as expected.

Collaborative Tracking Results

A $100\mu\text{m}$ spherical-shaped micro-agent is tracked with SSD and NCC based visual tracking methods in parallel. After each registration of template and current images, the outputs are merged separately by Luenberger (4.29) and Kalman (4.34), (4.35), (4.37), (4.38) estimators. Further, the merging is also applied to the case of multi-rate sampling. The results are shown in Fig. 4.9.

4.6 Conclusions

This study presents multi-rate Luenberger and Kalman state estimators for visual tracking of magnetic micro-agents. The main contribution is the intersample state estimation of micro-agents using slow medical imaging modalities. The micro-agents are tracked using

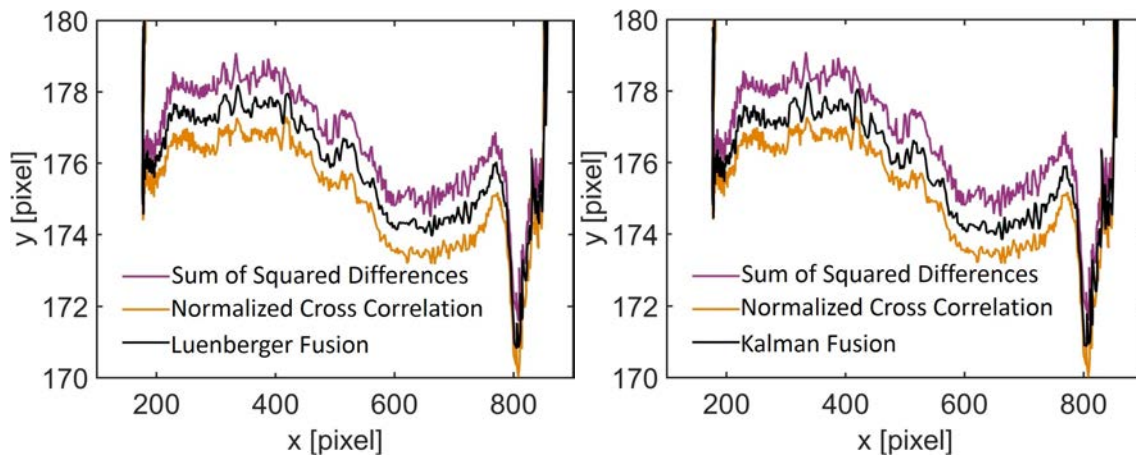
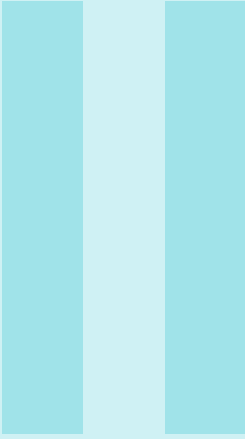


Figure 4.9: Results of the merging process using Luenberger (left) and Kalman (right) state estimators.

SSD and NCC cost functions in medical images. Further, the outputs of SSD and NCC are merged using state estimators for robust tracking. During the experiments, magnetic micro-agents with different shapes are steered using coils and imaged separately with a 2D US machine and a microscope. The advantages of the proposed method are demonstrated by means of extensive experiments under challenging conditions such as strong illumination and intensity variations and large motion displacements. During the experiments, it was observed that Kalman filter was more accurate than Luenberger observer and the agents could be tracked more reliably using NCC based visual tracking compared to SSD based visual tracking. Experimental results demonstrate that the proposed method can accurately track micro-agents with different shapes in images obtained from slow medical imaging modalities while providing intersample estimates in real-time. We envision that this method could be readily utilized with clinical instrumentation to accelerate translation of the use of microrobots in realistic minimally invasive operations.



System Integration and Real-Time Multicolor Fluorescence Microscopy

5	Real-Time Multicolor Microscopy	87
5.1	Introduction	
5.2	Methods	
5.3	Results	
5.4	Conclusions	

PREFACE

Part II (Chapter 5) expands the scope of multicolor fluorescence microscopy by real-time visualization of micro-agents in 3D tumor-on-a-chip and vascular networks. Imaging experiments are conducted using the multicolor microscope developed in **Part I (Chapters 2-4)**. The performance of the microscope is reported in **Chapter 2** using commercial fluorescent beads as micro-agents. However, the relatively low photobleaching resistance of the beads limits the imaging time. In this part, magnetic and fluorescent micro-agents at varying aspect ratios are fabricated using straight and beaded fibers synthesized by the electrospinning process. A polymer solution for electrospinning is presented to obtain micro-agents with relatively high photobleaching resistance and prolong the imaging time. Characterization experiments are carried out to visualize structural morphology and analyze the spectrum of the fabricated micro-agents. The microscope is combined with an electromagnetic coil array powered by the drivers introduced in **Chapter 3** to manipulate the micro-agents. **Chapter 5** demonstrates that multicolor microscopy performed using the round-robin strategy provides spatiotemporal resolution for visualizing magnetically actuated micro-agents and dynamic surroundings.

Cancer cell spheroids formed with the method in **Chapter 2** are actuated using the micro-agents in an open reservoir to visualize the sequential motion from all the spectrum bands in the multicolor microscope. The path and velocity information of spheroids to which micro-agents are attached is obtained using the template-based visual tracker presented in **Chapter 4**. Lucas-Kanade optical flow method is employed for depicting the motion of spheroids and micro-agents as vector fields. The open reservoir as an experimental testbed creates a dynamic environment by allowing translational and rotational mobility of the spheroids using micro-agents. Additionally, it provides random positioning of the spheroids. A microfluidic chip is developed to immobilize a single spheroid in a fixed location using a U-shaped pillar array and air bubble. Single and multiple micro-agents are attached to the immobilized spheroids by puncturing and electrostatic interaction as a proof-of-concept targeted drug delivery demonstration. Dynamic multicolor imaging is utilized as a passive method for attachment verification. The attachment experiments are repeated in the open reservoir to demonstrate the chip (1) maintains the spheroids to which micro-agents are attached for long-term microscopy and (2) allows fluorescence recovery after photobleaching for prolonging multicolor imaging time.

A non-vascularized tumor environment is created using the chip to validate real-time multicolor image acquisition. In order to show that multicolor microscopy is capable of visualizing the micro-agents within vascularized environments, a perfusable vascular network is engineered on a microfluidic system using red fluorescence protein - human umbilical vein endothelial cells. Visualizing micro-agents inside the vascular network allows (1) testing the microscope under *in vitro* conditions and (2) multicolor image acquisition using endogenous and exogenous fluorophores. The chicken chorioallantoic membrane (CAM) is employed to visualize micro-agents in natural blood vessels. Real-time images are acquired through experiments where the micro-agents are magnetically pulled outside and inside the blood vessels. **Chapter 5** is concluded by emphasizing that multicolor microscopy provides spectrally resolved and real-time visualization of polymeric micro-agents, organic bodies (spheroids and vessels), and surrounding media.

5. Visualization of Magnetic Micro-Agents and Dynamic Surroundings by Real-Time Multicolor Fluorescence Microscopy

Note: The following content is an adapted version of the paper "Visualization of Micro-Agents and Surroundings by Real-Time Multicolor Fluorescence Microscopy" by **M. Kaya**, F. Stein, P. Padmanaban, Z. Zhang, J. Rouwkema, I. S. M. Khalil, and S. Misra published in "*Nature Scientific Reports*", 12(13375), August 2022. ■

Abstract

Optical microscopy techniques are a popular choice for visualizing micro-agents. They generate images with relatively high spatiotemporal resolution but do not reveal encoded information for distinguishing micro-agents and surroundings. This study presents multicolor fluorescence microscopy for rendering color-coded identification of mobile micro-agents and dynamic surroundings by spectral unmixing. We report multicolor microscopy performance by visualizing the attachment of single and cluster micro-agents to cancer spheroids formed with HeLa cells as a proof-of-concept for targeted drug delivery demonstration. A microfluidic chip is developed to immobilize a single spheroid for the attachment, provide a stable environment for multicolor microscopy, and create a 3D tumor model. In order to confirm that multicolor microscopy is able to visualize micro-agents in vascularized environments, *in vitro* vasculature network formed with endothelial cells and *ex ovo* chicken chorioallantoic membrane are employed as experimental models. Full visualization of our models is achieved by sequential excitation of the fluorophores in a round-robin manner and synchronous individual image acquisition from three-different spectrum bands. We experimentally demonstrate that multicolor microscopy spectrally decomposes micro-agents, organic bodies (cancer spheroids and vasculatures), and surrounding media utilizing fluorophores with well-separated spectrum characteristics and allows image acquisition with 1280×1024 pixels up to 15 frames per second. Our results display that real-time multicolor microscopy provides increased understanding by color-coded visualization regarding the tracking of micro-agents, morphology of organic

bodies, and clear distinction of surrounding media.

5.1 Introduction

The field of microrobotics has opened up new avenues for various applications in medicine thanks to the advances in micro/nano-fabrication technologies [5, 39, 184]. One of the most prominent applications is targeted drug delivery, which is an innovative technique to increase the success rate of the treatment, mitigate the side effects of the medications, and reduce patient recovery time [23, 185]. Micro-agents, the end-effectors of the microrobotics systems, are utilized as carriers for nano-particle drug delivery and steered towards the tissue of interest by external stimuli (e.g., magnetic fields and acoustic waves) [186]. Imaging techniques are utilized for micro-agents to reach the target tissue since sensor integration remains a challenge due to size limitations [61, 187]. Acquired images can be considered only feedback source for target identification, manipulation of the micro-agents, and releasing the drugs in the desired location. Therefore, clear visualization plays a crucial role in the delivery process.

Magnetic resonance imaging (MRI), computed tomography (CT), fluoroscopy, ultrasound, and photoacoustic imaging are used to visualize micro-agents *in vitro* and *in vivo* conditions. MRI is used for simultaneous actuation and visualization of micro-agents with a high contrast-to-noise ratio [53, 54, 188]. In addition, MRI images contain anatomical details with a high contrast-to-noise ratio for precise steering of the micro-agents. However, the low image acquisition rate of MRI makes it not suitable for micro-agent applications that require real-time visualization [189]. Similar to MRI, CT provides high-resolution images of micro-agents but it has limited working space for the integration of actuation and sensing systems [190]. Fluoroscopy is an alternative imaging method for CT to obtain a larger workspace and achieve more image acquisition rate [31, 191]. Both CT and fluoroscopy have harmful effects on both clinicians and patients due to ionizing radiation exposure [56]. Among the imaging modalities, ultrasound-based techniques do not have any known side effects on health and are used for real-time visualization of the micro-agents [59, 66, 165, 192, 193]. Ultrasound imaging provides a large working space for the placement of the actuation systems since images are acquired using a small hand-held probe [62, 194, 195]. However, ultrasound images are inherently noisy and contain artifacts, which hinder the detection of micro-agents. Photoacoustic imaging overcomes the limitation in ultrasound imaging by contrast enhancement of micro-agents. The light absorption heats up micro-agents containing metallic materials, and subsequent acoustic waves are generated by thermal expansion [65]. The generated acoustic waves render that micro-agents achieve a higher signal-to-noise ratio than ultrasound imaging and are resolved from the surroundings [63, 196, 197].

Optical microscopy techniques are used for preliminary tests and micro-agents in lab-on-a-chip applications since the experimental environments are fabricated with transparent materials [61, 186]. Bright-field and single-band fluorescence microscopy techniques are widely-used for visualizing micro-agents. Full visualization of the samples is obtained with bright-field microscopy, but height differences between the micro-agents and physical surroundings cause blurring of the acquired images [198]. Single-band fluorescence microscopy provides only visualization of micro-agents with high-resolution and does not provide information about surroundings [98, 199]. In our previous study, multicolor fluorescence microscopy was introduced to overcome the limitations in optical microscopy techniques for visualizing micro-agents [198]. A wide-field multicolor microscope was

developed as a tool to collect focused images from different spectrum bands. The full samples were spectrally resolved, and occlusion-free visualization of micro-agents and surroundings was obtained.

In this study, we address the lack of real-time multicolor imaging of micro-agents and surroundings. The main difference between the imaging techniques used in previous studies and our approach is that a better understanding mechanism of functionality and dynamics of the micro-agents is established by color-coding of the full samples. Since color is an essential information carrier for human perception and cognition amplification, acquired multicolor images enable clear visualization of micro-agents and surroundings. The potential of multicolor microscopy is demonstrated by visualizing mobile micro-agents as surrogates for drug carriers in 3D tumor and vascularized environments. The primary contributions of this study (in the field of microrobotics) are (1) Demonstration of real-time multicolor fluorescence microscopy by spectral unmixing of micro-agents, organic bodies (cancer spheroids and vessels), and microfluidic channels. (2) Developing a microfluidic chip that immobilizes a single 3D cancer spheroid at a fixed location for delivery tasks with micro-agents and multicolor image acquisition from a confined environment. (3) Real-time color-coded visualization of micro-agents inside *in vitro* perfusable vascular network formed on a microfluidic system. Additionally, multiple imaging experiments are conducted using micro-agents with different geometries and sizes to show our contributions.

For imaging experiments, a tumor model is created by placing cancer spheroids formed using cervical HeLa cells in the developed microfluidic chip filled with culturing medium. *In vitro* based microfluidic vascular network and *ex ovo* based chicken chorioallantoic membrane are used as models to visualize micro-agents inside vascularized environments. Multicolor images are acquired through experiments where the micro-agents are magnetically moved inside the models. Real-time multicolor image acquisition is configured based on unambiguous color-coding as well as excitation of the fluorophores with minimal time intervals. First, spectral crosstalk disables the identification of micro-agents and surroundings from a single spectrum band and their visualization with a designated color. In order to overcome the crosstalk, emitted fluorescence photons are collected from three relatively well-separated spectrum bands for individual image formation. Second, fluorophores have a limited lifespan, and the intensity of emitted fluorescence photons decreases during imaging due to photobleaching. In order to prolong the lifespan of multicolor imaging by reducing the photodamage on the fluorophores, sequential excitation strategy is used.

The benefits of simultaneous [81, 93] and sequential [94, 200] excitation strategies for multicolor fluorescence microscopy are extensively studied using cellular structures. Simultaneous excitation of the fluorophores provides image acquisition from spectrum bands without delay. However, acquired images contain significant crosstalk that disables unambiguous detection of specific microstructures or compartments. Sequential excitation of the fluorophores and synchronous triggering of the imaging sensors (i.e., spectral multiplexing) overcome the crosstalk [119, 128]. The drawback of the sequential strategy is that spectrally resolved images are acquired with an equal delay, which limits the multicolor formation rate [201]. The models containing mobile and stationary micro-agents are fully resolved without crosstalk by sequential excitation of the fluorophores in a round-robin manner and synchronous image acquisition to the excitation sequence. Real-time visualization of the models is obtained by relatively fast spectral multiplexing.

5.2 Methods

5.2.1 Micro-Agent Fabrication using Electrospinning

Electrospinning setup for fabrication of micro-agents is constructed using a high-voltage power supply (60C24-P250-I5, Advanced Energy, USA) and a syringe pump (NE-4000, New Era Pump Systems, USA) (Fig. 5.2-(a)). A data acquisition unit (34972A, 34901A, 34907A, Keysight, USA) is used to both transfer control signals to the high-voltage power supply and collect feedback data. The setup is placed inside an air-tight enclosure to ensure reproducible fabrication by providing the same air convection condition. Polymer solution for the electrospinning consists of polystyrene pellets (430102-1KG, Sigma-Aldrich, USA) as carrier polymer, anhydrous N,N-Dimethylformamide (DMF) as solvent (227056-1L, Sigma-Aldrich, USA), coumarin 6 (442631-1G, Sigma-Aldrich, USA) as a hydrophobic fluorophore, and iron oxide nanoparticles (Fe_3O_4) (637106-25G, Sigma-Aldrich, USA) as magnetic material [46, 202]. For fabrication of continuous beaded and straight fibers, solutions with 30.02% (19.8% polystyrene, 10.0% Fe_3O_4 , 0.2% coumarin 6) and 45.25% (30.1% polystyrene, 15.0% Fe_3O_4 , 0.2% coumarin 6) weight-to-volume ratio in DMF are prepared, respectively. Fe_3O_4 and DMF are first sonicated for 30 min to disaggregate the particles. Polystyrene pellets and coumarin 6 are subsequently added to the mixture and blended using a roller mixer (LLG-uniRoller 6, LLG-Labware, Germany) for 12 hours to achieve a homogeneous solution. For the electrospinning process, the polymer solution is placed in a plastic syringe and connected through a Teflon tubing to an 18-gauge blunt-tip needle (TS18SS-15, Adhesive Dispensing Ltd., UK). Accelerating voltage, solution feed rate, and tip-to-collector distance are set as 14 kV, 2.5 mL/h, and 16 cm, respectively. 0.04 mL polymer solution is electrospun at once, and fiber meshes are deposited on a grounded aluminum foil at 24°C and 22% humidity. The solvent residue on the electrospun fibers is removed by drying at room temperature for 12 hours. Fig. 5.2-(b1) and (b2) show the morphologies of the fiber meshes imaged with scanning electron microscopy (JSM-7200F, JEOL, Japan). Deposited fiber meshes are cut into 2-3 mm pieces using a scalpel and then immersed into a glass vial containing 1% (volume/volume) Tween 80 (P4780-100ML, Sigma-Aldrich, USA) in Milli-Q water. Fluorescent and magnetic micro-agents are obtained by cutting the fibers using a sonicator (2510, Branson, USA) for 2 hours (Fig. 5.2-(c1)). The polymer grinding process using sonication randomly shortens the continuous fibers to obtain micro-agents. The electrospinning setup is also designed for depositing the fibers on the collector with random orientation. This fabrication technique is selected to enable the validation of multicolor image acquisition using micro-agents with random size distribution. In order to obtain micro-agents with desired sizes, synthesized fibers can be aligned with a drum collector and cut using a laser [203]. Additionally, the electrospaying process ensures the fabrication of bead-shaped micro-agents with narrow size distribution. The setup is able to be used for electrospaying without any modification [204]. Fig. 5.2-(c2) shows fluorescence images of the fabricated micro-agents. The surface profile of a micro-agent characterized using confocal microscopy (S Neox, Sensofar, Spain) is shown in Fig. 5.2-(c3). In order to determine optimal excitation and emission wavelength ranges for fluorescence microscopy, the spectrum of the micro-agents is characterized using a spectrofluorometer (FP-8300, Jasco, Japan).

5.2.2 Spectrum Analysis

The solution for the spectrum analysis is prepared by dissolving 2.11 mg coumarin 6 in 5 ml DMF. 10 μl solution is diluted with 690 μl DMF in a quartz cuvette (CV10Q700F,

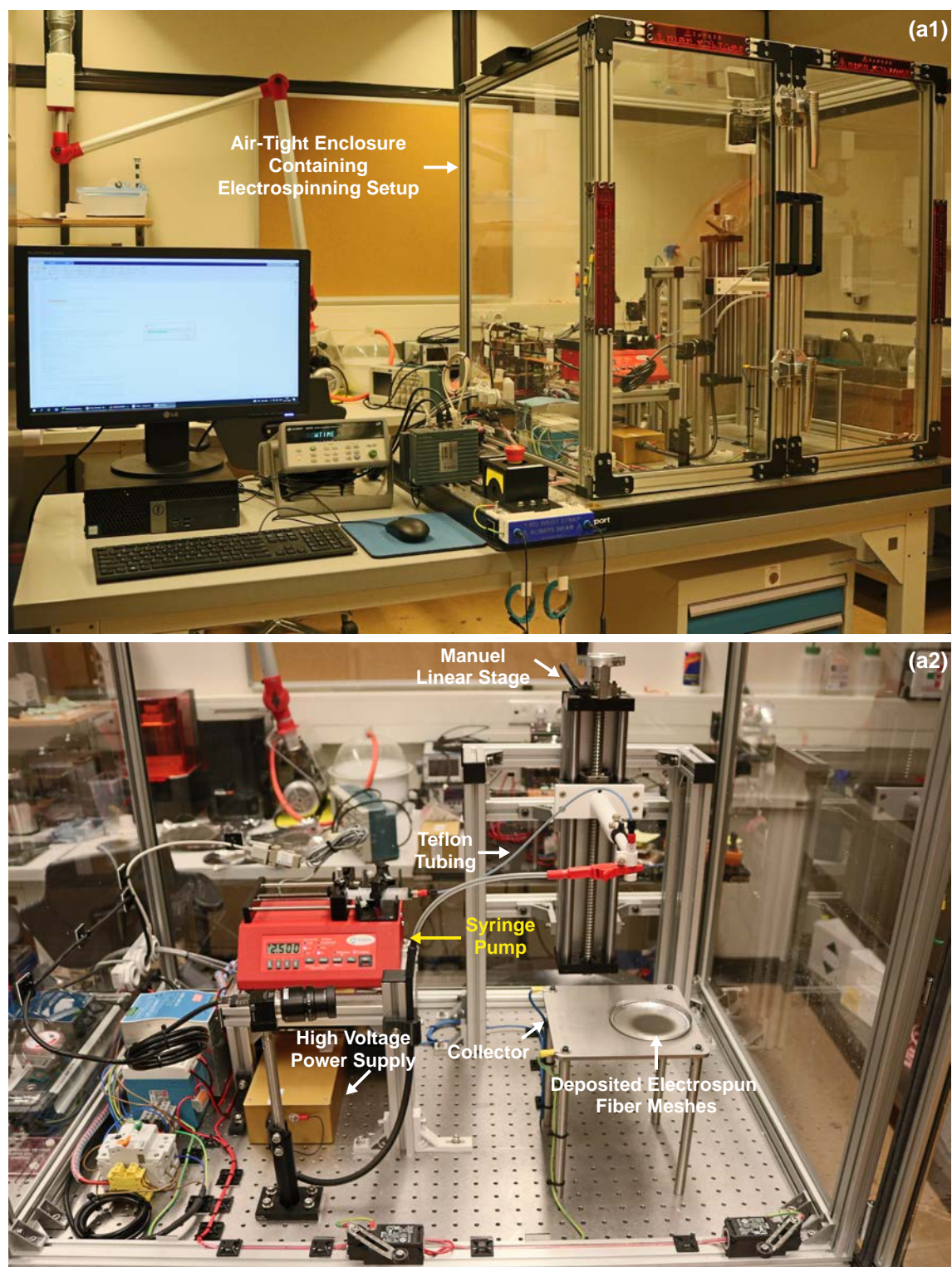


Figure 5.1: Overview of the electrospinning setup used for fabricating fluorescent and magnetic micro-agents. (a1) Control unit and electrospinning chamber. (a2) A detail of electrospinning system configuration.

Thorlabs, USA) for the measurement. Ultraviolet-visible excitation and emission spectra, the wavelength range between 200 nm and 900 nm, is measured using 2D spectrum analysis (Fig. 5.2-(d1)). Peak excitation and emission wavelengths for coumarin 6 in DMF are

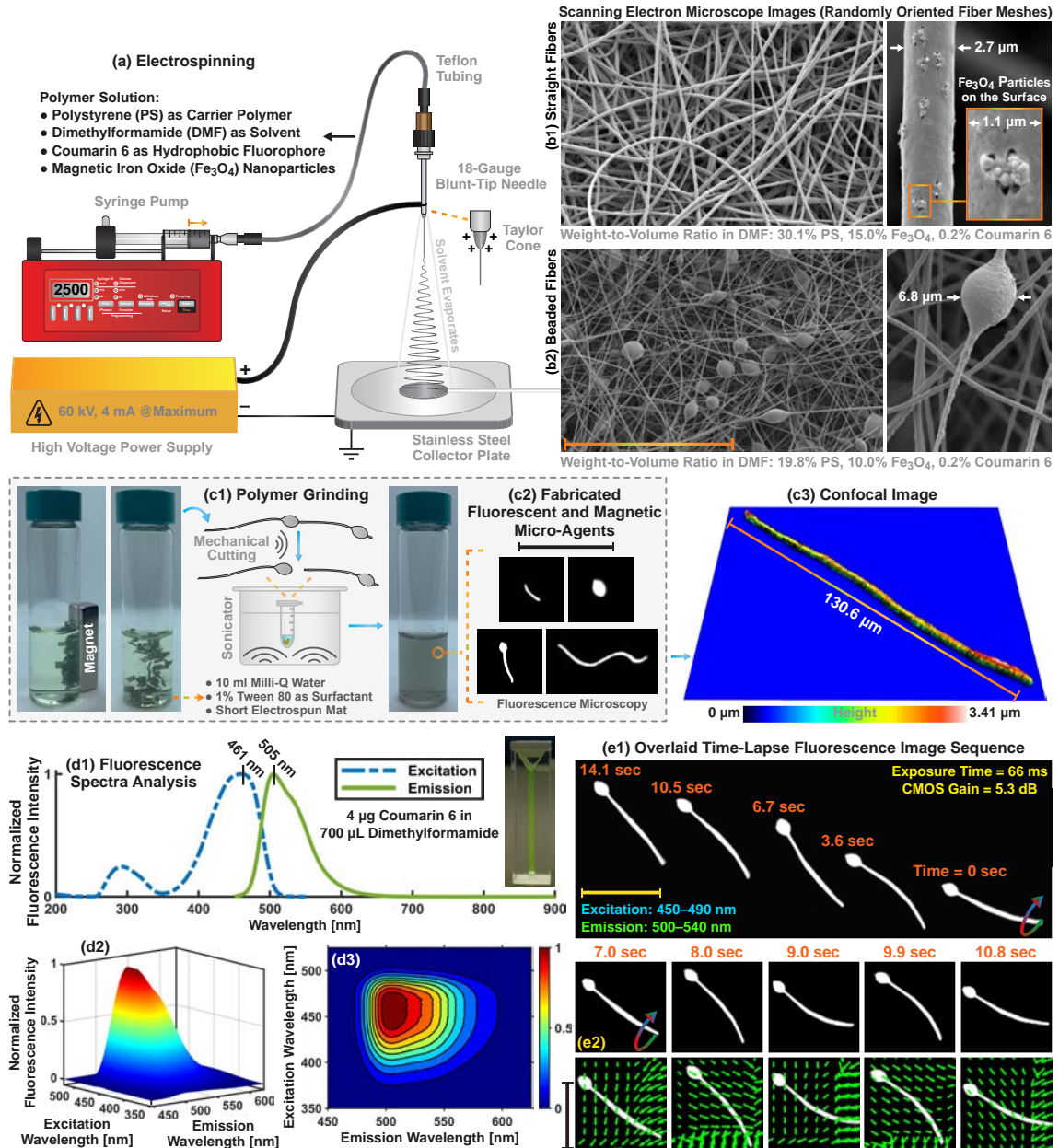


Figure 5.2: General overview for fluorescent and magnetic micro-agent fabrication using electrospinning. (a) Schematic representation of the electrospinning setup and content of the polymer solution. (b1) and (b2) Scanning electron microscope images of the deposited straight and beaded fiber meshes on the collector using electrospinning, respectively. (c1) Polymer grinding process for obtaining micro-agents by cutting the continuous fibers using a sonicator. (c2) Fluorescence images of the fabricated micro-agents. (c3) 3D surface profile of the micro-agent visualized using confocal microscopy. (d1) Ultraviolet-visible spectrum analysis of coumarin-6 in dimethylformamide (DMF). (d2) and (d3) Spectrum analysis of coumarin-6 in DMF at varying excitation and emission wavelengths. (e1) Fluorescence microscopy for visualizing micro-agent movement with a magnetic field of 21 mT. (e2) The vector fields overlaid on the fluorescence images show the motion of the micro-agents analyzed using Lucas-Kanade optical flow. Scale bar: 100 μm .

measured as 461 nm and 505 nm, respectively. 3D spectrum analysis is performed to measure emission spectrum at varying excitation wavelengths. The solution is excited between 350 nm and 500 nm with a 1 nm increment and emitted fluorescent photons are collected in the wavelength range of 450 nm and 600 nm (Fig. 5.2-(d2) and (d3)).

Our measurement shows that fluorescence photons with maximum intensity are collected when the excitation and emission are performed with 436–477 nm and 497–518 nm spectrum bands, respectively. According to the spectrum analysis, 450–490 nm and 500–540 nm bands are selected to excite coumarin 6 and collect emitted fluorescent photons for visualization of the fabricated micro-agents, respectively. Fig. 5.2-(e1) shows an example of single-band fluorescence microscopy for magnetic movement of a micro-agent. Multicolor microscopy is performed to visualize the micro-agents in a tumor environment containing HeLa cell spheroids with a diameter of 200 μm .

5.2.3 HeLa Cell Spheroids Formation

HeLa cells are cultured in Dulbecco's modified Eagle's medium (11-965-092, Fisher Scientific Ltd. Canada), supplemented with 10% fetal bovine serum (F7524-500ML, Sigma-Aldrich, USA), and 1% (volume/volume) penicillin-streptomycin (15-140-122, Thermo Fisher Scientific Inc., USA) [198]. Cells in 2D are cultured and passaged at 80% confluence and medium change is performed every 48 hours. For the formation of 3D cancer spheroids, cells are trypsinized, resuspended to a density of 2×10^6 cell/ml, and seeded in 3% (weight/volume) agarose (16500500, ultra-pure agarose, Invitrogen, USA) microwell arrays resulting in average 267 cells per spheroid. Half medium change is done daily. At day 3, spheroids are collected and stained with 10 μM CellTracker Red CMTPX (C34552, Thermo Fisher Scientific Inc., USA) by 45 minutes incubation in a serum-free medium and washed twice with cell culture medium. Both 2D and 3D cultures are done in a humidified atmosphere with 5% carbon dioxide at 37°C. For long-term storage, 3D spheroids stained with CMTPX are fixated at room temperature with 4% formaldehyde (F8775-25ML, Sigma-Aldrich, USA) for 15 minutes and then washed twice with Dulbecco's phosphate-buffered saline (DPBS). For imaging experiments, the spheroids are immobilized and maintained using the developed microfluidic chip.

5.2.4 Microfluidic Chip Fabrication

The standard soft-lithography method is used to fabricate negative mold of the chips with the height of 187 μm using SU-8 photoresist [132]. The salinization process is performed for easy removal of the polydimethylsiloxane (PDMS) layer by improving the surface hydrophilicity of the mold. Degassed 10:1 PDMS and curing agent (Sylgard 184 Silicon Elastomer Kit, Dow Corning, USA) mixture is poured over the mold and cured at 70°C in the oven for 12 hours. After the cured PDMS layer is removed, inlet and outlet ports are punched. The chip fabrication is completed by bonding the PDMS layer on a microscope glass using plasma oxidation. The bonding strength is improved by baking the chip on a hot plate at 70°C for 4 hours. A single cell spheroid is first transferred into the chip and immobilized by an air bubble injection. Micro-agents are mixed with 250 $\mu\text{g/ml}$ indocyanine green (I2633-25MG, Sigma-Aldrich, USA) in the culture medium and subsequently injected into the chip by pipetting. Thus, a 3D tumor model is created for multicolor image acquisition (Fig. 5.9-(a3)). In order to show that multicolor microscopy provides spectrally resolved images for the micro-agents in vascularized models, a perfusable vascular network is formed on a microfluidic channel.

5.2.5 3D Co-Culture in a Microfluidic System for *In Vitro* Vascularization

Red fluorescence protein - human umbilical vein endothelial cells (RFP-HUVECs) (cAP-0001, Angio-Proteomie, USA) are cultured in 2D with endothelial cell growth medium-2 (EGM-2 medium) (Endothelial Cell Growth Medium 2 Kit, C-22111, Promo Cell, USA)

with 1% (volume/volume) (v/v) penicillin-streptomycin. In parallel, mesenchymal stem cells (PT-2501, Lonza, USA) are cultivated in 2D in minimum essential medium eagle - alpha modification (22571020, Thermo Fisher Scientific, USA) supplemented with 10% (v/v) fetal bovine serum (F7524v, Sigma-Aldrich, USA), 2 mM l-glutamine (35050061, Thermo Fisher Scientific, USA), 0.2 mM ascorbic acid (A8960-5G, Sigma Aldrich, USA), 1% (v/v) penicillin-streptomycin (15-140-122, Thermo Fisher Scientific, USA) and 1 ng/ml fibroblast growth factor-basic (PHG0261, Thermo Fisher Scientific, USA). Both cell types are cultured in a humidified atmosphere with 5% carbon dioxide at 37°C and are used between passages 4 and 6. The cells are cultured till 80% confluency prior to detachment and mixed in a concentration of 10×10^6 cells/mL (1 to 1 ratio) in a fibrin hydrogel in a final concentration of 3 mg/mL (Fibrinogen, 0215112201, MP Biomedicals, USA) and 3 U of thrombin (0215416301, MP Biomedicals, USA). The cell-matrix mixture is injected into the hydrogel chamber of the gel loading port of the microfluidic system and is allowed to polymerize in the incubator at 37°C for 15 minutes. Before, the microfluidic surface area is functionalized to promote strong hydrogel interaction with the PDMS and glass by incubating the microfluidic chip after plasma oxidation bonding for 4 hours with poly-D-lysine hydrobromide (P1024-10MG, Sigma-Aldrich, USA) with following washing steps with sterile Milli-Q water. After hydrogel polymerization, the gel loading ports are blocked with stripes of standard PCR plate sealing foil to avoid fluidic leakages and the flow channels next to the hydrogel channel are filled with EGM-2 medium. The pressure drop of 5 Pa to create the mechanical stimuli for the *in vitro* vascularization is established by connecting two syringe pumps (AL-1600, New Era Pump Systems, USA) on vertically opposite sides. An overview of the microfluidic system for *in vitro* vascularization creation is illustrated in Fig. 5.3. The inlet port is used to inject the EGM-2 medium and the outlet port to pull it out while the fluidic ports are blocked with PDMS after the initial filling. By applying pre-determined flow rates with EGM-2 medium by flow studies performed using COMSOL Multiphysics (version 5.5, COMSOL AB, Sweden). The pressure drop is maintained for 7 days before the experiments. For multicolor microscopy, 250 $\mu\text{g/ml}$ indocyanine green in the cell culture medium and micro-agents are injected in the microfluidic system. Fig. 5.10-(a1) shows the micro-agents in the engineered vascular network. In order to visualize micro-agents in natural vessels, *ex ovo* chicken chorioallantoic membrane is used as a testbed.

5.2.6 Chicken Vasculature

White Leghorn chick embryos are incubated at 38°C and 65% humidity throughout the culturing process. At day 10, the egg contents are cracked into 60 mm cell culture Petri dishes [205]. Egg albumin and yolk contents are removed using viscous liquid handling pipettes. The vasculature is washed three times using ice-cold DPBS (14190250, Thermo Fisher Scientific, USA) solution and then fixated in 4% paraformaldehyde (1004965000, Sigma-Aldrich, USA) overnight at 4°C for long-term storage. This is followed by incubation with 0.3% Triton X-100 (T8787-250ML, Sigma-Aldrich, USA) in DPBS for 30 minutes and washing three times using ice-cold PBS solution. For multicolor microscopy, the vasculature is first decellularized (erythrocytes removed) and subsequently stained with Rhodamine B (K94900-25, Labshop, the Netherlands) and indocyanine green.

5.2.7 Multicolor Fluorescence Microscopy and Magnetic Movement

Real-time widefield multicolor microscopy is performed by excitation of the fluorophores from three-different spectrum bands in a round-robin manner [198]. The emitted fluores-

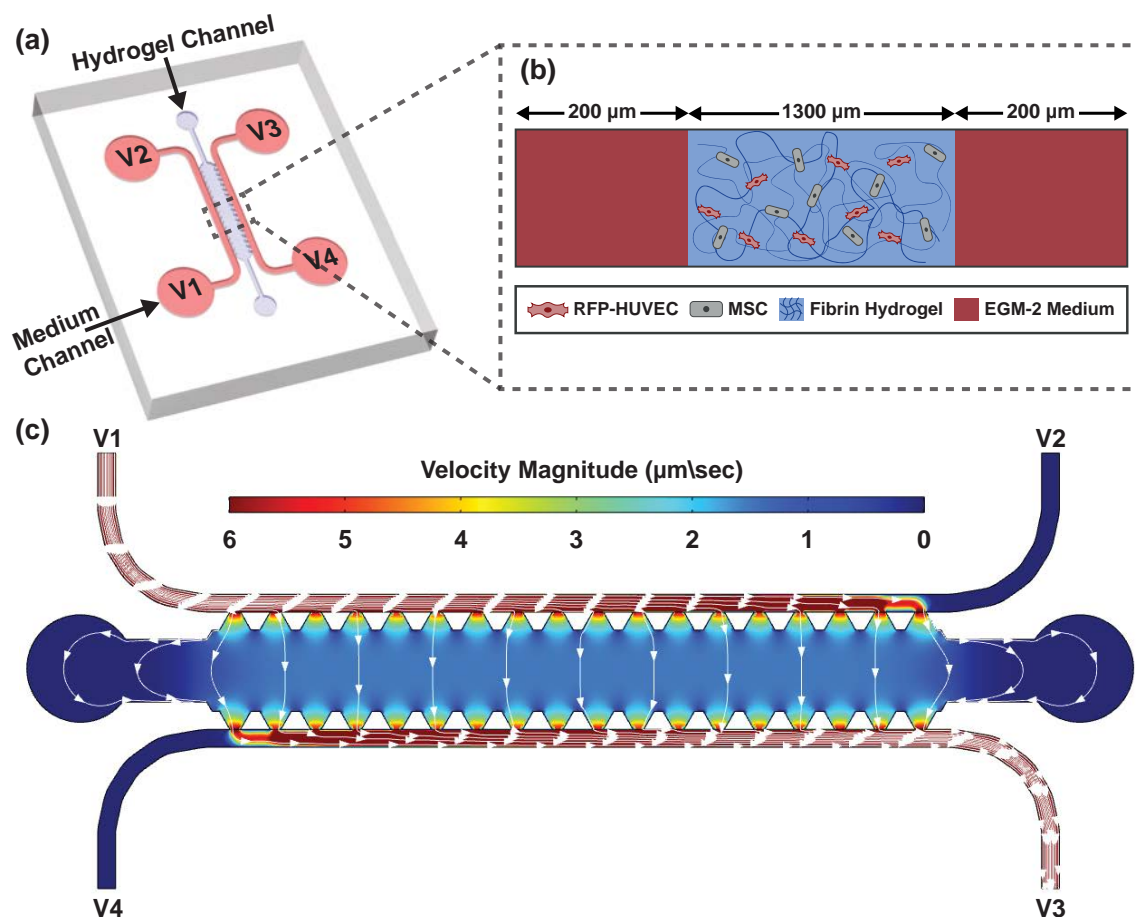


Figure 5.3: General overview of the microfluidic system to create an *in vitro* vascularization for multicolor imaging experiments. (a) The schematic representation of the microfluidic system illustrates the hydrogel filling ports and the different flow channel access points. The hydrogel channel is filled with a fibrin hydrogel with co-cultured red fluorescence protein - human umbilical vein endothelial cells (RFP-HUVECs) and mesenchymal stem cells (MSC) (b) and perfused with endothelial cell growth medium-2 (EGM-2 medium) for 7 days under constant interstitial flow. (c) Velocity heat map of the flow simulation using COMSOL Multiphysics (version 5.5, COMSOL AB, Sweden) for displaying the uniform interstitial flow across the fibrin hydrogel for stimulating the vascular formation of the embedded co-culture cells.

cence light is synchronously collected to acquire 8-bit grayscale individual images with 1280×1024 pixels. 10x and 5x long working distance objectives (Plan Apo, Mitutoyo, Japan) are used to focus the excitation light on the samples and collect the emitted fluorescent photons, respectively. Coumarin 6 and indocyanine green are excited from 450–490 nm and 750–800 nm spectrum bands, respectively. The emitted light is collected from 500–540 nm for coumarin 6 and 817.5–875.5 nm for indocyanine green, respectively. CMTPIX, RFP-HUVECs, and Rhodamine B are excited from the 554.5–589.5 nm band, and the emitted light is collected in the wavelength range of 592.5–667.5 nm. The intensity values in the individual images acquired from 500–540 nm, 592.5–667.5 nm, and 817.5–875.5 nm spectrum bands are represented using black-green, black-red, black-blue color maps, respectively (Fig. 5.8-(a4), Fig. 5.10-(b), Fig. 5.11-(a4)). Multicolor images are formed by overlapping the color-converted individual images acquired in one round. An orthogonal array of four iron-core electromagnetic coils with a cut-off frequency of 110 Hz is placed in the microscope's working space to move the micro-agents using the rotational field (Fig. 5.4 and Fig. 5.9-(d)). For heat dissipation, the coil array is mounted

on an aluminum holder using tapered collars. The coils are covered with copper tape for heat transfer enhancement and electrical isolation. Switchable amplifiers supplied with a dc power supply (EA-PS 5040-20A, EA Elektro-Automatik, Germany) are used to power the coils [206]. A signal generator (4050B, BK Precision, USA) is used to generate reference signals for the rotating field frequency. The signals are distributed to a corresponding coil driver using a demultiplexer interface (74HC4052, Texas Instruments, USA) by falling edge detection using a microcontroller. The maximum magnetic field produced by the coil array is measured as 30 mT using a teslameter (3MH3A, Senis AG, Switzerland). The magnetic pulling force is generated using two neodymium-iron-boron permanent magnets (S-45-30-N, Supermagnete, Germany). The maximum magnetic field and gradient generated by the magnets are measured as 120 mT and 5 T/m, respectively.

5.2.8 Ethics Statement

According to the Dutch animal care guidelines, IACUC approval for chicken embryo experimentation is not necessary unless hatching is expected. Moreover, only experiments with chick embryos of development EDD14 and older need IACUC approval. The embryos used in this study were all in the early stages of embryo development (EDD10). Fertilized chicken eggs used in this study were purchased from approved poultry egg farms in the Netherlands. RFP-HUVECs culture studies were approved by Dutch Ministry and experiments were performed under ML-1 laboratory environment, followed by the university policies and standard protocol.

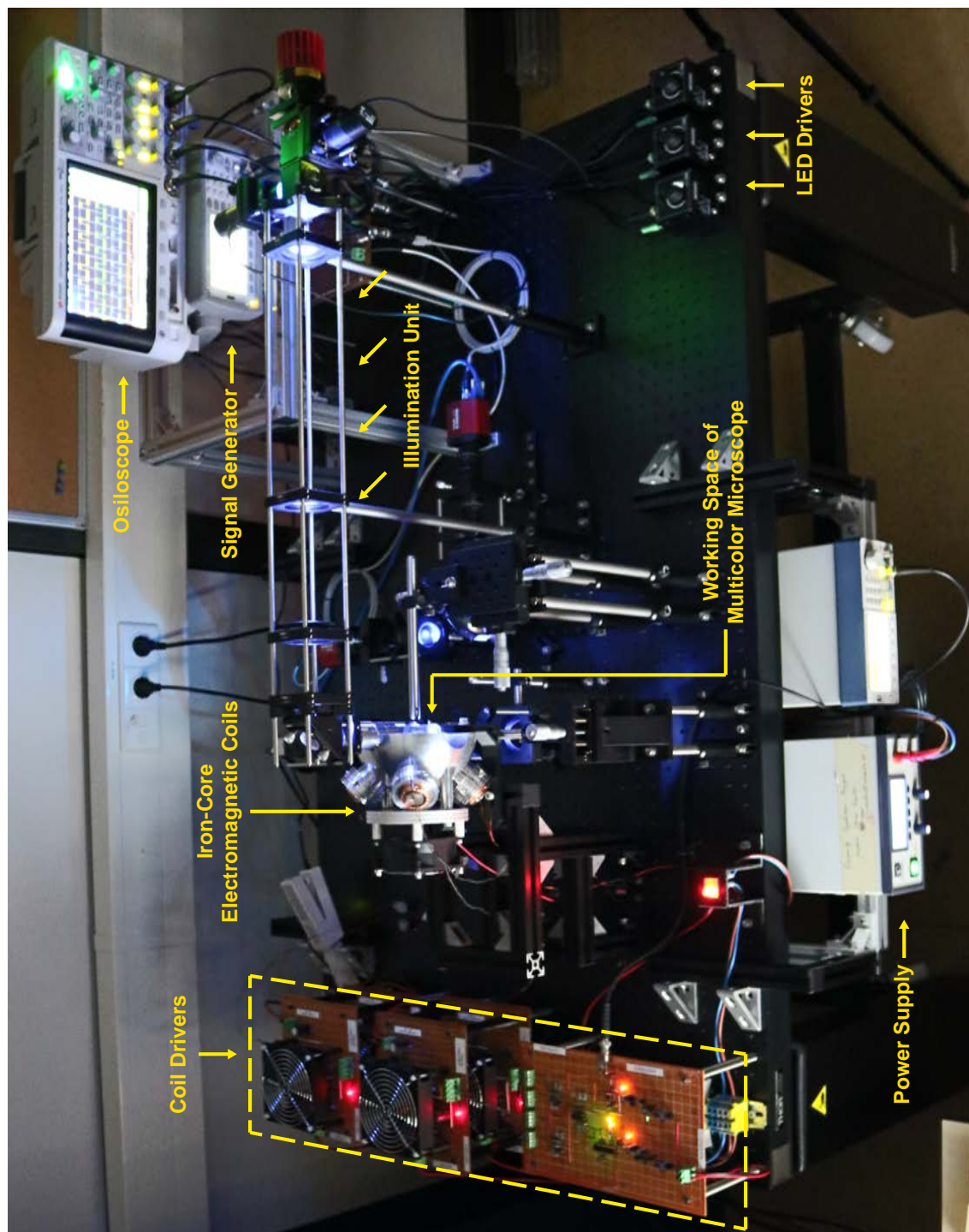


Figure 5.4: Microscope coupled with iron-core coils to acquire real-time multicolor fluorescent images containing mobile micro-agents and dynamic surroundings.

5.3 Results

5.3.1 Single-Band Fluorescence Microscopy

Our micro-agents are fabricated by grinding the continuous beaded and straight fibers synthesized using electrospinning (Fig. 5.2). The synthesized fibers consist of polystyrene as a carrier polymer and iron oxide nanoparticles (Fe_3O_4) as a magnetic material (Fig. 5.2-(b)). Coumarin 6 is selected to stain the fibers since it is immobilized in a polystyrene matrix and insoluble in water. Additionally, coumarin 6 has a relatively high photobleaching resistance. The grinding process breaks the fibers into fragments using ultrasound waves. This enables obtaining magnetic and fluorescent micro-agents ranging in size from $4\ \mu\text{m}$ to $131\ \mu\text{m}$ (Fig. 5.2-(c1) and (c2)). Single-band fluorescence microscopy is performed to visualize the motion and electrostatic interaction of the fabricated micro-agents in Milli-Q water. Fig. 5.5-(a) shows the pulling motion of two micro-agents fabricated using straight fibers. Fig. 5.5-(b) demonstrates the dynamic movement of a micro-agent fabricated using beaded fibers. During the imaging experiments, we observe that micro-agents fabricated using straight fibers are fully loaded with Fe_3O_4 and rigid. On the other hand, the polymer solution prepared for beaded fiber synthesis allows the fabrication of flexible micro-agents since the distribution of Fe_3O_4 is random. Fig. 5.5-(c1), (c2), (c3) and Fig. 5.5-(d1), (d2) show diagonal and vertical motion of a flexible micro-agent using an oscillating magnetic field, respectively. Electrostatic interaction between micro-agents is visualized using three experiments. The first experiment is conducted to visualize the behavior of micro-agents in a rotating field. We observe that micro-agents fabricated using both beaded and straight fibers aggregate owing to dipole-dipole interaction and form a cluster over time. Fig. 5.5-(e) demonstrates a representative case for a micro-agent cluster formation with a 16 mT rotating field at 8 Hz. The second experiment is devised to visualize the attachment of two micro-agents utilizing electrostatic forces. Fig. 5.5-(f1) shows acquired time-lapse images by highlighting the attachment (self-assembly). The motion of the attached micro-agents is represented as vector fields using Lucas-Kanade optical flow and shown in Fig. 5.5-(f2) [141]. Our results show that the attached micro-agents move together, and electrostatic forces prevent disaggregation. In the third experiment, the behavior of the micro-agents is observed when no magnetic field is applied. Acquired images reveal that micro-agents fabricated using straight fibers sink and create a line-shaped self-organization pattern in both an open reservoir and a microfluidic channel (Fig. 5.5-(g1) and (g2)). The self-organization pattern is not observed when the experiment is repeated with the micro-agents fabricated using beaded fibers. A decrease in the magnetic material concentration in the micro-agents disables the self-organization behavior. The fabricated micro-agents are used as surrogates for drug carriers and attached to HeLa cell spheroids.

5.3.2 Attachment of micro-agents to HeLa cell spheroids

We visualize single and multiple micro-agents attachment to HeLa cell spheroids with three experiments in an open reservoir containing indocyanine green in the culturing medium. In all experiments, multicolor images are formed at 15 fps, and micro-agents are steered towards the spheroids with a magnetic field intensity of 36 mT. In the first two experiments, micro-agents with sharp tips are attached by puncturing the spheroids (Fig.5.6-(a1) and (b1)). In the third experiment, three micro-agents are consecutively attached to the spheroid. The first two micro-agents are adhered to the spheroid surface by electrostatic interaction, whereas the third micro-agent is attached by puncturing (Fig.5.6-(c1)). The attachments are verified by screening long-term changes using dynamic imaging.

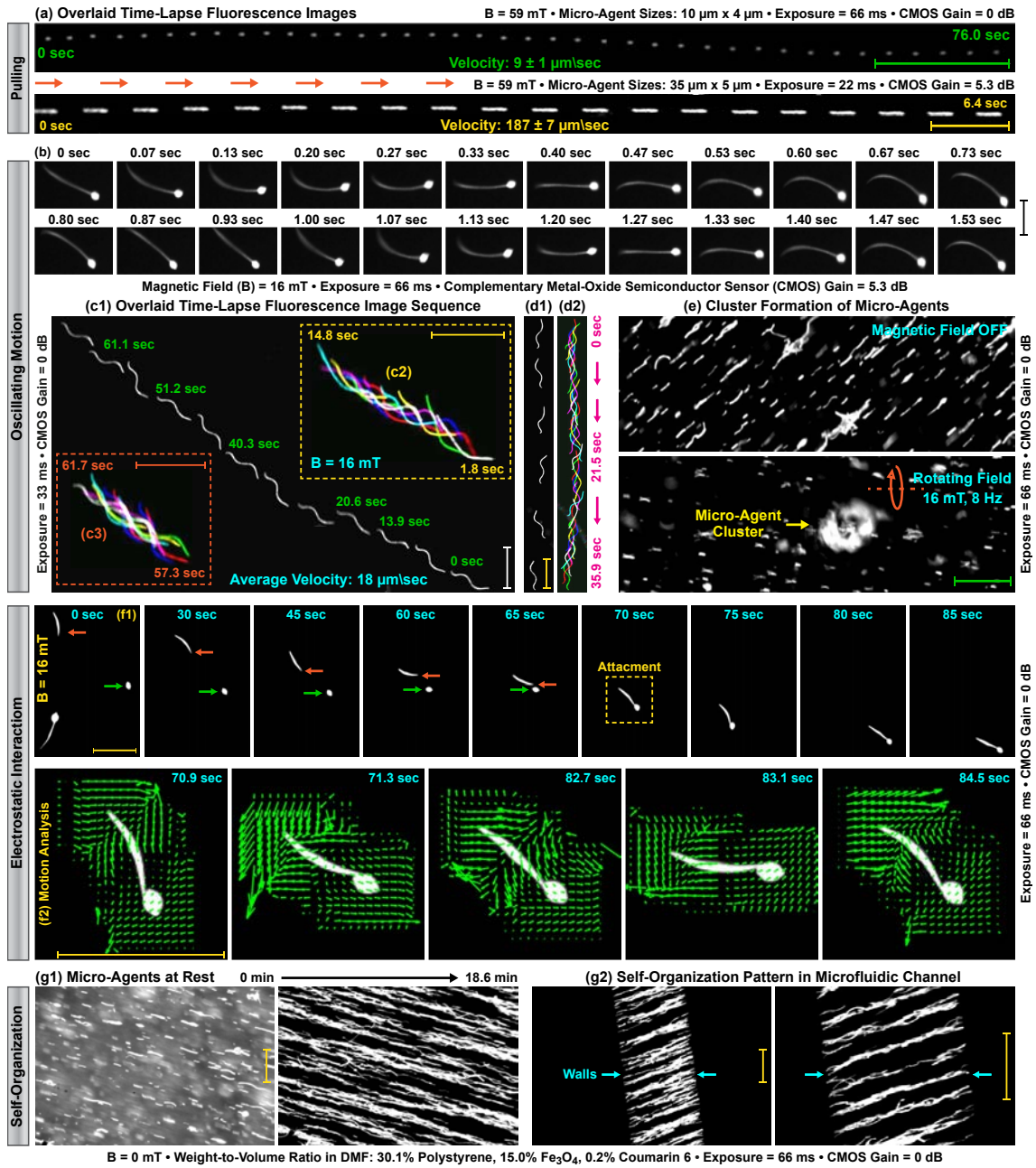


Figure 5.5: Single-band fluorescence microscopy for visualizing magnetic micro-agents labeled with coumarin 6. (a) Time-lapse image shows forward motion of the micro-agents by magnetic pulling. (b) Snapshot sequence demonstrates the oscillating motion of the micro-agent. (c1) and (d1) Overlaid fluorescence images show the diagonal and vertical movement of the micro-agents, respectively. (c2), (c3), and (d2) Oscillating motion patterns of the micro-agents. (e) Aggregation of the micro-agents by a rotating magnetic field. (f1) Attachment of the micro-agents by electrostatic interaction. (f2) Vector field expresses the motion of the attached micro-agents analyzed using Lucas-Kanade optical flow. (g1) and (g2) Self-organization of the micro-agents in a reservoir and a microfluidic channel, respectively. Scale bar: $100 \mu\text{m}$.

Excitation light generates a heat gradient between the illuminated and non-illuminated areas, which results in a flow. We visualize the mobility of the micro-agents in the flow as a passive method for attachment verification. The effect of the flow on both attached and non-attached micro-agents for 92 minutes is displayed in Fig. 5.6-(a2). Although the

velocity of the attached micro-agent is measured approximately $0 \mu\text{m}/\text{sec}$, non-attached micro-agents are mobilized by the flow. We also observe that a non-attached micro-agent moved by the flow aggregates with the attached micro-agent utilizing electrostatic forces (Fig. 5.6-(a3)). The displacement of the aggregated micro-agents is measured $0 \mu\text{m}$ for 92 minutes. Our experiment validates that attachment to the spheroid increases the inertia of the micro-agents and immobilizes them in the flow. In all experiments, the attachments are verified by visualizing the micro-agents immobility in the flow for more than 90 minutes (Fig. 5.6-(a2)-(c2)). Acquired dynamic images for the verification also reveal that the attached micro-agents displace along with the spheroids owing to the evaporation of the medium inside the reservoir by the generated heat (Fig. 5.6-(a3), (b2), and (c2)). After the complete evaporation of the medium, the displacements are measured $20 \mu\text{m}$ and $68 \mu\text{m}$ for the spheroids to which single and multiple micro-agents are attached, respectively. In order to confirm that the evaporation does not affect the attachment, a micro-agent is rotationally moved around its inserted part into the spheroid with a magnetic field of 14 mT for two minutes (Fig. 5.6-(b3)). The maximum velocity for the distal end of the micro-agent is measured as 1.4 body-length/sec ($180 \mu\text{m}/\text{sec}$). No detachment of the micro-agent from the spheroid is observed. Our results display that multicolor microscopy generates color-coded images in real-time for visualizing and verifying the attachment of micro-agents to the spheroids.

5.3.3 Translation and Rotation of Cell Spheroids by Micro-Agents Attachment

Real-time multicolor fluorescence microscopy is performed by sequential excitation of the fluorophores in a round-robin manner and synchronous individual image acquisition from 500–540 nm, 592.5–667.5 nm, and 817.5–875.5 nm spectrum bands. Individual images of the micro-agents labeled with coumarin 6 are acquired from the 500–540 nm spectrum band. The spheroids are stained with CMTPX and indocyanine green to render their visualization in 592.5–667.5 nm and 817.5–875.5 nm spectrum bands, respectively (Fig. 5.8-(a4)). Thus, the simultaneous motion of the spheroids and micro-agents is able to be visualized from all the spectrum bands used in multicolor microscopy. Our micro-agents are able to mobilize HeLa cell spheroids by an external magnetic field. Fig. 5.7-(a) shows a spheroid propelled by attached multiple micro-agents in the reservoir containing indocyanine green in the culturing medium with a magnetic field of 60 mT. Fig. 5.7-(b) demonstrates the clockwise rotation of a spheroid due to imbalances in the micro-agents attachment during the propulsion. We mobilize the spheroids with micro-agents to report the performance of the real-time multicolor microscopy. The open reservoir is used as an experimental testbed since it allows translational and rotational mobility of the spheroids by micro-agents attachment. Multicolor images are formed at 15 fps, where the individual image acquisition rate is 45 fps. Fig. 5.7-(c1) and (d1) show the forward motion of two and multiple spheroids propelled by micro-agents with a magnetic field of 120 mT, respectively. Fig. 5.7-(e1) demonstrates a representative case for steering a spheroid with propulsion of the micro-agents by changing the magnetic field direction. Path information obtained by visual tracking shows the translational motions of the spheroids up to $218 \mu\text{m}/\text{sec}$ (≈ 1.3 body-length/sec) in Fig. 5.7-(c2), (d2), and (e2) [207]. In order to visualize the rotational mobility, a spheroid is moved clockwise by a single micro-agent attachment with a maximum magnetic field of 36 mT (Fig. 5.8-(a1) and (a4)). The motion information of the spheroid with micro-agent is represented as vector fields using Lucas-Kanade optical flow and shown in Fig. 5.8-(a2). The vector fields and path of the attached micro-agent display that the spheroid is rotated around its axis with a maximum angular velocity of 1.2 rad/sec

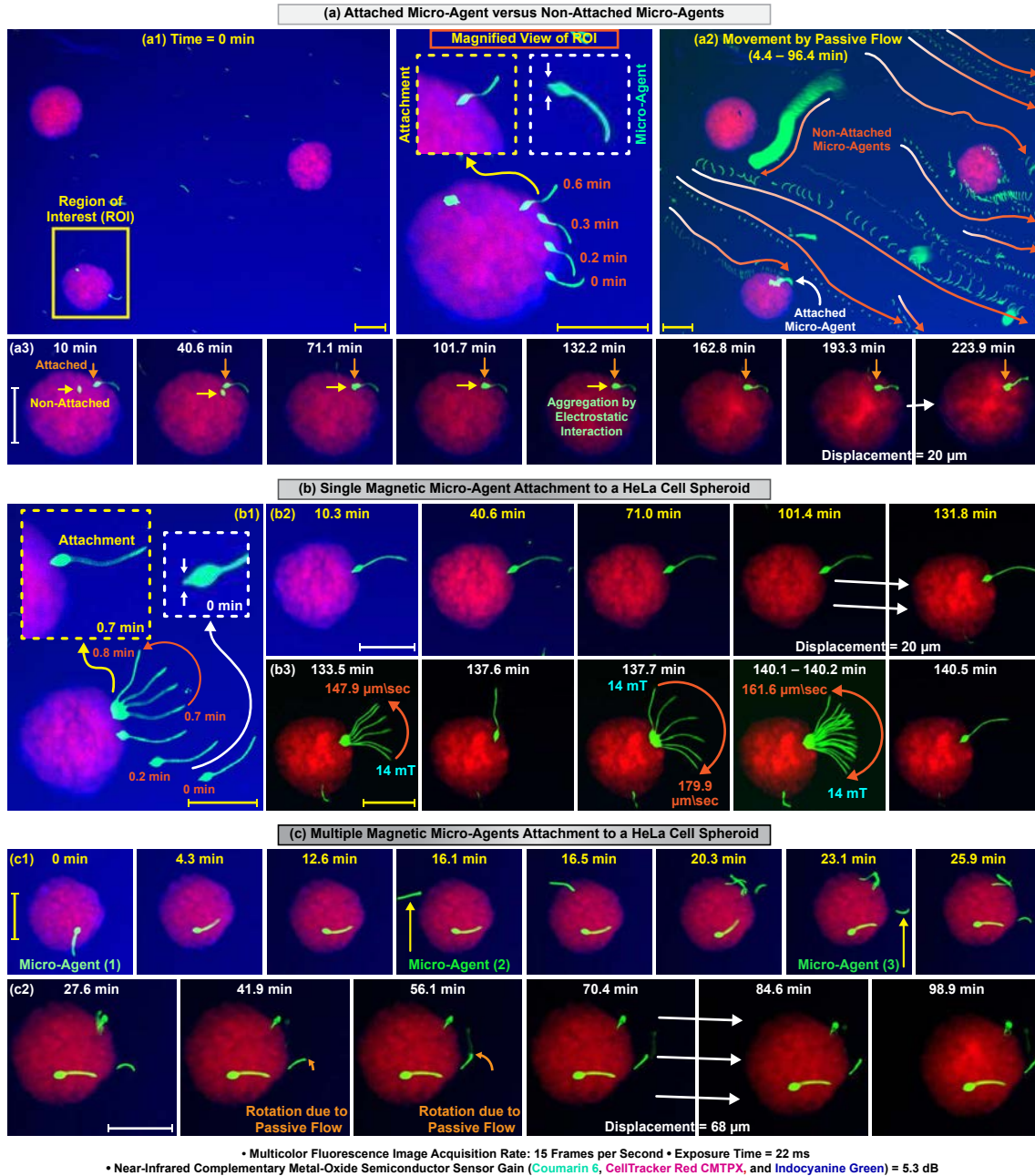


Figure 5.6: Time-lapse multicolor fluorescence microscopy for single and multiple magnetic micro-agents attachment to HeLa cell spheroids. (a1)-(c1) Attachment of micro-agents to HeLa cell spheroids with a magnetic field of 36 mT. (a2) and (a3) Effect of passive flow on the attached and non-attached micro-agents. (b2) and (c2) Visualization of the changes in the micro-agents attached to the spheroids. (b3) Attachment check by rotational movement of the micro-agent around its inserted part into the spheroid after two hours pass. Scale bar: 100 μm .

(Fig. 5.8-(a3)). Rotational and translational mobility is visualized together by actuating two spheroids adhered with a micro-agent cluster in a 16 mT rotating magnetic field at 1 Hz (Fig. 5.8-(b1)). Fig. 5.8-(b2) demonstrates the motion field for the rotation of the two spheroids with the micro-agent cluster. The translational motion of the spheroids is plotted in Fig. 5.8-(b3). Our experiments show that multicolor microscopy renders visualizing the simultaneous motion of multiple spheroids and micro-agents in time-varying magnetic

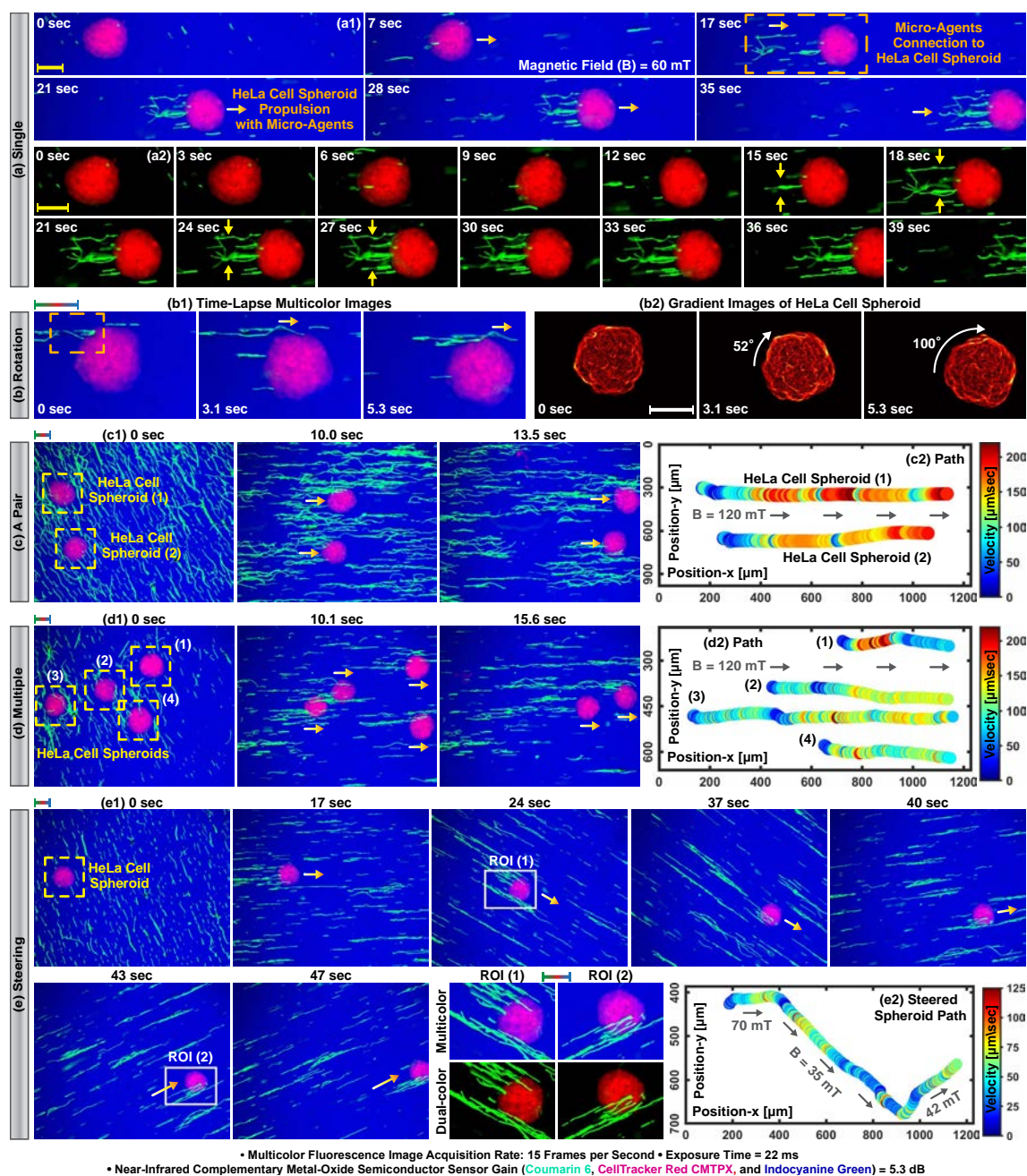


Figure 5.7: Translation of HeLa cell spheroids by magnetic micro-agents in a reservoir filled with culturing medium and indocyanine green. (a1) Propelling a single spheroid by micro-agents connection. (a2) Time-lapse dual-color microscopy for connection of micro-agents to the spheroid. (b1) Rotation of a spheroid caused by micro-agents propelling. (b2) Demonstration of the spheroid rotation by gradient images. (c1) and (d1) Simultaneous translation of two and multiple spheroids by micro-agents, respectively. (e1) Steering a spheroid propelled with micro-agents by changing the magnetic field direction. (c2)-(e2) Path and velocity information of the spheroids in (c1)-(e1), respectively. Scale bar: 100 μm .

fields up to a translational velocity of 504 $\mu\text{m}/\text{sec}$ (≈ 3.4 body-length/sec for a spheroid) at 15 fps. We also validate that spheroids as an organic body are able to be actuated by single, multiple, and a cluster of micro-agents in a reservoir environment. In order to immobilize a single spheroid for the attachment of micro-agents and provide a confined environment for multicolor microscopy, a microfluidic chip is developed.

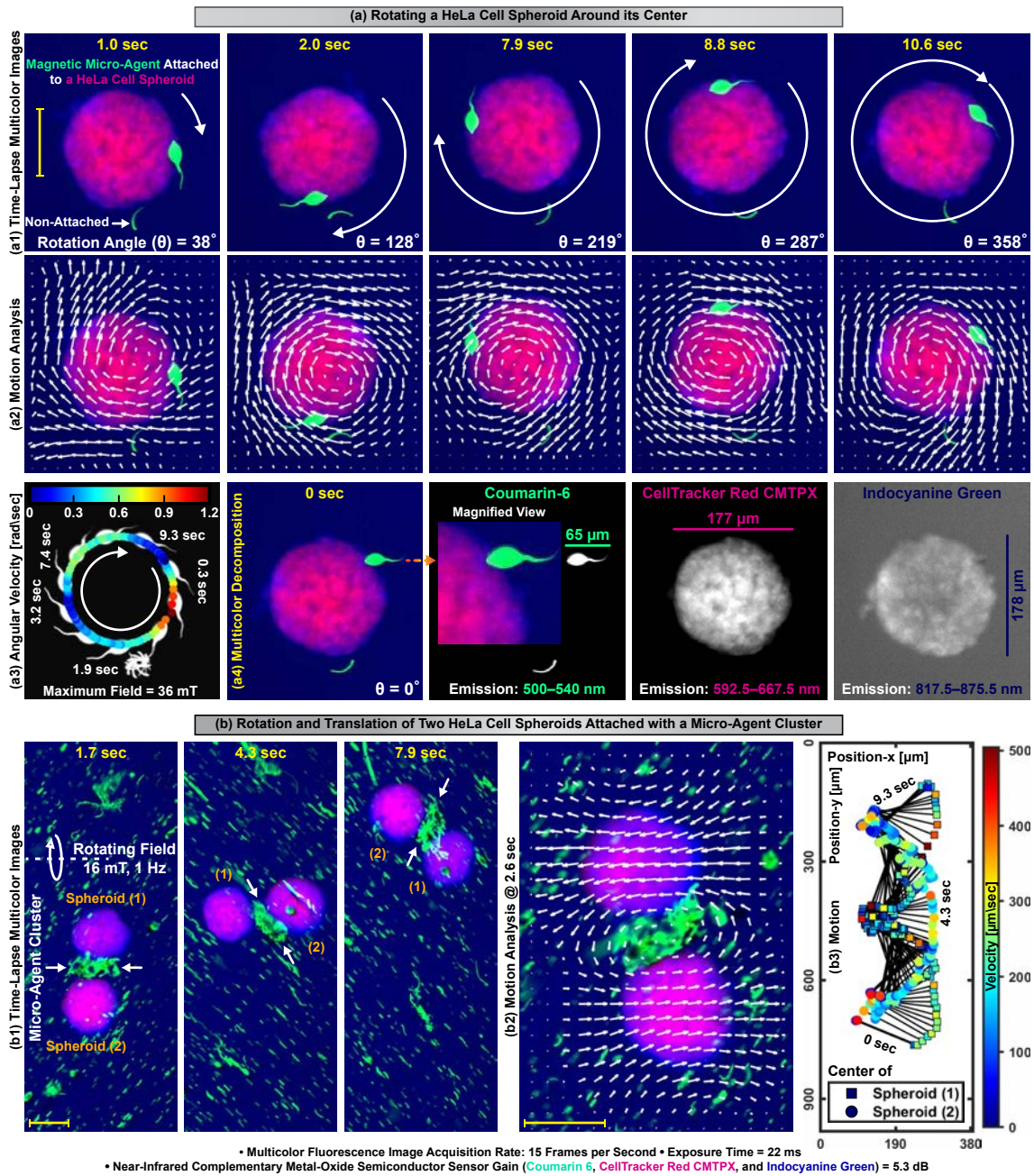


Figure 5.8: Rotation and translation of HeLa cell spheroids with micro-agents attachment in a reservoir filled with culturing medium and indocyanine green. (a1) and (b1) Actuation of the spheroids with single and cluster of micro-agent, respectively. (a2) and (b2) Vector fields overlaid on the time-lapse multicolor images show the rotational motion of the spheroids analyzed using Lucas-Kanade optical flow. (a3) and (b3) Motion profile and velocity information of the spheroids. (a4) Spectral image decomposition of the multicolor image at time zero. Scale bar: 100 μm .

5.3.4 Micro-Agents Attachment to Immobilized HeLa Cell Spheroids

For creating a 3D simplified tumor model, a microfluidic chip that is able to immobilize a single HeLa cell spheroid with a diameter between 100 μm and 250 μm is developed [208]. The chip contains a chamber constructed using a U-shaped pillar array with a spacing of 80 μm , which blocks the escape of the spheroid and allows the entrance of micro-agents (Fig. 5.9-(a1)). During the injection, the pillars trap the spheroid (Fig. 5.9-

(a2)). An air bubble is subsequently transferred into the chip to immobilize the spheroid by creating a pressure difference between the inside and outside of the pillar array (Fig. 5.9-(a3)). Thus, the spheroid is fixed in a certain location for multicolor experiments, unlike random positioning in the open reservoir. The chip is filled with 250 $\mu\text{g/ml}$ indocyanine green in the cell culture medium to render it visible in fluorescence microscopy. The medium and micro-agents are injected without moving the spheroid owing to the pressure difference. Fig. 5.9-(b) demonstrates a time-lapse multicolor image for a micro-agent passing from between two pillars and under an immobilized spheroid. Fig. 5.9-(c1) shows a single micro-agent attachment by puncturing an immobilized spheroid with a magnetic field of 36 mT. Dynamic imaging is performed at 15 fps for 395 minutes to validate that the chip maintains spheroids to which micro-agents are attached for long-term multicolor microscopy. Acquired dynamic images reveal the photobleaching resistance of indocyanine green is lower than coumarin 6 and CMTPX. Fluorescence imaging of the chip is unable due to the photobleaching of indocyanine green at minute 170 where the pixel intensity drops of the spheroid and the micro-agent are 21.2% and 1.6%, respectively (Fig. 5.9-(c2) and (c3)). In order to recover the fluorescence imaging of the chip, the excitation light is turned off for an hour. Diffusion of non-bleached indocyanine green molecules from outside the imaging area to the inside during off time enables the multicolor microscopy again (Fig. 5.9-(c4)) [139]. Fluorescence recovery is not able to be performed in the reservoir since the medium completely evaporates due to the heat produced by the excitation light (Fig. 5.6-(a3), (b2), and (c2)). The reservoir is not sealed to show the difference between open and closed microfluidic platforms in terms of multicolor image acquisition. The experiments conducted in our study demonstrate that the reservoir (as an open platform) and the microfluidic chip (as a closed platform) are able to be employed for real-time multicolor microscopy. However, evaporation of the medium inside the reservoir disables multicolor image acquisition after a certain time. An open reservoir is not a stable environment for visualizing long-term changes using dynamic multicolor imaging as long as it is not sealed with an air-tight transparent chamber to prevent evaporation. On the other hand, the chip keeps the heated medium inside it to (1) enable long-term microscopy and (2) prolong the multicolor imaging time by fluorescence recovery. In order to verify that fluorescence recovery does not affect the attachment, the micro-agent is randomly moved with a magnetic field of 14 mT between minutes 264 and 267 (Fig. 5.9-(c5)). The maximum velocity for the distal end of the micro-agent is measured 67 $\mu\text{m/sec}$ (1.3 body-length/sec), and no detachment is observed. Fig. 5.9-(c6) verifies the attachment by showing the part of the micro-agent inside the spheroid at minute 395. Multiple micro-agents are attached to an immobilized spheroid with a 16 mT rotating field at 5 Hz (Fig. 5.9-(d)). We observe that the attached micro-agents form a cluster over time as a result of dipole-dipole interaction (Fig. 5.9-(e)). Although a micro-agent cluster has the capability to actuate spheroids as shown in Fig 5.7-(b1), the displacement of the spheroid is measured 0 μm for 137 minutes. Our experiment shows that the chip creates a static environment for multicolor microscopy by allowing multiple micro-agents to be attached without moving the spheroid. We experimentally validate that our tumor model provides a controllable and stable testbed for multicolor image acquisition of single and multiple micro-agent attachments to a spheroid. In order to verify that multicolor microscopy can visualize micro-agents in vascularized environments, a vascular network on a microfluidic system is used as an experimental testbed.

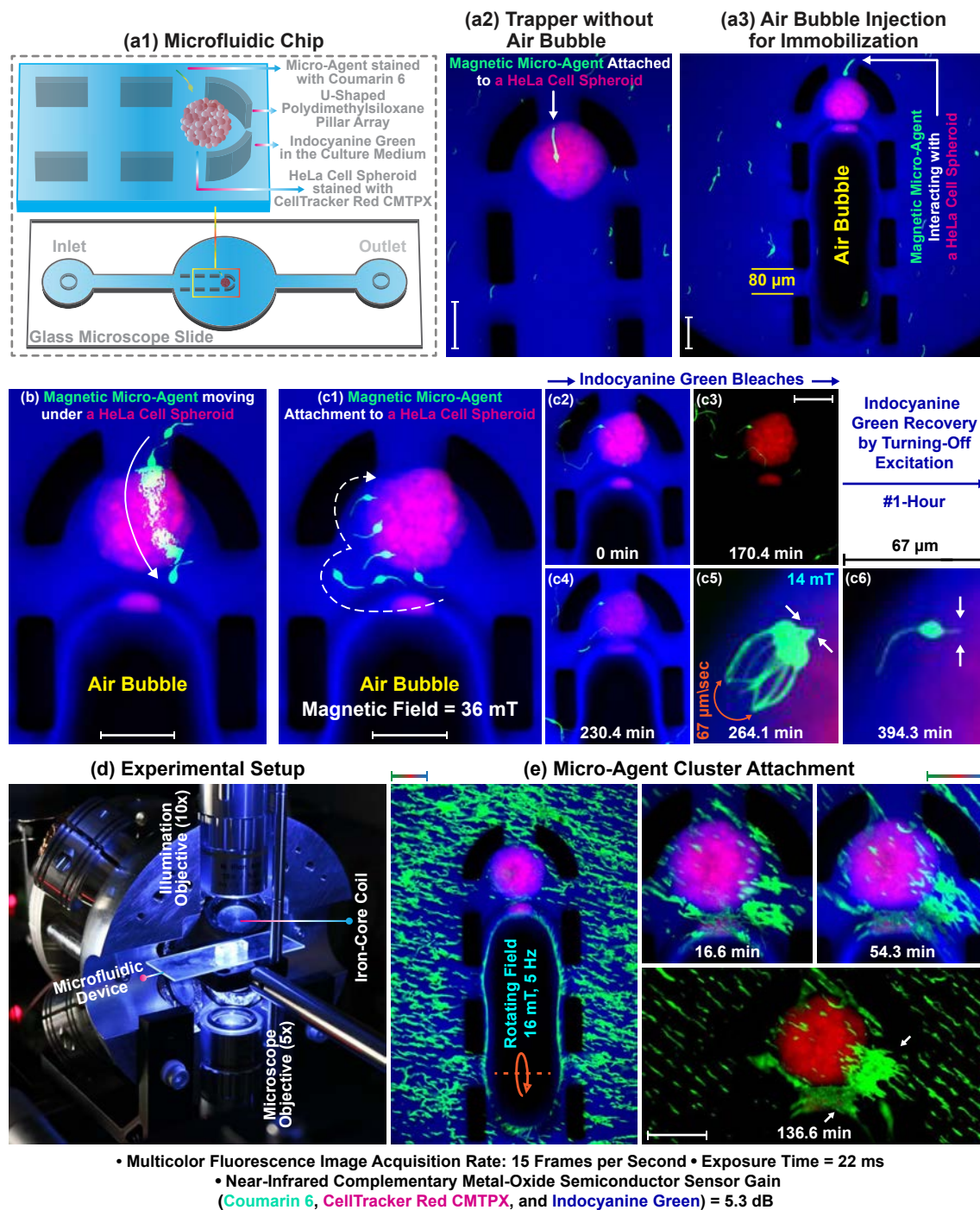


Figure 5.9: Multicolor fluorescence microscopy for visualizing the magnetic micro-agents in a microfluidic environment. (a1) Layout of the chip designed for immobilizing a single HeLa cell spheroid. (a2) Micro-agent attached to a trapped spheroid. (a3) Immobilizing a spheroid using an air bubble. (b) Overlaid image shows a micro-agent traveling under an immobilized spheroid. (c1) Attachment of a micro-agent to an immobilized spheroid. (c2)-(c4) Fluorescence recovery after photobleaching of indocyanine green. (c5) Attachment check by magnetically moving the micro-agent. (c6) Arrows indicate the part of the micro-agent inside the spheroid. (d) Workspace of the setup used for microscopy and magnetic actuation. (e) Formation of a micro-agent cluster attached to the spheroid. Scale bar: 100 μm .

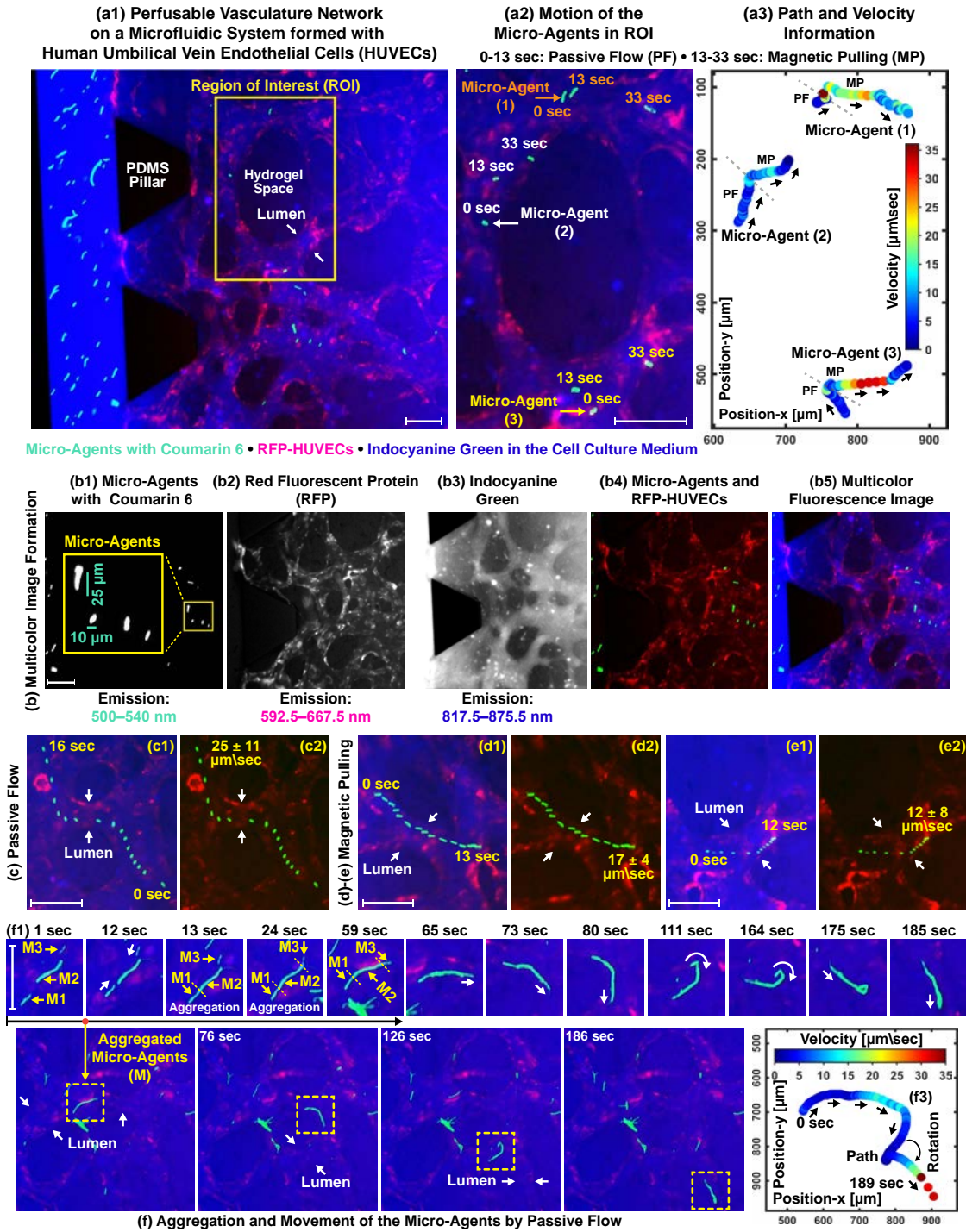
5.3.5 Micro-Agents inside a Perfusable Vascular Network

In vitro perfusable vascular network is engineered by co-culture of RFP-HUVECs and bone marrow-derived mesenchymal stem cells in a microfluidic system. For multicolor

microscopy, 250 $\mu\text{g/ml}$ indocyanine green in the cell culture medium and micro-agents are injected into the system. Fig. 5.10-(a1) depicts a static multicolor image of the microfluidic system featuring the engineered vascular network and micro-agents. Fig. 5.10-(a2) demonstrates the magnified view of the ROI defined on the multicolor image and highlights the movement of micro-agents in the vascular network by passive flow and magnetic pulling with a field of 70 mT. Micro-Agent (1) freely moves along the magnetic field, whereas Micro-Agents (2) and (3) hit the lumen walls after 33 seconds. Our experiment display that micro-agents perfuse into the vascular network via lumen openings and can be simultaneously tracked (Fig. 5.10-(a3)). Fig. 5.10-(b) shows representative multicolor image formation and verifies that micro-agents, vascular network, and microfluidic system are spectrally resolved in three distinct spectrum bands. The structural morphology of the vascular network is visualized from dual spectrum bands (592.5–667.5 nm and 817.5–875.5 nm) owing to the diffusion of indocyanine green in the culturing medium (Fig. 5.10-(b2) and (b3)). This enables complete visualization of the vasculature structure and clearly delineates the hydrogel space (Fig. 5.10-(b4) and (b5)). The mobility of the micro-agents inside the vascular network is visualized in three sets of multicolor experiments under non-cell culture conditions. In all experiments, multicolor images are acquired at 3 fps to minimize the photodamage on RFP. The higher image acquisition rate is achievable with incubation conditions since RFP-HUVECs have an active good working metabolism to rebuild the fluorescence signals. The first experiment is conducted to visualize a micro-agent moved by the passive flow (Fig. 5.10-(c)). The average velocity of the micro-agent is computed as 3.3 body-length/sec (25 $\mu\text{m/s}$). The second experiment is designed to visualize micro-agents magnetically pulled against the passive flow with a field of 42 mT. Fig. 5.10-(d) and (e) shows the overlaid time-lapse images of the micro-agents movement with the average velocity of 1.4 body-length/sec (17 $\mu\text{m/s}$) and 2.5 body-length/sec (12 $\mu\text{m/s}$), respectively. In the third experiment, the aggregation of three micro-agents utilizing electrostatic forces is visualized (Fig. 5.10-(f1)). The aggregated micro-agents are moved by the passive flow with the average velocity of 0.04 body-length/sec (4 $\mu\text{m/s}$) (Fig. 5.10-(f2) and (f3)). Acquired multicolor images reveal that no disaggregation occurs for 186 seconds (Fig. 5.10-(f1) and (f2)). Our imaging experiments demonstrate that multicolor microscopy: (1) provides spatiotemporal resolution for quantitative analysis of the micro-agents inside the vasculature, (2) allows image acquisition of the micro-agents with a minimum length of 5 μm , (3) enables unambiguous color-coding of both micro-agents and engineered vascular morphology in real-time. Next, we report the multicolor microscopy performance by visualizing micro-agents inside and outside the natural blood vessels.

5.3.6 Micro-Agents inside Chorioallantoic Membrane Vasculature

Ex ovo chorioallantoic membrane (CAM) vasculature containing the hierarchical multiscale blood vessels is used to visualize the micro-agents in a native environment (Fig. 5.11-(a1)). Fig. 5.11-(a2) and (a3) show the structural morphology of the vasculature visualized using bright-field as a reference and multicolor microscopy with autofluorescence of erythrocytes, respectively. The multicolor image is formed by spectral unmixing of three main cellular features: vasculature, erythrocytes, and CAM (Fig. 5.11-(a4)). We perfuse the CAM using DPBS to completely remove the free-floating erythrocytes within the vasculature structures. This decellularized vascular structure allows free movement of micro-agents as well as multiple fluorophore solutions. For staining, vasculature is placed in a Petri dish containing 250 $\mu\text{g/ml}$ indocyanine green in culture medium, 100 $\mu\text{g/ml}$ Rhodamine B in water, and the micro-agents for an overnight period. Before the imaging experiments,



• Multicolor Image Acquisition Rate: 3 Frames per Second • Exposure Time = 110 ms
• Near-Infrared Complementary Metal-Oxide Semiconductor Sensor Gain (Coumarin 6, RFP-HUVECs, and Indocyanine Green) = 5.3 dB

Figure 5.10: Multicolor fluorescence microscopy for visualizing the magnetic micro-agents in a perfusable vasculature network. (a1) Multicolor image of the micro-agents labeled with coumarin 6 in a vasculature formed with RFP-HUVECs on a microfluidic system filled with culture medium and indocyanine green. (a2) Movement of the micro-agents by passive flow and magnetic pulling with a field of 70 mT. (a3) Path and velocity of the micro-agents. (b) Multicolor image formation by overlapping the acquired spectrally-different images. (c1) and (d1)-(e1) Movement of the micro-agents in a lumen by passive flow and magnetic pulling with a field of 42 mT, respectively. (c2)-(e2) Merged fluorescence images of the micro-agents and lumens. (f1) and (f2) The aggregation and movement of the micro-agents in a vasculature by passive flow, respectively. (f3) Velocity and path of the aggregated micro-agents. Scale bar: 100 μm.

the dish containing the stained sample is washed with DPBS by manual shaking for 15 minutes to prevent the aggregation of the micro-agents on the CAM. A circular part with a diameter of 15 mm is cut out from the sample and transferred onto a PDMS reservoir for multicolor microscopy. The representative static multicolor image of a decellularized bifurcated blood vessel and the micro-agents after DPBS washing is shown in Fig. 5.11-(b1). ROI (1)-(3) defined on the multicolor image plane highlight micro-agents on the chorioallantoic membrane, on the vessel wall, and inside the vessel, respectively. In order to reveal details about micro-agents and vessels, the magnified view of ROI (1)-(3) are shown in Fig. 5.11-(b1)-(b3), respectively. Spectral image decomposition of ROI (2) and (3) verifies that the micro-agents and the vessel are imaged from different spectrum bands, and there is a contrast difference between CAM and vessel wall (Fig. 5.11-(b2) and (b3)). The contrast difference decreases by 90% since heterogeneous pores present on the vessel wall allow diffusion of Rhodamine B and indocyanine green (Fig. 5.11-(c) and (d)). Real-time multicolor images are acquired at 5 fps with 66 ms exposure time, where the micro-agents are pulled with a magnetic field of 42 mT. The average velocity of the micro-agents moving outside and inside the vessel is computed as 1 body-length/sec length/sec ($8 \mu\text{m/s}$) and 0.5 body-length/sec length/sec ($2 \mu\text{m/s}$), respectively (Fig. 5.11-(c) and (d)). The micro-agent inside the vessel is pulled until it reaches the wall. The displacement of the micro-agent after it reaches the vessel wall is measured as $0 \mu\text{m}$ for 5 minutes, whereas the micro-agents outside travel along the magnetic field (Fig. 5.11-(d)). Our experiment demonstrates that multicolor microscopy provides real-time visualization of the micro-agents inside the natural blood vessels.

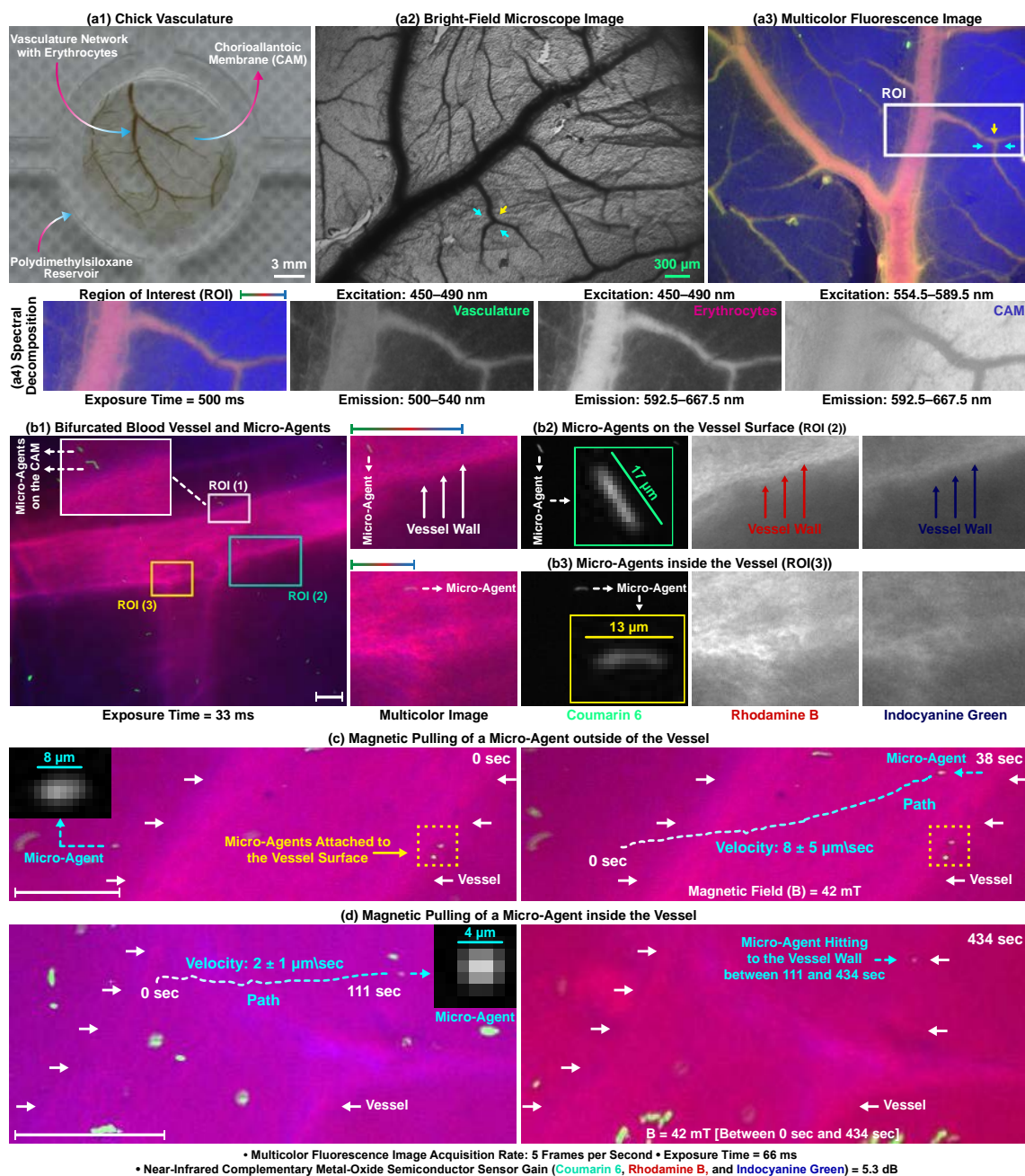
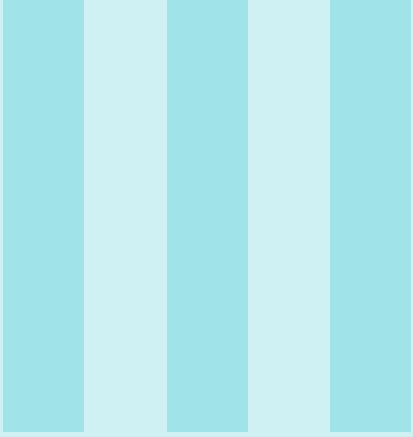


Figure 5.11: Multicolor fluorescence microscopy for visualizing the magnetic micro-agents in *ex ovo* chicken chorioallantoic membrane. (a1) Prepared sample for vasculature network visualization utilizing autofluorescence property of erythrocytes. (a2) and (a3) Bright-field and multicolor images of the network, respectively. (a4) Spectral decomposition of ROI on (a3). (b1) Multicolor image of the micro-agents labeled with coumarin 6 and a vessel containing Rhodamine B and indocyanine green. ROI (1)-(3) on (b1) showing the micro-agents on the membrane, on the vessel surface, and inside the vessel, respectively. (b2) and (b3) Magnified view and spectral decomposition of ROI (2) and (3), respectively. (c) and (d) Magnetic movement of the micro-agents outside and inside the vessels, respectively. Scale bar: 100 μm .

5.4 Conclusions

In this work, we demonstrate multicolor fluorescence microscopy to visualize polymeric micro-agents within 3D tumor-on-a-chip and vasculature models for the envisioned application of targeted drug delivery. Compared to the imaging techniques used in the literature,

micro-agents and surroundings are spectrally resolved in three distinct spectrum bands, and color-coded visualization of the models is acquired. We experimentally validate that multicolor microscopy allows spectrally-different image acquisition of micro-agents at varying aspect ratios, organic bodies, surrounding media up to 15 fps, and sequential motion detection up to 504 $\mu\text{m/s}$ from each spectrum band. As a result of color-coding, an increased understanding of the identification and discrimination of each micro-component is obtained. Our measurements show that multicolor microscopy delineates the spatial compartments in real-time for analyzing and verifying the functionality of the micro-agents. We expect real-time multicolor microscopy to accelerate the translation of micro-agents into practice by enabling the required clear visualization.



Concluding Remarks

6	Conclusions	113
6.1	Part I - Scientific Tools	
6.2	Part II - System Integration	
6.3	Outlook	
	Bibliography	119
	Articles	
	Books	
	Acknowledgments	133
	About the Author	135

6. Conclusions

The previous chapters in this thesis provided solutions to the challenges associated with fabrication, actuation, and imaging of micro-agents. In a nutshell, individual chapters in the parts explored topics from interdisciplinary fields to bridge the gap between microrobotics and multicolor microscopy. This last chapter summarizes **Chapters 2-5** that answer the research questions (**R.Q. 1-4**) stated in **Chapter 1**, presents the main contributions, and provides directions for future research.

6.1 Part I - Scientific Tools: Multicolor Microscope, Coil Driver, and Visual Tracker

Chapter 2 addresses the lack of multiplexed imaging in the literature to distinguish micro-agents and physical surroundings from different spectrum bands. A widefield multicolor fluorescence microscope is developed for visualizing micro-agents and surroundings by relatively fast spectral multiplexing. The working principle of the microscope is sequential excitation of the fluorophores in a round-robin manner and synchronous individual image acquisition using a common optical path (**R.Q. 2**). Polystyrene micro-beads as surrogates for drug carriers and cancer spheroids formed with HeLa cells are randomly placed inside a microfluidic channel to create a 3D tumor environment and show the potential of multicolor microscopy. It is experimentally validated that the micro-agents, spheroids, and channels are spectrally unmixed in three distinct spectrum bands by the multicolor microscope. The main findings are: (1) Synchronous individual image acquisition enables occlusion-free visualization of each micro-components with spectral crosstalk correction. (2) The round-robin excitation strategy minimizes the photodamage on the fluorophores for real-time and dynamic multicolor microscopy, prolonging the imaging time by a minimum of 1.5 fold. (3) Focused individual image acquisition from multiple planes ensures visualizing a 3D tumor model containing micro-agents without blurring. Imaging experiments demonstrate that the developed microscope has the capability to provide the required high spatiotemporal resolution (1280×1024 pixels with a minimum 5.5 ms exposure time) for micro-agents and surroundings. The multicolor microscope could be a desirable tool in the application

domain of microrobotics by spectral decomposition of full samples. In order to visualize the micro-agents actuated using magnetic fields, the microscope is coupled with an orthogonal array of four coils.

Chapter 3 presents a driver architecture to power the coils, which has not been studied in the microrobotics literature (**R.Q. 3**). The effect of PWM frequency on the current, magnetic field, and ohmic losses are studied using the developed coil driver. Experimental results show that driving the coils at PWM frequencies close to their self-resonant frequencies minimizes the magnitude of the current ripple. This results in (1) the reduction of magnetic field fluctuation and (2) increasing predictability of the field, which is one of the main components of magnetic manipulation. It is measured that increasing the PWM drive frequency of an air-core coil (with a self-resonant frequency of 45 kHz) from 100 Hz to 25 kHz decreases the current ripple and magnetic fluctuation by two orders of magnitude. Additionally, negligible ohmic loss difference (%2.8) is observed after 100 minutes. Experimental results highlight the importance of PWM frequency for the manipulation of micro-agents using magnetic field gradients. Magnetically-actuated micro-agents are visually tracked to obtain quantitative data.

Chapter 4 describes a template-based visual tracking method for micro-agents. The methods used in the literature are based on detecting micro-agents in every new frame and tracking with a Kalman filter. The main shortcomings in such methods are: (1) Detecting micro-agents requires thresholding, and values vary depending on the image. (2) Tracking suffers from inaccuracies due to failures in the detection. (3) Micro-agents with different geometries can not be tracked using the same tracking algorithm. Template-based tracking method overcomes these shortcomings by computing motion parameters instead of micro-agents detection in every frame. Experimental results show that different types of micro-agents could be visually tracked by computing their motion information between two consecutive frames without using any specific detection and thresholding procedure (**R.Q. 4**). The outputs of the visual trackers are used to provide feedback for the control of micro-agents. Such measurement rates can be lower than the sampling rates used in traditional closed-loop controllers. Multi-rate state observers are applied to virtually increase the sampling rate for the controllers by estimating the positions of the micro-agents between two consecutive frames. The output of the template-based visual tracker is provided as a measurement to the state observers for upsampling the actual image acquisition rate. The experiments show that when the image acquisition rate is increased from 25 fps to 200 fps using the multi-rate state estimation, the maximum error is computed as $48 \mu\text{m}$ for an elliptical-shaped micro-agent of $790 \mu\text{m} \times 1000 \mu\text{m}$ in size. The software and hardware tools presented in **Chapters 2-4** are employed in **Chapter 5** to visualize magnetically-actuated micro-agents and dynamic environments by real-time multicolor fluorescence microscopy.

6.2 Part II - System Integration and Real-Time Multicolor Microscopy

Chapter 5 reports the first demonstration of real-time multicolor fluorescence microscopy in the field of microrobotics. The performance of multicolor microscopy is analyzed by visualizing agents within microfluidic environments. In order to create a non-vascularized 3D tumor environment, a microfluidic chip that immobilizes a single cancer spheroid and allows free movement of the micro-agents is developed. The feature of the chip is that the spheroids are fixed in a certain location for multicolor image acquisition without the need for moving parts. *In vitro* perfusable vascular network is engineered on a microfluidic

system to show that multicolor microscopy provides spectrally-different image acquisition of the agents inside the vascularized environments. Besides, *ex ovo* chicken chorioallantoic membrane is employed to visualize micro-agents inside the natural blood vessels. For imaging experiments, magnetic and fluorescent micro-agents (ranging from 4 μm to 130 μm) are fabricated by shortening continuous fibers synthesized using electrospinning. Multiple imaging experiments verify that mobile micro-agents, organic bodies (HeLa cell spheroids and vascular network), and chamber media are resolved in three distinct spectrum bands. The sequential motion is detected from each spectrum band up to 504 $\mu\text{m}/\text{sec}$ when the individual images (with the size of 1280×1024 pixels) are acquired at 45 fps (**R.Q. 1**). The spectrally-resolved images provide direct segmentation of each micro-component for quantitative analysis owing to the crosstalk correction strategy presented in **Chapter 2**. Experimental results in this chapter indicate that multicolor microscopy delineates the spatial compartments in real-time to identify the target, manipulate the micro-agents, and reach the desired location. Real-time multicolor microscopy that spectrally resolves samples without crosstalk will be a powerful imaging technique for broad applications in microrobotics (e.g., microfluidics-based healthcare, micro-assembly, sensing). This doctoral thesis validates that multicolor microscopy changes the current understanding of visual tracking and localization in the microrobotics field by rendering unambiguous identification of micro-agents and surroundings. Outcomes of **Chapters 2-5** can contribute together or individually to the development of specific micro-agents. Methods and results presented in the chapters also provide information about the construction of imaging, actuation, and fabrication setups for microrobotics applications (e.g., organic body manipulation for tissue engineering, flow screening within the vascular networks, and visualizing morphological dynamics of cells after cargo delivery). Among the applications, targeted drug delivery is the most achievable using the direct outcome of this thesis. The subsequent section provides implications for follow-up therapeutic microrobotics studies.

6.3 Outlook

So far, this thesis has outlined the application of multicolor microscopy in the field of microrobotics. A widefield multicolor fluorescence microscope is introduced to obtain spectrally resolved visualization of samples containing mobile micro-agents. Electrospinning-based fabrication protocol is presented to obtain fluorescent and magnetic micro-agents as surrogates for drug carriers. A magnetic actuation system, including driver electronics, is constructed to manipulate the fabricated micro-agents. A template-based visual tracking method is applied to obtain quantitative information. 3D tumor-on-a-chip and vasculature models are developed to demonstrate the performance of multicolor microscopy and create drug screening platforms. The outlook section concludes this doctoral journey by providing directions to fabricate therapeutic agents, perform *in vivo* multicolor imaging, and accelerate the clinical translation of microrobotics. The section starts by detailing the fabrication of micro-agents as drug carriers.

6.3.1 Fabrication of Polymeric Micro-Agents containing Drugs

Regardless of the fabrication method and polymer solution, the first step will be drug selection and monitoring its effectiveness using a microfluidic gradient generator [209]. The results obtained using the gradient generator will show the concentration that should be loaded into the micro-agents for high treatment efficacy. The electrospinning process presented in this thesis is one of the techniques for drug-loaded micro-agent fabrication.

Polystyrene is chosen as the carrier polymer to fabricate micro-agents due to its biocompatibility. However, carrier polymer should also have biodegradability properties in drug delivery applications. The biocompatibility and controllable biodegradability of poly(lactic-co-glycolic acid) (PLGA) make it one of the suitable candidates to be used as a carrier polymer in future studies [210, 211]. Dimethylformamide and dichloromethane are two solvent examples to prepare a PLGA solution for electrospinning. Coumarin 6 and iron-oxide nanoparticles are biocompatible compounds to make the polymer solution fluorescent and magnetic, respectively. Coumarin 6 is homogeneously dispersed in PLGA and displays a relatively high photobleaching resistance. Micro-agents (approximately 52 μm in length) containing iron-oxide nanoparticles can be actuated with a low magnetic field (14 mT) in biological fluids like a fetal bovine serum, as demonstrated in **Chapter 5**.

Hydrophobic drugs (e.g., paclitaxel, docetaxel, etoposide) can be directly mixed with the magnetic and fluorescent polymer solution since they are immobilized in the PLGA matrix [212, 213]. Hydrophilic drugs (e.g., cisplatin, doxorubicin hydrochloride) will need encapsulation as they are not stable in the polymer matrix when in contact with water. The coaxial electrospaying process provides a method for encapsulating drug solutions with a polymer shell [214]. Encapsulated drugs can be used as micro-agents or placed inside the fibers using the coaxial electrospinning process. Obtaining micro-agents by shortening the synthesized fibers in equal sizes will be required for reproducible drug delivery and testing. The electrospinning setup in **Chapter 5** is designed for depositing the fibers on the collector with random orientation. The polymer grinding process also randomly shortens the beaded and straight fibers to obtain micro-agents. This fabrication technique is selected to enable the validation of multicolor image acquisition using micro-agents with random size distribution. In order to obtain micro-agents with desired sizes, electrospun fibers will be aligned with a drum collector and cut into small pieces using a laser [203]. Electrospinning/spraying are not techniques for fabricating micro-agents with architectural complexity, as in lithography and direct laser writing. The setup(s) only allows the fabrication of therapeutic micro-agents with spherical (or elliptical), beaded, and straight fiber shapes for the follow-up studies. The surface of the fabricated micro-agents can be conjugated with antibodies (e.g., anti-EpCam, anti-CA125, anti-PD-1) for adhering them to the unhealthy cells. Lyophilization will be necessary for the long-term storage of the micro-agents by inhibiting PLGA hydrolysis [72]. *In vitro* experiments will be conducted to monitor drug release from the micro-agents.

6.3.2 Visualization of Drug Release and Cellular Viability

The multicolor microscope presented in **Chapter 2** can provide real-time visualization of targeted drug delivery, release kinetics, and cellular viability on the microfluidic platforms. The microscope is specially designed with long-working distance objective lenses to provide space for the integration of remote actuation and drug release systems. Combining illumination and emission units using multi-band dichroic mirrors can offer a larger working area. In order to perform live-cell imaging, the multicolor microscope will be combined with an incubation chamber to adjust carbon dioxide, oxygen, humidity, and temperature. Perfusable vascular network experiments in **Chapter 5** are conducted without a cell culture incubator. It is observed that endothelial cells are unable to regenerate red fluorescence protein for multicolor microscopy and die within an hour due to non-optimal conditions. In the absence of an incubation unit, live cells can not be maintained due to environmental conditions, causing the inaccurate observation of drug efficacy.

Under incubation conditions, drug release can be triggered remotely by raising the

temperature of the micro-agents, for example, using an alternating magnetic field, focused ultrasound waves, or near-infrared light [215]. Solvents and pH solutions can also be used to activate the release by accelerating polymer erosion [216, 217]. In future studies, the temperature rise and chemical activation will be used (1) generating pores in the encapsulation shells for the escape of hydrophilic drugs and (2) breaking the bonds between the carrier polymer and hydrophobic drugs for controlled release. Fluorescence microscopy is a commonly used method to obtain drug release kinetics from the agents by measuring their average intensity over time. Live/dead staining assays will be employed to monitor cellular viability for drug response assessment by dual-color fluorescence microscopy. The assay solution is a mixture of two fluorophores that render live and dead cells visible in different spectrum bands. The microfluidic chip in **Chapter 5** is designed as a platform for drug delivery to cell spheroids and viability analysis after release.

The immobilization feature of the chip can provide a controlled test environment to visualize the interaction between micro-agents and 3D cancer spheroids. The perfusable vascular network on the microfluidic system is a testbed to monitor the effect of therapeutic micro-agents targeted at inhibiting the spread of unhealthy cells. The vascular network can be used to screen metastasis dynamics by perfusing tumor cells via lumen openings. Visualizing the testbed will open a pathway for increased comprehension of the effect of therapeutic micro-agents on both vascular morphology and metastasis cells. Upon extensive testing under *in vitro*, drug delivery using micro-agents will be studied at the whole organism level. However, the widefield multicolor microscope presented in this thesis (1) is a tool for acquiring spectrally resolved visualization of agents and physical surroundings in microfluidic environments, and (2) provides superficial imaging depth compared to medical imaging modalities (e.g., ultrasound, photoacoustic). In the final part of this thesis, the microscope-in-a-catheter concept is proposed to render the micro-agents visualization inside the tissue by multicolor imaging.

6.3.3 Multicolor Microscope-in-a-Catheter

The incorporation of optical fibers into catheters (i.e., catheter probes) enables the transmission of light deep inside the biological tissue and the collection of photons for image formation [218]. Coupling the catheter probe with microscopy techniques (i.e., microscope-in-a-catheter) allows invasive imaging of tissue microstructures with high-resolution [219, 220]. In future work, multicolor microscopy will be combined with the catheter probe to achieve (1) spectrally-resolved visualization of micro-agents in tissue and (2) delineating the borders between healthy and unhealthy cells. A catheter probe can be a versatile tool for the application domain of microrobotics. For instance, a catheter probe will allow the transportation of micro-agents to the targeted tissue as well as their visualization. The fibers in the catheter probe can also permit the transmission of near-infrared light for triggering drug release. The probe can overcome the limited penetration depth of near-infrared light (1-2 mm) by transmitting deep into the tissue for clinical drug release applications. A catheter probe coupled with multicolor microscopy has the potential to open new possibilities for testing therapeutic micro-agents under *in vivo* conditions.

Bibliography

Articles

- [1] Metin Sitti. “Voyage of the microrobots”. In: *Nature* 458.7242 (2009), pages 1121–1122.
- [2] Pelin Erkoc et al. “Mobile microrobots for active therapeutic delivery”. In: *Advanced Therapeutics* 2.1 (2019), page 1800064.
- [3] Veronika Magdanz et al. “IRONSPERM: Sperm-templated soft magnetic microrobots”. In: *Science Advances* 6.28 (2020), eaba5855.
- [4] Ryan L Truby and Shuguang Li. “Integrating chemical fuels and artificial muscles for untethered microrobots”. In: *Science Robotics* 5.45 (2020), eabd7338.
- [5] Bradley J Nelson et al. “Microrobots for minimally invasive medicine”. In: *Annual Review of Biomedical Engineering* 12 (2010), pages 55–85.
- [6] Samuel Sánchez et al. “Chemically powered micro-and nanomotors”. In: *Angewandte Chemie International Edition* 54.5 (2015), pages 1414–1444.
- [7] S Tasoglu et al. “Untethered micro-robotic coding of three-dimensional material composition”. In: *Nature Communications* 5.1 (2014), pages 1–9.
- [8] Wuming Jing et al. “A microforce-sensing mobile microrobot for automated micromanipulation tasks”. In: *IEEE Transactions on Automation Science and Engineering* 16.2 (2018), pages 518–530.
- [9] Metin Sitti et al. “Biomedical applications of untethered mobile milli/microrobots”. In: *Proceedings of the IEEE* 103.2 (2015), pages 205–224.
- [10] Twan Lammers et al. “Cancer nanomedicine: is targeting our target?” In: *Nature Reviews Materials* 1.591 (2016), page 16069.
- [11] Michael Torrice. “Does nanomedicine have a delivery problem?” In: *ACS Central Science* 2.7 (2016), pages 434–437.
- [12] Christine K Schmidt et al. “Engineering microrobots for targeted cancer therapies from a medical perspective”. In: *Nature Communications* 11.1 (2020), pages 1–18.

- [13] Ouajdi Felfoul et al. “Magneto-aerotactic bacteria deliver drug-containing nanoliposomes to tumour hypoxic regions”. In: *Nature Nanotechnology* 11.11 (2016), pages 941–947.
- [14] Junyang Li et al. “Development of a magnetic microrobot for carrying and delivering targeted cells”. In: *Science Robotics* 3.19 (2018), eaat8829.
- [15] A Nacev et al. “The behaviors of ferromagnetic nano-particles in and around blood vessels under applied magnetic fields”. In: *Journal of Magnetism and Magnetic Materials* 323.6 (2011), pages 651–668.
- [16] Franziska Ullrich et al. “Recent progress in magnetically actuated microrobotics for ophthalmic therapies”. In: *European Ophthalmic Review* 8 (2014), pages 120–126.
- [17] Mariana Medina-Sánchez et al. “Cellular cargo delivery: Toward assisted fertilization by sperm-carrying micromotors”. In: *Nano Letters* 16.1 (2016), pages 555–561.
- [18] Islam SM Khalil et al. “Rubbing against blood clots using helical robots: Modeling and *in vitro* experimental validation”. In: *IEEE Robotics & Automation Letters* 2.2 (2017), pages 927–934.
- [19] Fernando Soto et al. “Medical micro/nanorobots in precision medicine”. In: *Advanced Science* 7.21 (2020), page 2002203.
- [20] Franziska Ullrich et al. “Mobility experiments with microrobots for minimally invasive intraocular surgery”. In: *Investigative Ophthalmology & Visual Science* 54.4 (2013), pages 2853–2863.
- [21] Evin Gultepe et al. “Biopsy with thermally-responsive untethered microtools”. In: *Advanced Materials* 25.4 (2013), pages 514–519.
- [22] Sumit Mohanty et al. “Contactless acoustic micro/nano manipulation: a paradigm for next generation applications in life sciences”. In: *Proceedings of the Royal Society A* 476.2243 (2020), page 20200621.
- [23] Hakan Ceylan et al. “Translational prospects of untethered medical microrobots”. In: *Progress in Biomedical Engineering* 1.1 (2019), page 012002.
- [24] Sagar Chowdhury et al. “Controlling multiple microrobots: recent progress and future challenges”. In: *Journal of Micro-Bio Robotics* 10.1 (2015), pages 1–11.
- [25] Yunus Alapan et al. “Multifunctional surface microrollers for targeted cargo delivery in physiological blood flow”. In: *Sci. Robotics* 5.42 (2020), eaba5726.
- [26] Jeonghyo Kim et al. “Microrobotic photocatalyst on-the-fly: 1D/2D nanoarchitectonic hybrid-based layered metal thiophosphate magnetic micromachines for enhanced photodegradation of nerve agent”. In: *Chemical Engineering Journal* (2022), page 137342.
- [27] Metin Sitti and Diederik S Wiersma. “Pros and cons: Magnetic versus optical microrobots”. In: *Advanced Materials* 32.20 (2020), page 1906766.
- [28] Islam SM Khalil et al. “The control of self-propelled microjets inside a microchannel with time-varying flow rates”. In: *IEEE Transactions on Robotics* 30.1 (2013), pages 49–58.
- [29] Nafiseh Ebrahimi et al. “Magnetic actuation methods in bio/soft robotics”. In: *Advanced Functional Materials* 31.11 (2021), page 2005137.
- [30] Zhengxin Yang and Li Zhang. “Magnetic actuation systems for miniature robots: A review”. In: *Advanced Intelligent Systems* 2.9 (2020), page 2000082.
- [31] Kyoungrae Cha et al. “Electromagnetic actuation methods for intravascular locomotive microrobot”. In: *2010 Annual International Conference of the IEEE Engineering in Medicine and Biology* (2010), pages 1962–1965.

- [32] Federico Ongaro et al. “Design of an electromagnetic setup for independent three-dimensional control of pairs of identical and nonidentical microrobots”. In: *IEEE Transactions on Robotics* 35.1 (2018), pages 174–183.
- [33] Zhengxin Yang et al. “Magnetic control of a steerable guidewire under ultrasound guidance using mobile electromagnets”. In: *IEEE Robotics & Automation Letters* 6.2 (2021), pages 1280–1287.
- [34] Patrick Ryan and Eric Diller. “Magnetic actuation for full dexterity microrobotic control using rotating permanent magnets”. In: *IEEE Transactions on Robotics* 33.6 (2017), pages 1398–1409.
- [35] Abdelrahman Hosney et al. “Propulsion and steering of helical magnetic microrobots using two synchronized rotating dipole fields in three-dimensional space”. In: *2015 IEEE/RSJ Int. Conference on Intelligent Robots and Systems (IROS)* (2015), pages 1988–1993.
- [36] Belal Ahmad et al. “Mobile microrobots for *in vitro* biomedical applications: A survey”. In: *IEEE Transactions on Robotics* 38.1 (2021), pages 646–663.
- [37] Berna Özkale et al. “Modular soft robotic microdevices for dexterous biomanipulation”. In: *Lab on a Chip* 19.5 (2019), pages 778–788.
- [38] M. Selman Sakar et al. “Single cell manipulation using ferromagnetic composite micro-transporters”. In: *App. Physics Letters* 96.4 (2010), page 043705.
- [39] Irene Bernardeschi et al. “A review on active 3D microstructures via direct laser lithography”. In: *Advanced Intelligent Syst.* 3.9 (2021), page 2100051.
- [40] Fatemeh Rajabasadi et al. “3D and 4D lithography of untethered microrobots”. In: *Progress in Materials Science* 120 (2021), page 100808.
- [41] Kathrin E Peyer et al. “Bio-inspired magnetic swimming microrobots for biomedical applications”. In: *Nanoscale* 5.4 (2013), pages 1259–1272.
- [42] Andrew C Lamont et al. “Geometric determinants of in-situ direct laser writing”. In: *Scientific Reports* 9.1 (2019), pages 1–12.
- [43] Hakan Ceylan et al. “3D-printed biodegradable microswimmer for theranostic cargo delivery and release”. In: *ACS Nano* 13.3 (2019), pages 3353–3362.
- [44] Joshua Giltinan et al. “3D microprinting of iron platinum nanoparticle-based magnetic mobile microrobots”. In: *Advanced Intelligent Systems* 3.1 (2021), page 2000204.
- [45] Mukrime Birgul Akolpoglu et al. “High-yield production of biohybrid microalgae for on-demand cargo delivery”. In: *Advanced Science* 7.16 (2020), page 2001256.
- [46] Islam SM Khalil et al. “Magnetic propulsion of robotic sperms at low-Reynolds number”. In: *Applied Physics Letters* 109.3 (2016), page 033701.
- [47] Yingchun Su et al. “Melt electrospinning writing of magnetic microrobots”. In: *Advanced Science* 8.3 (2021), page 2003177.
- [48] Federico Ongaro et al. “Control of untethered soft grippers for pick-and-place tasks”. In: (2016), pages 299–304.
- [49] Seungmin Lee et al. “A needle-type microrobot for targeted drug delivery by affixing to a microtissue”. In: *Advanced Healthcare Materials* 9.7 (2020), page 1901697.
- [50] Immihan Ceren Yasa et al. “3D-Printed microrobotic transporters with recapitulated stem cell niche for programmable and active cell delivery”. In: *Advanced Functional Materials* 29.17 (2019), page 1808992.

- [51] Dongwook Kim et al. “Chemotactic steering of bacteria propelled microbeads”. In: *Biomedical Microdevices* 14.6 (2012), pages 1009–1017.
- [52] De Gong et al. “Magnetic biohybrid microrobot multimers based on chlorella cells for enhanced targeted drug delivery”. In: *ACS Applied Materials & Interfaces* 14.5 (2022), pages 6320–6330.
- [53] Sylvain Martel et al. “MRI-based medical nanorobotic platform for the control of magnetic nanoparticles and flagellated bacteria for target interventions in human capillaries”. In: *The International Journal of Robotics Research* 28.9 (2009), pages 1169–1182.
- [54] Mehmet Efe Tiryaki and Metin Sitti. “Magnetic resonance imaging-based tracking and navigation of submillimeter-scale wireless magnetic robots”. In: *Advanced Intelligent Systems* 4.4 (2022), page 2100178.
- [55] Sylvain Martel. “Microrobotics in the vascular network: present status and next challenges”. In: *Journal of Micro-Bio Robotics* 8.1 (2013), pages 41–52.
- [56] Veronica Iacovacci et al. “High-resolution SPECT imaging of stimuli-responsive soft microrobots”. In: *Small* 15.34 (2019), page 1900709.
- [57] Hyunchul Choi et al. “Electromagnetic actuation system for locomotive intravascular therapeutic microrobot”. In: *5th IEEE RAS/EMBS International Conference on Biomedical Robotics and Biomechatronics (BioRob)* (2014), pages 831–834.
- [58] Junsun Hwang et al. “A review of magnetic actuation systems and magnetically actuated guidewire-and catheter-based microrobots for vascular interventions”. In: *Intelligent Service Robotics* 13.1 (2020), pages 1–14.
- [59] Stefano Pane et al. “Dynamic tracking of a magnetic micro-roller using ultrasound phase analysis”. In: *Scientific Reports* 11.1 (2021), pages 1–10.
- [60] Salvador Pané et al. “Imaging technologies for biomedical micro-and nanoswimmers”. In: *Advanced Materials Technologies* 4.4 (2019), page 1800575.
- [61] Azaam Aziz et al. “Medical imaging of microrobots: Toward *in vivo* applications”. In: *ACS Nano* 14.9 (2020), pages 10865–10893.
- [62] Qianqian Wang et al. “Real-time magnetic navigation of a rotating colloidal microswarm under ultrasound guidance”. In: *IEEE Transactions on Biomedical Engineering* 67.12 (2020), pages 3403–3412.
- [63] Zhiguang Wu et al. “A microrobotic system guided by photoacoustic computed tomography for targeted navigation in intestines *in vivo*”. In: *Science Robotics* 4.32 (2019), eaax0613.
- [64] Paul Wrede et al. “Real-time 3D optoacoustic tracking of cell-sized magnetic microrobots circulating in the mouse brain vasculature”. In: *Science Advances* 8.19 (2022), eabm9132.
- [65] Azaam Aziz et al. “Dual ultrasound and photoacoustic tracking of magnetically driven micromotors: From *in vitro* to *in vivo*”. In: *Advanced Healthcare Materials* 10.22 (2021), page 2101077.
- [66] Elizabeth E Niedert et al. “A tumbling magnetic microrobot system for biomedical applications”. In: *Micromachines* 11.9 (2020), page 861.
- [67] Dongfang Li et al. “Automated *in vivo* navigation of magnetic-driven microrobots using OCT imaging feedback”. In: *IEEE Transactions on Biomedical Engineering* 67.8 (2019), pages 2349–2358.
- [68] Ben Wang et al. “Endoscopy-assisted magnetic navigation of biohybrid soft microrobots with rapid endoluminal delivery and imaging”. In: *Science Robotics* 6.52 (2021), eabd2813.

- [69] Xiaohui Yan et al. “Multifunctional biohybrid magnetite microrobots for imaging-guided therapy”. In: *Science Robotics* 2.12 (2017), eaaq1155.
- [70] Ania Servant et al. “Controlled *in vivo* swimming of a swarm of bacteria-like microrobotic flagella”. In: *Advanced Materials* 27.19 (2015), pages 2981–2988.
- [71] Sungwoong Jeon et al. “Magnetically actuated microrobots as a platform for stem cell transplantation”. In: *Science Robotics* 4.30 (2019), eaav4317.
- [72] Edward B Steager et al. “Automated biomanipulation of single cells using magnetic microrobots”. In: *The Int. Journal of Robotics Research* 32.3 (2013), pages 346–359.
- [73] Michael P Kummer et al. “OctoMag: An electromagnetic system for 5-DOF wireless micromanipulation”. In: *IEEE Transactions on Robotics* 26.6 (2010), pages 1006–1017.
- [74] Sumit Mohanty et al. “Bidirectional propulsion of arc-shaped microswimmers driven by precessing magnetic fields”. In: *Advanced Intelligent Systems* 2.9 (2020), page 2000064.
- [75] Ugur Bozuyuk et al. “Shape anisotropy-governed locomotion of surface microrollers on vessel-like microtopographies against physiological flows”. In: *Proceedings of the National Academy of Sciences* 118.13 (2021), e2022090118.
- [76] Lidong Yang et al. “Automated control of magnetic spore-based microrobot using fluorescence imaging for targeted delivery with cellular resolution”. In: *IEEE Transactions on Automation Science and Engineering* 17.1 (2019), pages 490–501.
- [77] Yunus Alapan et al. “Soft erythrocyte-based bacterial microswimmers for cargo delivery”. In: *Science Robotics* 3.17 (2018), eaar4423.
- [78] Timo Zimmermann et al. “Spectral imaging and its applications in live cell microscopy”. In: *FEBS Letters* 546.1 (2003), pages 87–92.
- [79] Lamiae Abdeladim et al. “Multicolor multiscale brain imaging with chromatic multiphoton serial microscopy”. In: *Nature Communications* 10.1 (2019), pages 1–14.
- [80] Jakob Nikolas Kather et al. “Color-coded visualization of magnetic resonance imaging multiparametric maps”. In: *Scientific Reports* 7.1 (2017), pages 1–11.
- [81] Chiara Stringari et al. “Multicolor two-photon imaging of endogenous fluorophores in living tissues by wavelength mixing”. In: *Scientific Reports* 7.1 (2017), pages 1–11.
- [82] Honglin Li and Joshua C Vaughan. “Switchable fluorophores for single-molecule localization microscopy”. In: *Chemical Reviews* 118.18 (2018), pages 9412–9454.
- [83] Yingxiao Wang et al. “Fluorescence proteins, live-cell imaging, and mechanobiology: seeing is believing”. In: *Annual Review of Biomedical Engineering Journal* 10 (2008), pages 1–38.
- [84] Jingwen Shou et al. “Super-multiplex imaging of cellular dynamics and heterogeneity by integrated stimulated Raman and fluorescence microscopy”. In: *Isience* 24.8 (2021), page 102832.
- [85] Amy M Bittel et al. “Varied length stokes shift BODIPY-based fluorophores for multicolor microscopy”. In: *Scientific Reports* 8.1 (2018), pages 1–12.
- [86] Andrew M Smith et al. “Multicolor quantum dots for molecular diagnostics of cancer”. In: *Expert Review of Molecular Diagnostics* 6.2 (2006), pages 231–244.
- [87] Jaroslav Icha et al. “Phototoxicity in live fluorescence microscopy, and how to avoid it”. In: *BioEssays* 39.8 (2017), page 1700003.
- [88] Kwan Seob Park et al. “Simultaneous multicolor imaging of wide-field epi-fluorescence microscopy with four-bucket detection”. In: *Bio. Opt. Express* 7.6 (2016), pages 2285–2294.

- [89] Ahmet Yildiz and Ronald D Vale. “Total internal reflection fluorescence microscopy”. In: *Cold Spring Harbor Protocols* 2015.9 (2015), pdb-top086348.
- [90] Olaf Schulz et al. “Resolution doubling in fluorescence microscopy with confocal spinning-disk image scanning microscopy”. In: *Proceedings of the National Academy of Sciences* 110.52 (2013), pages 21000–21005.
- [91] Rory M Power and Jan Huisken. “A guide to light-sheet fluorescence microscopy for multiscale imaging”. In: *Nature Methods* 14.4 (2017), pages 360–373.
- [92] Pierre Mahou et al. “Multicolor two-photon tissue imaging by wavelength mixing”. In: *Nature Methods* 9.8 (2012), pages 815–818.
- [93] Asylkhan Rakhymzhan et al. “Synergistic strategy for multicolor two-photon microscopy: application to the analysis of germinal center reactions *in vivo*”. In: *Scientific Reports* 7.1 (2017), pages 1–16.
- [94] David Entenberg et al. “Setup and use of a two-laser multiphoton microscope for multi-channel intravital fluorescence imaging”. In: *Nat. Proto.* 6.10 (2011), pages 1500–1520.
- [95] Arnab Halder and Yi Sun. “Biocompatible propulsion for biomedical micro/nano robotics”. In: *Biosensors and Bioelectronics* 139 (2019), page 111334.
- [96] Manuel Vonthron et al. “A MRI-based integrated platform for the navigation of micro-devices and microrobots”. In: *2011 IEEE/RSJ International Conference on Intelligent Robots and Systems (IROS)* (2011), pages 1285–1290.
- [97] Qianqian Wang and Li Zhang. “Ultrasound imaging and tracking of micro/nanorobots: From individual to collectives”. In: *IEEE Open Journal of Nanotechnology* 1 (2020), pages 6–17.
- [98] Lidong Yang et al. “Automated control of multifunctional magnetic spores using fluorescence imaging for microrobotic cargo delivery”. In: *2018 IEEE/RSJ International Conference on Intelligent Robots and Systems (IROS)* (2018), pages 1–6.
- [99] Longchen Wang et al. “Engineering magnetic micro/nanorobots for versatile biomedical applications”. In: *Advanced Intelligent Systems* 3.7 (2021), page 2000267.
- [100] Christoff Heunis et al. “Flexible instruments for endovascular interventions: Improved magnetic steering, actuation, and image-guided surgical instruments”. In: *IEEE Robotics & Automation Magazine* 25.3 (2018), pages 71–82.
- [101] Julien Leclerc et al. “A magnetic manipulator cooled with liquid nitrogen”. In: *IEEE Robotics & Automation Letters* 3.4 (2018), pages 4367–4374.
- [102] Jakub Sikorski et al. “Milimac: Flexible catheter with miniaturized electromagnets as a small-footprint system for microrobotic tasks”. In: *IEEE Robotics & Automation Letters* 5.4 (2020), pages 5260–5267.
- [103] Tiantian Xu et al. “Multimodal locomotion control of needle-like microrobots assembled by ferromagnetic nanoparticles”. In: *IEEE/ASME Transactions on Mechatronics* (2022), pages 1–12.
- [104] Jakub Sikorski et al. “Vision-based 3-D control of magnetically actuated catheter using BigMag—An array of mobile electromagnetic coils”. In: *IEEE/ASME Transactions on Mechatronics* 24.2 (2019), pages 505–516.
- [105] Stefano Scheggi et al. “A GPU-accelerated model-based tracker for untethered submillimeter grippers”. In: *Robotics and Autonomous Systems* 103 (2018), pages 111–121.

- [106] Federico Ongaro et al. “Autonomous planning and control of soft untethered grippers in unstructured environments”. In: *Journal of Micro-Bio Robotics* 12.1 (2017), pages 45–52.
- [107] Alper Denasi and Sarthak Misra. “Independent and leader–follower control for two magnetic micro-agents”. In: *IEEE Robotics & Automation Letters* 3.1 (2017), pages 218–225.
- [108] Neda Sharifi et al. “A feasibility study of *in vivo* control and tracking of microrobot using taxicab geometry for direct drug targeting”. In: *IEEE Transactions on NanoBioscience* 20.2 (2021), pages 235–245.
- [109] Jessica M Rosenholm et al. “Towards multifunctional, targeted drug delivery systems using mesoporous silica nanoparticles—opportunities & challenges”. In: *Nanoscale* 2.10 (2010), pages 1870–1883.
- [110] Jungho Ahn et al. “Microfluidics in nanoparticle drug delivery; From synthesis to pre-clinical screening”. In: *Advanced Drug Delivery Reviews* 128 (2018), pages 29–53.
- [111] Jigang Wu et al. “Optical imaging techniques in microfluidics and their applications”. In: *Lab on a Chip* 12.19 (2012), pages 3566–3575.
- [112] Sarvesh Kumar Srivastava et al. “Medibots: dual-action biogenic microdagger for single-cell surgery and drug release”. In: *Advanced Materials* 28.5 (2016), pages 832–837.
- [113] Xiaohui Yan et al. “Molecular cargo delivery using multicellular magnetic microswimmers”. In: *Applied Materials Today* 15 (2019), pages 242–251.
- [114] Carlos Aguilar-Avelar et al. “High-throughput automated microscopy of circulating tumor cells”. In: *Scientific Reports* 9.1 (2019), pages 1–9.
- [115] Lyubov V Doronina-Amitonova et al. “Multicolor *in vivo* brain imaging with a microscope-coupled fiber-bundle microprobe”. In: *Applied Physics Letters* 101.23 (2012), page 233702.
- [116] Samuel B Tristan-Landin et al. “Facile assembly of an affordable miniature multicolor fluorescence microscope made of 3D-printed parts enables detection of single cells”. In: *PLoS One* 14.10 (2019), e0215114.
- [117] Stephen ED Webb et al. “Multicolour single molecule imaging on cells using a supercontinuum source”. In: *Biomedical Optics Express* 3.3 (2012), pages 400–406.
- [118] Ke Wang et al. “Three-color femtosecond source for simultaneous excitation of three fluorescent proteins in two-photon fluorescence microscopy”. In: *Biomedical Optics Express* 3.9 (2012), pages 1972–1977.
- [119] Jacob Licea-Rodriguez et al. “Multicolor fluorescence microscopy using static light sheets and a single-channel detection”. In: *Journal of Biomedical Optics* 24.1 (2019), page 016501.
- [120] Xing Zhou et al. “Image recombination transform algorithm for superresolution structured illumination microscopy”. In: *Journal of Biomedical Optics* 21.9 (2016), page 096009.
- [121] Qingling Li et al. “Multicolor fluorescence detection-based microfluidic device for single-cell metabolomics: simultaneous quantitation of multiple small molecules in primary liver cells”. In: *Analytical Chemistry* 88.17 (2016), pages 8610–8616.
- [122] Yulung Sung et al. “Open-source do-it-yourself multi-color fluorescence smartphone microscopy”. In: *Biomedical Optics Express* 8.11 (2017), pages 5075–5086.
- [123] Chang-Deng Hu and Tom K Kerppola. “Simultaneous visualization of multiple protein interactions in living cells using multicolor fluorescence complementation analysis”. In: *Nature Biotechnology* 21.5 (2003), pages 539–545.
- [124] Daniel R Larson et al. “Water-soluble quantum dots for multiphoton fluorescence imaging *in vivo*”. In: *Science* 300.5624 (2003), pages 1434–1436.

- [125] Roman A Verkhovskii et al. “Lightsheet-based flow cytometer for whole blood with the ability for the magnetic retrieval of objects from the blood flow”. In: *Biomedical Optics Express* 12.1 (2021), pages 380–394.
- [126] Pierre Pouponneau et al. “Therapeutic magnetic microcarriers guided by magnetic resonance navigation for enhanced liver chemoembolization: a design review”. In: *Annals of Biomedical Engineering* 42.5 (2014), pages 929–939.
- [127] Haifeng Xu et al. “Sperm-hybrid micromotor for targeted drug delivery”. In: *ACS Nano* 12.1 (2018), pages 327–337.
- [128] Chenying Yang et al. “Mitigating fluorescence spectral overlap in wide-field endoscopic imaging”. In: *Jour. of Biomedical Optics* 18.8 (2013), page 086012.
- [129] Bongsu Jung et al. “Revisiting indocyanine green: effects of serum and physiological temperature on absorption and fluorescence characteristics”. In: *IEEE Journal of Selected Topics in Quantum Electronics* 20.2 (2013), pages 149–157.
- [130] Oguzhan Avci et al. “Pupil function engineering for enhanced nanoparticle visibility in wide-field interferometric microscopy”. In: *Optica* 4.2 (2017), pages 247–254.
- [131] Sara Abrahamsson et al. “Fast multicolor 3D imaging using aberration-corrected multifocus microscopy”. In: *Nature Methods* 10.1 (2013), pages 60–63.
- [132] Younan Xia and George M Whitesides. “Soft lithography”. In: *Angewandte Chemie International Edition* 37.5 (1998), pages 550–575.
- [133] Sungjo Park et al. “*In vivo* photoacoustic and fluorescence cystography using clinically relevant dual modal indocyanine green”. In: *Sensors* 14.10 (2014), pages 19660–19668.
- [134] Mark Bates et al. “Multicolor super-resolution fluorescence imaging via multi-parameter fluorophore detection”. In: *ChemPhysChem* 13.1 (2012), pages 99–107.
- [135] Zhou Wang et al. “Image quality assessment: from error visibility to structural similarity”. In: *IEEE Transactions on Image Processing* 13.4 (2004), pages 600–612.
- [136] Onur Mudanyali et al. “Wide-field optical detection of nanoparticles using on-chip microscopy and self-assembled nanolenses”. In: *Nat. Photonics* 7.3 (2013), pages 247–254.
- [137] Fatih Aydoğan et al. “Sentinel lymph node biopsy under fluorescent indocyanine green guidance: Initial experience”. In: *Turkish Journal of Surgery/Ulusal Cerrahi Dergisi* 32.1 (2016), page 50.
- [138] Mustafa Kemal Ruhi et al. “Dose-dependent photochemical/photothermal toxicity of indocyanine green-based therapy on three different cancer cell lines”. In: *Photodiagnosis and Photodynamic Therapy* 21 (2018), pages 334–343.
- [139] Eric AJ Reits and Jacques J Neefjes. “From fixed to FRAP: measuring protein mobility and activity in living cells”. In: *Nat. Cell Biology* 3.6 (2001), E145.
- [140] T Bernas et al. “Minimizing photobleaching during confocal microscopy of fluorescent probes bound to chromatin: role of anoxia and photon flux”. In: *Journal of Microscopy* 215.3 (2004), pages 281–296.
- [141] Bruce D Lucas and Takeo Kanade. “An iterative image registration technique with an application to stereo vision”. In: *In Proceedings of the International Joint Conference on Artificial Intelligence* (1981), pages 674–679.
- [142] Eric Diller and Metin Sitti. “Three-dimensional programmable assembly by untethered magnetic robotic micro-grippers”. In: *Adv. Funct. Mat.* 24.28 (2014), pages 4397–4404.

- [143] N Ma and G Song. “Control of shape memory alloy actuator using pulse width modulation”. In: *Smart Materials and Structures* 12.5 (2003), page 712.
- [144] J. J. Abbott and B. Osting. “Optimization of coreless electromagnets to maximize field generation for magnetic manipulation systems”. In: *IEEE Magnetics Letters* 9 (2018), pages 1–4.
- [145] Eric Diller et al. “Independent control of multiple magnetic microrobots in three dimensions”. In: *The International Journal of Robotics Research* 32.5 (2013), pages 614–631.
- [146] S. L. Charreyron et al. “Shared control of a magnetic microcatheter for vitreoretinal targeted drug delivery”. In: *IEEE International Conference on Robotics and Automation (ICRA)* (2017), pages 4843–4848.
- [147] K. J. Boskma et al. “Closed-loop control of a magnetically-actuated catheter using two-dimensional ultrasound images”. In: *IEEE International Conference on Biomedical Robotics and Biomechatronics (BioRob)* (2016), pages 61–66.
- [148] B. E. Kratochvil et al. “Visual servoing and characterization of resonant magnetic actuators for decoupled locomotion of multiple untethered mobile microrobots”. In: *IEEE International Conference on Robotics and Automation (ICRA)* (2009), pages 1010–1015.
- [149] K. Shirabe et al. “Advantages of high frequency PWM in AC motor drive applications”. In: *IEEE Energy Conversion Congress and Exposition (ECCE)* (2012), pages 2977–2984.
- [150] Hengchun Mao et al. “Analysis and design of high frequency three-phase boost rectifiers”. In: *IEEE Applied Power Electronics Conference and Exposition (APEC)* (1996), pages 538–544.
- [151] Alexandre Cunha Oliveira et al. “Improved dead-time compensation for sinusoidal PWM inverters operating at high switching frequencies”. In: *IEEE Transactions on Industrial Electronics* 54.4 (2007), pages 2295–2304.
- [152] B. J. Patella et al. “High-frequency digital PWM controller IC for DC-DC converters”. In: *IEEE Transactions on Power Electronics* 18.1 (2003), pages 438–446.
- [153] Di Han et al. “Comparison between output CM chokes for SiC drive operating at 20- and 200-kHz switching frequencies”. In: *IEEE Transactions on Industry Applications* 53.3 (2017), pages 2178–2188.
- [154] Challa SSR Kumar and Faruq Mohammad. “Magnetic nanomaterials for hyperthermia-based therapy and controlled drug delivery”. In: *Advanced Drug Delivery Reviews* 63.9 (2011), pages 789–808.
- [156] Arthur Farnsworth et al. “Cooling system for a computer environment”. In: (2006). US Patent App. 11/056,300.
- [157] Bok Lae Cho and In Yong Park. “Electron microscope electron gun for facilitating position adjustment and electron microscope including same”. In: (2018). US Patent App. 15/576,687.
- [158] Brendan Whelan et al. “Passive magnetic shielding in MRI-Linac systems”. In: *Physics in Medicine & Biology* 63.7 (2018), page 075008.
- [160] Gaoui Bachir et al. “Comparison electromagnetic shielding effectiveness between single layer and multilayer shields”. In: *IEEE Power Engineering Conference (UPEC)* (2016), pages 1–5.
- [161] Muhammed Nasir Inan and Mehmet Arik. “A multi-functional design approach and proposed figure of merits for solid state lighting systems”. In: *Journal of Solid State Lighting* 1.1 (2014), pages 1–8.

- [162] Umut Zeynep Uras et al. “Thermal performance of a light emitting diode light engine for a multipurpose automotive exterior lighting system with competing board technologies”. In: *Journal of Electronic Packaging* 139.2 (2017), page 020907.
- [163] Simone Schuerle et al. “Three-dimensional magnetic manipulation of micro-and nanostructures for applications in life sciences”. In: *IEEE Transactions on Magnetics* 49.1 (2013), pages 321–330.
- [164] Alexander Tokarev et al. “Multifunctional magnetic rotator for micro and nanorheological studies”. In: *Review of Scientific Instruments* 83.6 (2012), page 065110.
- [165] Stefano Scheggi et al. “Magnetic motion control and planning of untethered soft grippers using ultrasound image feedback”. In: *2017 IEEE International Conference on Robotics and Automation (ICRA)* (2017), pages 6156–6161.
- [166] Jasper D Keuning et al. “Image-based magnetic control of paramagnetic microparticles in water”. In: *2011 IEEE/RSJ International Conference on Intelligent Robots and Systems (IROS)* (2011), pages 421–426.
- [167] Ayoung Hong et al. “Real-time holographic tracking and control of microrobots”. In: *IEEE Robotics & Automation Letters* 2.1 (2016), pages 143–148.
- [169] Yafei Wang et al. “Multirate estimation and control of body slip angle for electric vehicles based on onboard vision system”. In: *IEEE Transactions on Industrial Electronics* 61.2 (2013), pages 1133–1143.
- [170] Minghui Zheng et al. “Multi-rate observer based sliding mode control with frequency shaping for vibration suppression beyond nyquist frequency”. In: *IFAC-PapersOnLine* 49.21 (2016), pages 13–18.
- [171] Mahadevamurty Nemani et al. “Multi-rate analysis and design of visual feedback digital servo-control system”. In: *Journal of Dynamic Systems, Measurement, and Control* 116.1 (1994), pages 45–55.
- [172] Jean-Yves Bouguet. “Pyramidal implementation of the affine lucas kanade feature tracker description of the algorithm”. In: *Intel Corp.* 5.1-10 (2001), page 4.
- [173] Simon Baker and Iain Matthews. “Lucas-kanade 20 years on: A unifying framework”. In: *International Journal of Computer Vision* 56.3 (2004), pages 221–255.
- [174] Selim Benhimane and Ezio Malis. “Real-time image-based tracking of planes using efficient second-order minimization”. In: *2004 IEEE/RSJ International Conference on Intelligent Robots and Systems (IROS)* (2004), pages 943–948.
- [175] Rogerio Richa et al. “Robust similarity measures for gradient-based direct visual tracking”. In: *The Johns Hopkins University, Tech. Rep* (2012).
- [176] Myung Hwangbo et al. “Inertial-aided KLT feature tracking for a moving camera”. In: *2009 IEEE/RSJ International Conference on Intelligent Robots and Systems (IROS)* (2009), pages 1909–1916.
- [177] Iain Matthews et al. “The template update problem”. In: *IEEE Transactions on Pattern Analysis and Machine Intelligence* 26.6 (2004), pages 810–815.
- [179] Hebertt Sira-Ramírez and Vicente Feliu Batlle. “Robust Σ - Δ modulation-based sliding mode observers for linear systems subject to time polynomial inputs”. In: *International Journal of Systems Science* 42.4 (2011), pages 621–631.
- [180] Reinhard Gahleitner and Martin Schagerl. “A state observer for using a slow camera as a sensor for fast control applications”. In: *Image Processing: Machine Vision Applications VI* 8661 (2013), pages 15–24.

- [181] Zhong-Ping Jiang and Yuan Wang. “Input-to-state stability for discrete-time nonlinear systems”. In: *Automatica* 37.6 (2001), pages 857–869.
- [182] Lin Yang et al. “Prediction based collaborative trackers (PCT): A robust and accurate approach toward 3D medical object tracking”. In: *IEEE Transactions on Medical Imaging* 30.11 (2011), pages 1921–1932.
- [183] Zdenek Kalal et al. “Forward-backward error: Automatic detection of tracking failures”. In: *2010 20th International Conference on Pattern Recognition* (2010), pages 2756–2759.
- [184] Yunus Alapan et al. “Microrobotics and microorganisms: Biohybrid autonomous cellular robots”. In: *Annual Review of Control, Robotics, and Autonomous Systems* 2 (2019), pages 205–230.
- [185] Deasung Jang et al. “Targeted drug delivery technology using untethered microrobots: A review”. In: *Journal of Micromechanics and Microengineering* 29.5 (2019), page 053002.
- [186] Hakan Ceylan et al. “Mobile microrobots for bioengineering applications”. In: *Lab on a Chip* 17.10 (2017), pages 1705–1724.
- [187] Mariana Medina-Sánchez and Oliver G Schmidt. “Medical microrobots need better imaging and control”. In: *Nature* 545.7655 (2017), pages 406–408.
- [188] Pierre Pouponneau et al. “Magnetic nanoparticles encapsulated into biodegradable microparticles steered with an upgraded magnetic resonance imaging system for tumor chemoembolization”. In: *Biomaterials* 30.31 (2009), pages 6327–6332.
- [189] Onder Erin et al. “Magnetic resonance imaging system-driven medical robotics”. In: *Advanced Intelligent Systems* 2.2 (2020), page 1900110.
- [190] Phu Bao Nguyen et al. “Real-time microrobot posture recognition via biplane X-ray imaging system for external electromagnetic actuation”. In: *International Journal of Computer Assisted Radiology and Surgery* 13.11 (2018), pages 1843–1852.
- [191] Kim Tien Nguyen et al. “Guide-wired helical microrobot for percutaneous revascularization in chronic total occlusion in-vivo validation”. In: *IEEE Transactions on Biomedical Engineering* 68.8 (2020), pages 2490–2498.
- [192] Qianqian Wang et al. “Ultrasound Doppler-guided real-time navigation of a magnetic microswarm for active endovascular delivery”. In: *Science Advances* 7.9 (2021), eabe5914.
- [193] Islam SM Khalil et al. “Magnetic-based closed-loop control of paramagnetic microparticles using ultrasound feedback”. In: *2014 IEEE International Conference on Robotics and Automation (ICRA)* (2014), pages 3807–3812.
- [194] Stefano Pane et al. “Ultrasound acoustic phase analysis enables robotic visual-servoing of magnetic microrobots”. In: *IEEE Transactions on Robotics* 38.3 (2022), pages 1571–1582.
- [195] Sumit Mohanty et al. “CeFlowBot: A biomimetic flow-driven microrobot that navigates under magneto-acoustic fields”. In: *Small* (2021), page 2105829.
- [196] Yan Yan et al. “Photoacoustic imaging to track magnetic-manipulated micro-robots in deep tissue”. In: *Sensors* 20.10 (2020), page 2816.
- [197] Ugur Bozuyuk et al. “High-performance magnetic FePt (L10) surface microrollers towards medical imaging-guided endovascular delivery applications”. In: *Advanced Functional Materials* 32.8 (2022), page 2109741.
- [198] Mert Kaya et al. “Serial imaging of micro-agents and cancer cell spheroids in a microfluidic channel using multicolor fluorescence microscopy”. In: *PLoS One* 16.6 (2021), e0253222.

- [199] Azaam Aziz et al. “Real-time IR tracking of single reflective micromotors through scattering tissues”. In: *Advanced Functional Materials* 29.51 (2019), page 1905272.
- [200] Clément Ricard et al. “Six-color intravital two-photon imaging of brain tumors and their dynamic microenvironment”. In: *Frontiers in Cellular Neuroscience* 8 (2014), page 57.
- [201] Philip R Nicovich et al. “NicoLase—an open-source diode laser combiner, fiber launch, and sequencing controller for fluorescence microscopy”. In: *PLoS One* 12.3 (2017), e0173879.
- [202] Islam SM Khalil et al. “Sperm-shaped magnetic microrobots: Fabrication using electrospinning, modeling, and characterization”. In: *2016 IEEE International Conference on Robotics and Automation (ICRA)* (2016), pages 1939–1944.
- [203] Chaobo Huang et al. “Unbreakable codes in electrospun fibers: digitally encoded polymers to stop medicine counterfeiting”. In: *Advanced Materials* 22.24 (2010), pages 2657–2662.
- [204] J Anu Bhushani and Chinnaswamy Anandharamakrishnan. “Electrospinning and electro-spraying techniques: Potential food based applications”. In: *Trends in Food Science & Technology* 38.1 (2014), pages 21–33.
- [205] Prasanna Padmanaban et al. “Assessment of flow within developing chicken vasculature and biofabricated vascularized tissues using multimodal imaging techniques”. In: *Scientific Reports* 11.1 (2021), pages 1–14.
- [206] Mert Kaya et al. “Development of a coil driver for magnetic manipulation systems”. In: *IEEE Magnetics Letters* 10 (2019), pages 1–5.
- [207] Mert Kaya et al. “A multi-rate state observer for visual tracking of magnetic micro-agents using 2D slow medical imaging modalities”. In: *2018 IEEE/RSJ International Conference on Intelligent Robots and Systems (IROS)* (2018), pages 1–8.
- [208] Telma Cristina Esteves et al. “A microfluidic system supports single mouse embryo culture leading to full-term development”. In: *RSC Advances* 3.48 (2013), pages 26451–26458.
- [209] Wanyoung Lim and Sungsu Park. “A microfluidic spheroid culture device with a concentration gradient generator for high-throughput screening of drug efficacy”. In: *Molecules* 23.12 (2018), page 3355.
- [210] Xiuli Hu et al. “Electrospinning of polymeric nanofibers for drug delivery applications”. In: *Journal of Controlled Release* 185 (2014), pages 12–21.
- [211] Joana Angélica Loureiro and Maria Carmo Pereira. “PLGA based drug carrier and pharmaceutical applications: the most recent advances”. In: *Pharmaceutics* 12.9 (2020), page 903.
- [212] Ming-Yi Hsu et al. “Enhanced paclitaxel efficacy to suppress triple-negative breast cancer progression using metronomic chemotherapy with a controlled release system of Electrospun Poly-DL-Lactide-co-glycolide (PLGA) nanofibers”. In: *Cancers* 13.13 (2021), page 3350.
- [213] Rafael Contreras-Cáceres et al. “Electrospun nanofibers: Recent applications in drug delivery and cancer therapy”. In: *Nanomaterials* 9.4 (2019), page 656.
- [214] Ali Tanhaei et al. “Electrospraying as a novel method of particle engineering for drug delivery vehicles”. In: *Journal of Controlled Release* 330 (2021), pages 851–865.
- [215] Ji Liu et al. “Design of hybrid nanovehicles for remotely triggered drug release: an overview”. In: *Journal of Materials Chemistry B* 3.30 (2015), pages 6117–6147.
- [216] Chizhu Ding and Zibiao Li. “A review of drug release mechanisms from nanocarrier systems”. In: *Materials Science and Engineering: C* 76 (2017), pages 1440–1453.

- [217] Juliana M Chan et al. “PLGA–lecithin–PEG core–shell nanoparticles for controlled drug delivery”. In: *Biomaterials* 30.8 (2009), pages 1627–1634.
- [218] Guillermo J Tearney et al. “*In vivo* endoscopic optical biopsy with optical coherence tomography”. In: *Science* 276.5321 (1997), pages 2037–2039.
- [219] Dirk Lorensen et al. “Dual-modality needle probe for combined fluorescence imaging and three-dimensional optical coherence tomography”. In: *Optics Letters* 38.3 (2013), pages 266–268.
- [220] Daniel Aharoni et al. “All the light that we can see: a new era in miniaturized microscopy”. In: *Nature Methods* 16.1 (2019), pages 11–13.

Books

- [155] James K Roberge. *Operational amplifiers: theory and practice*. Volume 197. Wiley New York, 1975. Chapter 11.
- [159] V. V. Yashchuk et al. *Magnetic shielding*. Edited by Dmitry Budker and Derek F. Editors Jackson Kimball. Cambridge University Press, 2013, pages 225–248.
- [168] Shahram Vaezy and Vesna Zderic. *Image-Guided Therapy Systems*. Artech House, 2009. Chapter 2.
- [178] Raymond A. DeCarlo. *Some Techniques for Computing The Matrix Exponential and its Integral*. Prentice-Hall, 1989. Chapter 14.

Acknowledgments

This doctoral thesis would not have been possible without the help of many people for whom I am sincerely grateful. First and foremost, I would like to thank my advisor, Prof. Sarthak Misra, for accepting me as his Ph.D. student. Thank you for giving me the opportunity to work on project-ROBOTAR. Dear Prof. Misra (sevgili ve değerli hocam), the Mert is grateful for your constant support, valuable comments, and directions for preparing this thesis. The Mert aspires to become a perfect scientific writer like you and appreciates that you patiently helped him for improving his writing skills. I wish to thank my co-advisor, Dr. Islam S.M. Khalil, for his guidance, vision, and valuable suggestions during the second half of my Ph.D. research. Dear Dr. Khalil, special thanks for introducing me to the electrospinning technique. I want to accentuate that electrospinning opened a new era in my research. I also express my deepest gratitude to the European Research Council for funding and the University of Twente for providing a research environment.

My appreciation goes to Lianne Bode, Jeanine Lodeweges-de Vries, and Yolanda Assink-Strokappe. As Sumit Mohanty stated in his Ph.D. thesis, I can't imagine a day without your presence at the University of Twente. I believe that your ready-to-help attitude makes everyone's life easier. Mrs. Lianne, I don't know what to say. Our conversations broadened my horizon and motivated me during difficult times in my Ph.D. journey. Thank you so much for everything! Mrs. Jeanine, it is impossible to forget your guidance and valuable support. Thank you for always welcoming me with your positive energy and helping me solve complex issues. My heartfelt gratitude goes to Lorena Montoya, who always helped me without hesitation, as did Mrs. Lianne, Mrs. Jeanine, and Yolanda. Thank you for your guidance, patience, and efforts that helped me get to the finish line.

I want to extend my deepest gratitude and appreciation to Mert Karaca, Dr. Özkan Bebek, Dr. Devrim Ünay, Dr. Ergün Şimşek, Dr. Babür Baki Hadimioğlu, Prof. Fatih Uğurdağ, Prof. Yıldırım Üçtuğ, and Prof. Hayrettin Kara. I would not be where I am today without your insightful guidance. I will forever be grateful for guiding me toward the right path in the scientific world. Özkan Hocam, thank you for accepting me as your master's student and introducing me to the field of medical robotics. The engineering

skills I learned from you have guided me and created a baseline for my doctoral study. I sincerely thank you for opening my eyes to multidisciplinary research areas. You and Fatih Hocam are one of the people I care about and value very much. Fatih Hocam, I do not know how I could ever express my thanks for your mentorship. I feel that your presence in my life has blessed me since 2006. I hope that I will be your 911 until the end of my life, and we will never disconnect from each other. Thank you for everything! Hayrettin Hocam, I do not doubt that you are a great physician, visionary academy member, and pure human. Frankly, you are one of my role models. I frequently bug you to learn tricky points regarding becoming a mastermind and knowledge seeker. Thank you for helping me in difficult times and sharing your motivational quotes with me. "İyi bir hoca ilk önce hocasını geçer daha sonra kendinden daha iyi bir öğrenci yetiştirir!" is a game-changer quote in my life and became my main philosophy. With your permission, I share this quote taken from Nietzsche with my prospective students, friends, colleagues, and advisors.

A special thank goes to my precious friend, Fabian Stein. It was my honor and privilege to make collaboration with you. Our scientific discussions always helped me to shape this dissertation. Your knowledge and expertise in biology are admirable. I also wish to thank Vasileios Trikalitis, Prasanna Padmanaban, and Erdem Ağbahca for our fruitful discussions and collaborative work. Vasileios, thanks for introducing me to inspiring topics from material science and 3D bioprinting. Erdem, thank you for being my friend and always supporting me with your wisdom. My sincere thanks go to Wouter Abbas, Quint Meinders, Nancy C.M. Heijnekamp-Snellens, Herman Kuiper, Andries Klijnstra, Edwin Morsink, Martijn Wessels, Michiel Ligtenberg, Remco Sanders, Nick Helthuis, Erik G. de Vries, Robert Jan Meijer, and Jacqueline Plass for providing technical support. Your suggestions helped me a lot to improve the content of this dissertation.

I thank my dear colleagues Alper Denasi, Onno Derkman, Michiel Richter, Theodosia Lourdes Thomas, Foad Sojoodi Farimani, Robbert-Jan Fidler, Akin Sahin, Ayhan Alp Aydeniz, Sumit Mohanty, Venkat Kalpathy Venkiteswaran, Christoff Heunis, Chen Wang, Chuang Li, Juan Julian Jesus Huaroto Sevilla, Kaixuan Zhang, Yiyang Li, Yu-Hsiang Lin, Zhengya Zhang, Zhuoyue Wang, Zihan Wang, Mina M. M. Farag, Alaaeldine Sadek, Filip Šuligoj, Jakub Sikorski, Oskar van der Wal, Luigi Capuano, Stefano Scheggi, Ugo Siciliani De Cumis, Fouzia Khan, Guilherme Phillips Furtado, Klaas Jelmer Boskma, Chiel van Vliet, Jesús Jimenez Palao, Mohamed Ehab Hafez, Morteza Mojarradi, and Deepti Rana. We shared lots of good times in Surgical Robotics. I am grateful for your help, patience, and friendship, which enabled me to complete this doctoral dissertation. I especially thank Theodosia Lourdes Thomas and Michiel Richter for their valuable comments on my thesis. It is also my pleasure to see them as my paranymphs.

I would also like to thank Dr. Jeroen Rouwkema, Prof. Ivo Vellekoop, Prof. Inge Zuhorn, and Prof. Quan Zhou for accepting to participate on my thesis committee, their critical thinking, and their valuable comments.

Last but not least, I would like to thank my lovely family members, who have always deeply supported me. I have always considered myself very lucky to be a member of such a great family. I am grateful for your patience, sacrifice, and love. Thank you for being my family! I dedicate my doctoral thesis to the members of my family who are always there for me in difficult times.

Mert Kaya
Enschede, The Netherlands
University of Twente, 2022.

About the Author

Mert Kaya was born on 28th April 1989 in Istanbul, Turkey. He received the bachelor's degree in electrical and electronics engineering from Bahçeşehir University, Istanbul, Turkey, in 2011, and the master's degree in electrical and electronics engineering from Özyeğin University, Istanbul, in 2015. In April 2017, he joined the Surgical Robotics Laboratory (SRL) in Biomechanical Engineering at the University of Twente as a doctoral candidate under the supervision of Dr. Islam S.M. Khalil and Prof. Dr. Sarthak Misra. Here, he was baptized as the Mert by Prof. Misra and established the Surgical Robotics Laboratory - Laser and Imaging Lab (SRL-LIL). During his Ph.D. study, the Mert focused on the fabrication, actuation, and imaging of therapeutic microrobotic agents. He has also been a visiting researcher with the Biomedical Engineering Department, University Medical Centre at Groningen, the Netherlands. The doctoral dissertation you are reading contains the outcome of his research of five years, six months, twenty-six days, seven hours, and forty-five minutes.



A message from the Mert to the prospective doctoral students: The fact is that Ph.D. is a lifestyle, not a job. As Prof. Misra says, "Do it once and do it properly!" can be a good motto for your new lifestyle.

I am the Mert, and we are in the end.